

UNIVERSIDAD DE CHILE
FACULTAD DE CIENCIAS FISICAS Y MATEMATICAS
DEPARTAMENTO DE ASTRONOMIA

**CONFRONTANDO MODELOS HIDRODINAMICOS
CON OBSERVACIONES DE SUPERNOVAS DE
TIPO II-PLATEAU**

**TESIS PARA OPTAR AL GRADO DE DOCTOR EN CIENCIAS
MENCION ASTRONOMIA**

MELINA CECILIA BERSTEN

PROFESOR GUIA:

Mario Hamuy Wackenhut

MIEMBROS DE LA COMISION:

Omar Benvenuto

Alejandro Clocchiatti

Andrés Escala Astorquiza

José Maza Sancho

SANTIAGO DE CHILE

JULIO 2010

Nota: El Prof. Omar Benvenuto fue co-director de esta tesis. Por motivos administrativos, aparece como miembro de la comisión evaluadora.

Note: Prof. Omar Benvenuto was co-director of this thesis. For administrative reasons, he appears as a member of the evaluation committee.

Resumen

El objetivo principal de esta tesis es el desarrollo de un código hidrodinámico unidimensional para modelar curvas de luz bolométricas de supernovas de tipo II plateau (SNs II-P) con el propósito final de analizar las propiedades físicas de los progenitores de estas supernovas comparando nuestros modelos con una gran base de datos de muy buena calidad y cobertura temporal.

Para poder comparar nuestro modelo con las observaciones hemos derivado calibraciones para la corrección bolométrica (CB) y la temperatura efectiva basadas en fotometría *BVI*. La dispersión típica de la calibración encontrada para la CB conduce a una incerteza de 0.05 dex en la luminosidad.

Usando nuestro código hemos estudiado en detalle el caso de la SN 1999em, una de las SNs II-P mejor observadas, y encontramos un muy buen acuerdo con las observaciones usando los siguientes parámetros físicos: $E = 1.25$ foe, $M = 19 M_{\odot}$, $R = 800 R_{\odot}$, and $M_{\text{Ni}} = 0.056 M_{\odot}$. En este análisis vemos que es necesario usar una extensa mezcla de ^{56}Ni para reproducir un plateau tan chato como muestran las observaciones.

Hemos calculado curvas de luz bolométricas para todas las SNs de nuestra muestra y definido una serie de parámetros que nos permiten caracterizarlas. Comparando dichos parámetros encontramos un rango de 1, 15 dex en la luminosidad del plateau, un rango de duración del plateau de 64 a 103 días y masas de níquel inferiores a 0, 1 M_{\odot} para todas las SNs en nuestra muestra, con la excepción de SN 1992am.

Finamente, hemos calculado una grilla de modelos hidrodinámicos para estudiar la dependencia de diferentes observables con los parámetros físicos (masas, radio y energía de la explosión) y las correlaciones entre distintos observables. A partir de este análisis vemos que nuestros modelos reproducen la fuerte correlación observada entre

la luminosidad y la velocidad de expansión durante el plateau.

Agradecimientos

Quiero agradecer en primer lugar a Gastón Folatelli por su apoyo constante a lo largo de esta tesis no sólo desde el punto de vista emocional si no también científico. A mis directores, Omar Benvenuto por su incondicional apoyo y por toda la experiencia científica que me ha transmitido; y Mario Hamuy por haberme impulsado constantemente a la búsqueda de un poco más y también por las oportunidades que me ha brindado. A ambos les agradezco la confianza y la independencia con las que me han dejado trabajar.

Quiero agradecer profundamente a Ken'ichi Nomoto por haberme invitado al IPMU, experiencia que fue fundamental para terminar de madurar varios de los temas tratados en esta tesis. Un especial agradecimiento a Sergei Blinnikov por todas las conversaciones, sugerencias y por el interés puesto en mi trabajo; y también a Elena Sorokina. Con ambos compartí unos meses muy intensos con hermosas tardes de té, ciencia y otros temas. También me gustaría agradecer a Nozomu Tominaga por su ayuda para testear mi modelo. A Giuliano Pignata por ser el ideólogo de mi estadía en Japón y a Alejandro Clocchiatti por su apoyo y el permanente entusiasmo puesto en mi trabajo.

No quisiera dejar de agradecer a mi familia, en especial a mi abuela y a mi hermana Lara. A mis amigos de La Serena, Julia, Nidia y Rodolfo, de Santiago en especial a Cristian y Maria José y por supuesto también a mis amigos de mi querida y extrañada La Plata, a Andrea F., Andrea T., Cecilia, Mariana, Martin, Verónica, Ricardo y a Ramiro por sus hermosas visitas. Gracias amigos por aguantar mis descargas y transmitirme siempre alegría y confianza.

List of Figures

1.1	SNe classification	3
1.2	LC of SN II-P	6
1.3	Spectra of SN II-P	7
3.1	Rosseland mean opacity	27
3.2	Gamma-ray deposition	30
3.3	Density distribution for single polytropic model	31
3.4	Double-polytropic initial models for different masses	33
3.5	Double-polytropic initial models for different radii	33
3.6	LC for single and double polytropic model	34
3.7	Density distribution form stellar evolution	35
3.8	LC for stellar evolution progenitor	35
3.9	Code Scheme	36

3.10	Evolutionary phases of a LC	38
3.11	Comparison with STELLA Code	40
3.12	LC for different values of the opacity minimum	41
4.1	Blackbody fit to the monochromatic fluxes	45
4.2	Contributions to the bolometric flux	46
4.3	UV contribution to the total flux	47
4.4	Bolometric luminosity of SN 1987A, SN 1999em and SN 2003hn . . .	49
4.5	Bolometric corrections versus $(B - V)$ and $(V - I)$	51
4.6	Bolometric corrections versus $(B - I)$	52
4.7	Bolometric corrections for radioactive tail phase versus $(B - V)$. . .	56
4.8	Effective temperature versus $(B - V)$	58
4.9	Effective temperatures for SN 1987A, SN 1999em and SN 2003hn . .	60
5.1	Initial density distribution for model M19R8E1.25NI56	64
5.2	Abundance distribution for model M19R8E1.25NI56	65
5.3	The bolometric light curve for model M19R8E1.25NI56 compared with the data of SN 1999em	66
5.4	The photosphere velocity for model M19R8E1.25NI56 compared with data of SN 1999em	67

5.5	SW propagation on different physical quantities	69
5.6	Bolometric luminosity and effective temperature during breakout . .	70
5.7	Evolution of the velocity for different layers	73
5.8	Evolution of the fraction of ionized hydrogen, opacity and temperature	75
5.9	Bolometric LC without energy released by recombination	77
5.10	Evolution of the interior luminosity	78
5.11	Comparison between bolometric LCs for different ^{56}Ni mixing	79
5.12	Evolution of photospheric radius, velocity and mass above the photo- sphere	80
5.13	Low mass models for SN 1999em	86
5.14	Low mass models for SN 1999em (continuation)	87
5.15	Low mass models for SN 1999em (continuation)	89
5.16	Low mass models for SN 1999em (continuation)	90
6.1	Bolometric luminosities and effective temperatures for SNe II-P (part 1)	95
6.2	Bolometric luminosities and effective temperatures for SNe II-P (part 2)	96
6.3	Bolometric luminosities and effective temperatures for SNe II-P (part 3)	97
6.4	Bolometric luminosities and effective temperatures for SNe II-P (part 4)	98

6.5	Bolometric luminosities and effective temperatures for SNe II-P (part 5)	99
6.6	Bolometric luminosities and effective temperatures for SNe II-P (part 6)	100
6.7	Bolometric luminosities and effective temperatures for SNe II-P (part 7)	101
6.8	Bolometric luminosities and effective temperatures for SNe II-P (part 8)	102
6.9	Bolometric luminosities and effective temperatures for SNe II-P (part 9)	103
6.10	Bolometric luminosities and effective temperatures for SNe II-P (part 10)	104
6.11	Bolometric LC and observed parameters	105
6.12	The distribution of L_p for SNe II-P	107
6.13	Range of the plateau luminosities	108
6.14	Distribution of Δt_p for SNe II-P	110
6.15	Range of variation of the plateau lengths	111
6.16	Distribution of $\Delta \log L$ for SNe II-P	113
6.17	Different transition properties	114
6.18	Distribution of ^{56}Ni masses for SNe II-P	117
6.19	Tail luminosity	118
6.20	Bolometric LC for different physical parameters	120
6.21	Model dependence of L_P on explosion energy	122

6.22	Model dependence of Δt_P on explosion energy	123
6.23	Model dependence of ΔL on explosion energy	124
6.24	Model dependence of $\text{Log } v_{-30}$ on explosion energy	125
6.25	Plateau luminosity vs. ^{56}Ni mass	128
6.26	Plateau duration vs. ^{56}Ni mass	129
6.27	The drop in luminosity vs. ^{56}Ni mass	130
6.28	The photosperic velocity vs. ^{56}Ni mass	131
6.29	Plateau luminosity vs. photosperic velocity	133
6.30	Plateau luminosity vs. plateau duration	134
6.31	Plateau luminosity vs. the drop in luminosity	135
6.32	Plateau duration vs. photosperic velocity	136
A.1	Space-time grid	142

List of Tables

2.1	List of Type II Supernovae	12
2.2	Telescopes and instruments	14
2.3	Host-galaxy extinctions, distances and explosion times for the sample of SNe II-P	17
4.1	Coefficients of the fits to BC	54
4.2	Coefficients of the fits to T_{eff}	59
5.1	Properties of model M19R8E1.25NI56	68
5.2	Physical parameters for SN 1999em from three hydro-codes	82
5.3	Low mass models parameter	91
6.1	Observed Parameters for SNe II-P	106
6.2	Parameters of the grid of models	121

Contents

Resumen	i
1 Introduction	1
1.1 Supernova Background	1
1.2 Type II-Plateau SNe	5
1.3 This thesis	10
2 Sample of supernovae	11
2.1 Observations	13
2.2 AKA Corrections and Distances	13
2.3 Time Reference Frame	15
3 Hydrodynamical Code	18
3.1 Calculation Method	19

3.1.1	Equations for radiation transport and hydrodynamics	19
3.1.2	Input physics	24
3.1.3	Gamma-ray Deposition	28
3.1.4	Initial models	29
3.2	Code structure	36
3.3	Discussion on the approximations	38
4	Comparison with observables	42
4.1	Analysis of BC and T_{eff} -color relations	43
4.1.1	Bolometric Luminosity Calculations	44
4.1.2	Bolometric corrections versus Color	50
4.1.3	Effective Temperature-Color Relation	55
4.2	Photospheric velocities	59
5	Hydro-Model for SN 1999em	62
5.1	High-Mass Model of SN 1999em	63
5.1.1	Shock wave propagation and the early evolution	67
5.1.2	Adiabatic cooling and homologous expansion	71

5.1.3	Cooling and recombination wave	73
5.2	Comparison with other hydro-models of SN 1999em	82
5.3	Low Mass Model of SN 1999em	83
6	Observed and Physical Properties	92
6.1	Application to SN II-P Data	93
6.1.1	Plateau Luminosity: L_p	107
6.1.2	Plateau duration: Δt_p	109
6.1.3	Luminosity drop: $\Delta \log L$	112
6.1.4	^{56}Ni mass: M_{Ni}	115
6.2	Grid of Hydrodynamical Models	119
6.3	Observed and Modeled Correlations	126
7	Summary	137
A	Finite Difference Approximations	141
A.1	Computational grid	141
A.2	The Difference Equations	142
B	Solution of Gamma-ray transfer	147

Chapter 1

Introduction

1.1 Supernova Background

A supernova (SN, hereafter) explosion is among the most spectacular events that can be observed in the Universe. The term “supernova” is somewhat misleading, as such an event does not represent a new star (that is, a “nova”), but instead the death of a star.

The first records on supernovae (SNe) goes back to the second century A.D., mainly by Chinese astronomers. They observed and recorded “guest stars” , i.e., stars that suddenly appeared in the sky, were visible for a certain length of time, and then faded away. The “guest stars” that were visible for a year or longer were probably SNe, while the shorter guests were common novae. Among the most famous historical SNe are the events of 1054 A.D. (the “Crab Nebula”), 1572 A.D. (“Tycho’s supernova”), and 1604 A.D. (“Kepler’s supernova” which appeared only few years before the invention of the telescope). Another SN, known as Cas A (Cas for Cassiopeia), exploded in our galaxy between 1650 and 1680. Its remnant is a very strong radio source but, intriguingly, was not reported by contemporary observers.

The occurrence of this phenomenon became more familiar to astronomers at the end of the 19th century, with the beginning of the use of photographic plates and systematic surveys. Astronomers designated these objects with the genuine name “nova”. By 1927 ~ 100 novae had been discovered in the magnitude range 16–18. However, it was not until the distances to the nearby galaxies were firmly established through the observation of Cepheid variables (Hubble, 1925) that the separation of ordinary novae and the extraordinary luminous SNe, became clear.

The first physical explanation for SNe was proposed by Baade and Zwicky (1934). They suggested that the SN energy comes from the collapse of ordinary stars into neutron stars. This idea is a prescient suggestion for the fate of massive stars, but it is not the correct explanation for all types of SNe. Nature has more than one way to explode a star. This was revealed clearly by Minkowski (1941) who noted that the spectra of SNe indicated at least two different types of objects. One group, which he named “Type I”, was characterized by broad emission features and no signs of hydrogen in the spectrum, while the rest, named “Type II”, showed strong, broad hydrogen lines dominating the spectrum. Since that time, the classification of SNe has evolved parallel to the increasing body of spectroscopy data and our knowledge about these objects. In the mid-1980s it was realized that the Type I group could be further differentiated according to the presence of the Si II $\lambda 6355$ line. If this line was present in the spectra, the SN was classified as Type Ia; otherwise it was designated as Type Ib or Ic, depending on the presence or absence of He lines, respectively. Another critical piece of information about the nature of these objects was provided by the stellar environments where they were discovered. Supernovae of types II, Ib and Ic are only observed near star forming regions in late-type galaxies, which indicates their association with young stellar environments, while Type Ia SNe (SNe Ia) occur both in elliptical and spiral galaxies. Currently, it is accepted that there are two different physical types: the thermonuclear explosion of a white dwarf star in a binary system, and the gravitational collapse of the core of a massive star, as suggested by Baade and Zwicky (1934). The latter are called “core-collapse SNe” (CCSNe) and observationally correspond to SNe II, Ib and Ic. SNe Ia correspond to the first group of thermonuclear SNe.

Unlike SNe Ia, CCSNe form a diverse group in terms of their spectral and

photometric properties. SNe II have been subdivided according to their light curve shapes into: II-Plateau (showing plateau-like light curves), and II-Linear (showing linearly declining light curves). Further subgroups arise from spectroscopic properties: IIn (showing narrow emission lines), and IIb (showing hydrogen initially but afterward evolving to hydrogen-deficient at later times). There are some SNe Ib/c associated with long gamma-ray bursts (Woosley & Bloom, 2006) which show much broader lines than the typical objects of this class. They have been referred to as “hypernovae” or broad-lined SNe, due to the large inferred kinetic energies. Figure 1.1 shows a diagram of the current SN classification, as provided by Turatto (2003). A review of SN classification criteria is given by Filippenko (1997). It should be noted that, because of its empirical nature, the current classification scheme is prone to evolve as more data are obtained.

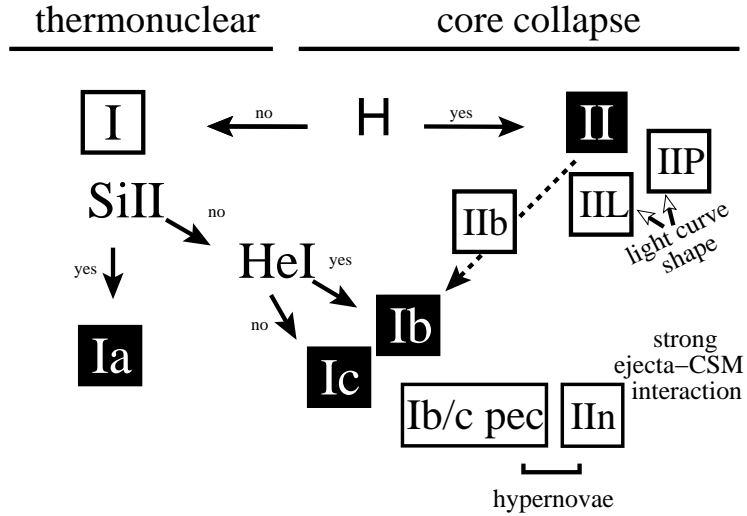


Figure 1.1: The current classification scheme of supernovae. Type Ia SNe are associated with the thermonuclear explosion of accreting white dwarfs. Other SN types are associated with the core collapse of massive stars. CCSNe with explosion energies $E > 10^{52}$ erg are often called hypernovae.

A typical SN has a luminosity of $\sim 10^{10} L_{\odot}$ during a period of weeks to months, which is comparable to the luminosity of its host galaxy. This radiative energy corresponds to only 0.01% of their typical kinetic energy which is $\sim 10^{51}$ erg (a quantity commonly known as 1 foe or, more recently, as 1 Bethe). The kinetic energy is essentially determined from the observed expansion velocities, as measured

from spectral lines. The characteristic broad P-Cygni profiles in SN spectra, with mean expansion velocities of the order to 10^4 km s^{-1} , is an indicator of fast-expanding atmospheres. In addition, the observed temperatures near maximum brightness are $\sim 2 T_{\odot}$, (where T_{\odot} stand for the effective temperature of the Sun), which implies radii $\sim 10^5 R_{\odot}$, assuming spherical symmetry and that the SN radiates as a black body. For the case of CCSNe, the kinetic energy represents only 1% of the energy released during the explosion. The remaining 99% ($\sim 10^{53} \text{ erg}$) is carried away by neutrinos created during the collapse of the core. Such an explosion mechanism was first confirmed with the detection of neutrinos from SN 1987A. This famous SN discovered on February 23, 1987 in the Large Magellanic Cloud (LMC) was the brightest SN detected since the invention of the telescope and one of the most extensively observed stellar objects in the history of astronomy. It was observed in all wavelengths from gamma rays to radio wavelength, and for the first time, extra solar neutrinos were detected. It presented a peculiar light curve shape which we know now that was due to the blue supergiant nature of the progenitor star, later identified on photographic plates of the LMC obtained prior to the explosion.

During the SN explosion a fraction of the progenitor's material is thermonuclearly burned into various elements. Among these products, unstable isotopes of iron-group elements play an important role in the subsequent evolution of the object. The most abundant radioactive isotope produced is ^{56}Ni which decays in ^{56}Co that in turn decays to stable ^{56}Fe . This process provides an additional source of energy which is thermalized in the ejecta and later released during a period of weeks to months.

Given their large intrinsic luminosity, SNe have long been considered potential probes for extragalactic distance determination and thus for the measurement of cosmological parameters that describe the expansion history of the Universe. Historically, SNe Ia have been used for this purpose due to their high degree of homogeneity. Through an empirical correlation found by Phillips (1993) between the absolute peak luminosity and the width of the light curve, SNe Ia can be used to determine distances with a precision of $\sim 7\%$ (Hamuy et al., 1996). One decade ago, the application of this method to high-redshift SNe Ia in comparison with the low-redshift sample of the Calán/Tololo survey led to the remarkable finding of the *accelerated* expansion of the

Universe (Riess et al., 1998; Perlmutter et al., 1999). Although, SNe II-P are fainter and less homogeneous than SNe Ia, they have also been proposed as good distance indicators with potential application to cosmology, in an independent way as SNe Ia. The most popular methods in the literature are the expanding photosphere method (EPM; Eastman et al., 1996; Dessart & Hillier, 2005a), the spectral-fitting expanding atmosphere method (SEAM; Mitchell et al., 2002; Baron et al., 2004), and the standard-candle method (SCM; Hamuy & Pinto, 2002). The former two methods require detailed atmospheric modeling, while the SCM is a much simpler approach based on an empirical correlation between luminosity and expansion velocity at the middle of the plateau phase. In principle, EPM and SEAM provide distances which are independent of the standard cosmic “distance ladder”, whereas SCM requires an external calibrator in order to provide absolute distances. By comparing low- and high-redshift samples, SCM can be potentially employed to determine cosmological parameters using data from upcoming SN surveys.

Recently, a compilation of all SN discoveries within a volume of 28 Mpc during a period of time of 10.5 yr has provided us the relative rates of each sub-type of SNe (Smartt et al., 2009). This study showed that SNe Ia represent only 27% of all SNe. The rest are CCSNe with the following rates: 59% for SNe II-P, 29% for SNe Ib/c, 5% for SNe IIb, 4% for SNe IIc and 3% for SNe IIL.

The goal of this thesis is the study of SNe II-P and their progenitors. In § 1.2 I review our current knowledge on these objects focusing on the motivations for this work. In § 1.3, I summarize the main goals of this thesis and I give a brief overview of each of its chapters.

1.2 Type II-Plateau SNe

Type II-Plateau SNe (SNe II-P) form a well-defined family characterized by a “plateau” in the optical light curve (Barbon et al., 1979), where the luminosity remains nearly constant for a period of ~ 100 days (see Figure 1.2), and the presence of prominent P-Cygni hydrogen lines in the spectrum (see Figure 1.3). They are a subclass of

the core-collapse SNe (CCSNe) —which includes Type Ib, Type Ic, and other subclasses of type II SNe— originated by the violent death of stars with initial masses greater than $8 M_{\odot}$ (Heger et al., 2003; Smartt et al., 2009) and sharing, in general terms, the same explosion mechanism. It has been shown that SNe II-P are the most common type of SNe in nature, amounting to 59% of all CCSNe. Apart from their astrophysical importance in connection with stellar evolution and the physics of the interstellar medium, additional interest on SNe II-P has recently arisen from the fact that they have been established as good distance indicators with potential application to cosmology, independent of Type Ia SNe (see § 1.1).

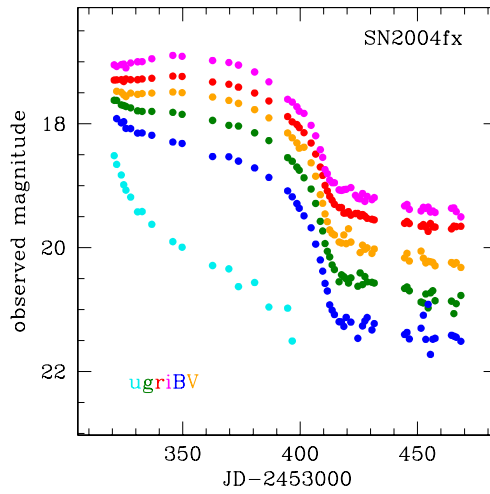


Figure 1.2: Light curve SN 2004fx, a typical SN II-P

Massive stars may suffer considerable mass loss during the early phases of their evolution, due to strong stellar winds or transfer to binary companions. Thus, they may lose part or all of their outermost envelope of unprocessed hydrogen and helium. The vast diversity observed among CCSNe is related with the properties of the progenitor star. In the current picture, SNe II result from progenitors which are able to retain a significant fraction of their external hydrogen layers and possibly have the least massive progenitor of all CCSNe. This picture is combined with hydrodynamical models of SNe II-P, which show that a red supergiant progenitor with an extensive H envelope is necessary in order to reproduce the plateau-shaped light curves (Grassberg et al., 1971; Falk & Arnett, 1977; Chevalier, 1976). Recent

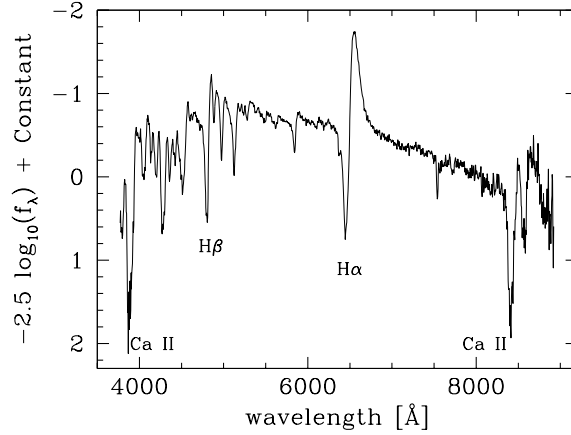


Figure 1.3: Spectra of SN 2004fx, a typical SN II-P

direct detection of the progenitors of several SNe II-P suggest in fact that SNe II-P arise from red supergiant stars with $M_{ZAMS} < 18M_{\odot}$ (Van Dyk et al. (2003); Smartt et al. (2004) and Smartt et al. (2009)).

There is general agreement that the explosion of a massive star is originated by the collapse of its central parts into a neutron star or black hole when the iron core is formed at the end of the star evolution, and further nuclear burning no longer provides thermal pressure to support the star. During the explosion, the heavy elements (mostly α -nuclei) synthesized inside the SN progenitor over its life are spread at very high speed into the interstellar medium. Despite the intensive theoretical modeling done during recent years (see Burrows et al., 2006; Janka et al., 2007, and references therein) the mechanism that transfers the energy released during the collapse of the core to the envelope, still remains unknown. The approach usually adopted to model CCSNe is to decouple the explosion into two independent parts: a) the core collapse and the subsequent formation of a shock wave, and b) the ejection of the envelope. Based on the analysis of the propagation of the shock wave through the envelope, independently of how the shock is formed, it is possible to study the observational outcome of the explosion such as light curves and spectra. This approach has been extensively used (Falk & Arnett, 1977; Grassberg et al., 1971; Woosley, 1988, among others) and has led to the conclusion that the main factors influencing the outcome are the explosion energy and the progenitor properties (mass and radius).

Observationally, SNe II-P show a wide range of plateau luminosities (L_p) and durations (Δt_p), expansion velocities (v_{exp}), and nickel masses (M_{Ni}) (Young & Branch, 1989; Hamuy, 2001). The morphology of the light curve (LC) of SNe II-P has been shown to be connected with physical properties of the progenitor object such as ejected mass (M), explosion energy (E), and pre-supernova radius (R). The relations between these physical and observable parameters were first derived analytically by Arnett (1980) and then generalized by Popov (1993). Numerical calibrations of these relations were then given by Litvinova & Nadezhin (1983, 1985) (LN83 and LN85 hereafter, respectively) based on a grid of hydrodynamical models for different values of M , R and E . Hamuy (2003) and Nadyozhin (2003) applied such calibrations to a set of ~ 20 SN II-P and thereby derived masses, radii and explosion energies for their sample. However, these studies have not been fully satisfactory owing to 1) the lack of good-quality data, 2) the use of simplified relations between ill-defined and hard-to-measure photometric and spectroscopic parameters, and 3) the fact that some of the models are based on simplified physical assumptions. Some of the weaknesses of the LN83 and LN85 models are that they did not include the effect of nickel heating in their calculations, the use of old opacity tables, the neglect of any effect from line opacities, and the simplified initial pre-supernova models adopted.

This thesis was motivated by the need to remedy such problems in order to improve our knowledge of the physical properties of SN II-P progenitors. Furthermore, the availability of an enlarged data set of *BVI* light curves and spectra of ~ 30 SNe II-P (Hamuy et al., 2010) justifies a detailed study. To accomplish our purpose, we have developed our own hydrodynamical model (Bersten et al., 2010) which allows us to perform a comparison between models and data in a consistent way.

During the development of this thesis there have been important advances in this field. For example, Utrobin (2007) performed a detailed analysis of SN 1999em and also studied how several physical parameters affect the LC. In that work, the author provided relations between physical and observed parameters for SNe II-P similar to SN 1999em. More recently, Kasen & Woosley (2009) calculated a set of model LC and spectra of SNe II-P, for different masses, metallicities, and explosion energies. They used their models to describe the dependence of plateau luminosity

and duration on explosion energy and progenitor mass. Nevertheless, the relations they found are simple and easy to apply *only* in the extreme case of no ^{56}Ni production. When ^{56}Ni is considered, the relations involve more parameters, which hinders their applicability to obtain physical parameters from observations. Other works have also explored the effect of several physical parameters on the LC and other observational properties of SNe II-P (Chieffi et al., 2003; Young, 2004), although without attempting to derive general relations. In recent years, there has been a number of works which analyzed the physical properties of individual SNe II-P based on hydrodynamical models (Baklanov et al., 2005; Utrobin & Chugai, 2009, among others).

In addition to the comparison with hydrodynamical models, there is an alternative way to derive progenitor masses of SNe II-P, namely, using pre-supernova images to search for the progenitor star and measuring its brightness and color to derive a mass in connection with a stellar evolution model. The last decade has witnessed direct discoveries of several SN progenitors providing a remarkable and rapid progress in this field. Currently, there are three SNe II-P (SN 2003gd, SN 2005cs and SN 2008bk) with a firm detection of the progenitor and ~ 17 others without a positive detection (see Smartt et al. (2009) for a review). The latter cases are still useful since they provide upper limits to the progenitor masses. These studies have suggested a minimum of the stellar mass for SNe II-P of $8 \pm 1 M_{\odot}$ and a maximum of $16.5 \pm 1.5 M_{\odot}$. Although there seems to be consensus on the lower mass limit of mass for SNe II-P, the upper limit derived by this method is systematically lower than the progenitor masses derived by modelling the light curves, as noted by Utrobin & Chugai (2008) and Smartt (2009). Specifically, there are three SNe II-P with hydrodynamical masses which have been studied in pre-supernova imaging (namely, SN 1999em, SN 2004et and SN 2005cs) and a few more that have been studied using semi-analytical models. In all cases the mass estimated by hydrodynamical models is higher than the estimate or upper limit given by pre-supernova imaging. This discrepancy poses a very interesting and unsolved problem which is necessary to address.

1.3 This thesis

Supernovae are very relevant astrophysical objects: they affect the energetic and chemical evolution of galaxies, and are also important distance indicators for cosmology. Determining what ranges of physical parameters (masses, radii and energies) give rise to each type of CCSNe is still an open question. One way to estimate such parameters is by comparing observations (light curves, colors, spectra) with hydrodynamical models. In addition to this, the LC provides a useful tool to test models of stellar evolution of massive stars and unveil the internal structure (chemical composition, mixing and mass distribution) of the progenitor object. Furthermore, models may provide a theoretical explanation for the correlations that are employed in the determination of distances to SNe II-P, and guide future refinements of this technique.

The main goal of this thesis is the development of a one-dimensional, Lagrangian hydrodynamic code to model bolometric light curves of SNe II-P with the ultimate purpose of analyzing the physical properties of an available large sample of SNe with highly-precise, well-sampled observations.

I have organized the thesis as follows. In Chapter 2, I give a description of the sample of ~ 30 SNe II-P used in this study, the sources of the data, corrections for extinction and distances. In Chapter 3, I present our one-dimensional, flux-limited, Lagrangian hydrodynamical code for the modeling of bolometric light curves of SNe II-P. The micro-physics and pre-supernova models used in our calculation are also described in Chapter 3. More technical details of the calculations are given in appendices A and B. In Chapter 4, I explain the method used to compute bolometric corrections (BC) for SNe II-P which are necessary to derive bolometric light curves from BVI photometry, this allows us to compare our model with observations. In Chapter 5, I analyze the case of the prototype SN 1999em, and discuss how our model compares with previous hydrodynamical studies of this object. In Chapter 6, I derive bolometric LC for our sample of SNe and derive physical parameters for this sample. I also study the correlations between different observables. Finally, in Chapter 7, I summarize the main conclusions of this work.

Chapter 2

Sample of supernovae

One of the main motivations for this thesis is the availability of an unprecedented data set of *BVI* light curves and spectra of ~ 35 SNe which offers the opportunity to significantly improve our understanding of SNe II-P and their progenitors. This sample of SNe II-P was observed in the course of four systematic follow-up programs: the *Cerro Tololo Supernova Program* (1986-2003), the *Calán/Tololo Supernova Program* (CT; 1990-1993), the *Optical and Infrared Supernova Survey* (SOIRS; 1999-2000), and the *Carnegie Type II Supernova Program* (CATS; 2002-2003). Additionally, I included four SNe from the literature: SN 1999gi (Leonard et al., 2002), SN 2004dj (Vinkó et al., 2006), SN 2004et (Sahu et al., 2006), and SN 2005cs (Pastorello et al., 2006; Tsvetkov et al., 2006). Complementary photometry for SN 2003gd obtained by Van Dyk et al. (2003) and Hendry et al. (2005) was also incorporated. A complete listing of the SNe used in this work is given in Table 2.1 where I present the SN, host galaxy name, the SN equatorial coordinates, the heliocentric redshift of the host galaxy and their sources, the extinction due to our own Galaxy (Schlegel et al., 1998) and the corresponding reference for the photometric and spectroscopic data of each supernova.

TABLE 2.1: LIST OF TYPE II SUPERNOVAE

SN Name	Host Galaxy	α (J2000)	δ (J2000)	z_{host}^a	(s) ^b	$E(B - V)_{\text{Gal}}$	References
1991al	LEDA 140858	19 42 24.00	-55 06 23.0	0.01525	HP02	0.051	1
1992af	ESO 340-G038	20 30 40.20	-42 18 35.0	0.01847	NED	0.052	1
1992am	MCG -01-04-039	01 25 02.70	-04 39 01.0	0.04773	NED	0.049	1
1992ba	NGC 2082	05 41 47.10	-64 18 01.0	0.00395	NED	0.058	1
1993A	anonymous	07 39 17.30	-62 03 14.0	0.02800	NED	0.173	1
1999br	NGC 4900	13 00 41.80	+02 29 46.0	0.00320	NED	0.024	2
1999ca	NGC 3120	10 05 22.90	-34 12 41.0	0.00931	NED	0.109	2
1999cr	ESO 576-G034	13 20 18.30	-20 08 50.0	0.02020	NED	0.098	2
1999em	NGC 1637	04 41 27.04	-02 51 45.2	0.00267	NED	0.040	2
1999gi	NGC 3184	10 18 17.00	+41 25 28.0	0.00198	NED	0.017	3
200210	MCG +00-03-054	01 01 16.80	-01 05 52.0	0.05140	NED	0.036	4
2002fa	NEAT J205221.51	20 52 21.80	+02 08 42.0	0.06000	NED	0.099	4
2002gw	NGC 922	02 25 02.97	-24 47 50.6	0.01028	NED	0.020	4
2002hj	NPM1G+04.0097	02 58 09.30	+04 41 04.0	0.02360	NED	0.115	4
2002hx	PGC 23727	08 27 39.43	-14 47 15.7	0.03099	NED	0.054	4
2003B	NGC 1097	02 46 13.78	-30 13 45.1	0.00424	NED	0.027	4
2003E	MCG -4-12-004	04 39 10.88	-24 10 36.5	0.01490	J09	0.048	4
2003T	UGC 4864	09 14 11.06	+16 44 48.0	0.02791	NED	0.031	4
2003bl	NGC 5374	13 57 30.65	+06 05 36.4	0.01459	J09	0.027	4
2003bn	2MASX J10023529	10 02 35.51	-21 10 54.5	0.01277	NED	0.065	4
2003ci	UGC 6212	11 10 23.83	+04 49 35.9	0.03037	NED	0.060	4
2003cn	IC 849	13 07 37.05	-00 56 49.9	0.01811	J09	0.021	4
2003cx	NEAT J135706.53	13 57 06.46	-17 02 22.6	0.03700	NED	0.094	4
2003ef	NGC 4708	12 49 42.25	-11 05 29.5	0.01480	J09	0.046	4
2003fb	UGC 11522	20 11 50.33	+05 45 37.6	0.01754	J09	0.183	4
2003gd	M74	01 36 42.65	+15 44 20.9	0.00219	NED	0.069	4,5,6
2003hd	MCG -04-05-010	01 49 46.31	-21 54 37.8	0.03950	NED	0.013	4
2003hg	NGC 7771	23 51 24.13	+20 06 38.3	0.01427	NED	0.074	4
2003hk	NGC 1085	02 46 25.76	+03 36 32.2	0.02265	NED	0.037	4
2003hl	NGC 772	01 59 21.28	+19 00 14.5	0.00825	NED	0.073	4
2003hn	NGC 1448	03 44 36.10	-44 37 49.0	0.00390	NED	0.014	4
2003ho	ESO 235-G58	21 06 30.56	-48 07 29.9	0.01438	NED	0.039	4
2003ip	UGC 327	00 33 15.40	+07 54 18.0	0.01801	NED	0.066	4
2003iq	NGC 772	01 59 19.96	+18 59 42.1	0.00825	NED	0.073	4
2004dj	NGC 2403	07 37 17.00	+65 35 58.1	0.00044	NED	0.040	7
2004et	NGC 6946	20 35 25.30	+60 07 18.0	0.00016	NED	0.342	8
2005cs	NGC 5194	13 29 53.40	+47 10 28.0	0.00154	NED	0.035	9,10

^a Heliocentric host-galaxy redshifts

^b Sources of host-galaxy redshifts. HP02: Hamuy & Pinto (2002); J09: Jones et al. (2009); NED: NASA/IPAC Extragalactic Database

References. (1) *Calán/Tololo Supernova Program*; (2) SOIRS; (3) Leonard et al. (2002); (4) CATS; (5) Van Dyk et al. (2003); (6) Hendry et al. (2005); (7) Vinkó et al. (2006); (8) Sahu et al. (2006); (9) Pastorello et al. (2006); (10) Tsvetkov et al. (2006)

2.1 Observations

The observations were made with telescopes from *Cerro Tololo Inter-American Observatory* (CTIO), *Las Campanas Observatory* (LCO), the *European Southern Observatory* (ESO) in La Silla and the *Steward Observatory* (SO). Table 2.2 shows the telescopes and instruments used to obtain the photometry and spectroscopy of this data set. CCD detectors and standard Johnson-Kron-Cousins *UBVRIZ* filters (Johnson et al., 1966; Cousins, 1971; Hamuy, 2001) were employed in all the cases, and for a small subset of SNe, observations in the *JHK* filters were also obtained. Additionally, low resolution optical spectra were taken for each SN at various epochs using CCD detectors in combination with different gratings/grisms and blocking filters. Currently, all of the optical data and spectra have been reduced and they are in course of publication (Hamuy et al., 2010). The data reductions were performed using IRAF¹ procedures including, among others, the host galaxy subtraction (for more details, see also Hamuy, 2001).

2.2 AKA Corrections and Distances

In order to study the physical properties of our SNe and to compare them with each other it is necessary to correct the observed magnitudes by host-galaxy extinction (A_{host}), redshift (K -correction), and Galactic extinction (A_G) dubbed AKA corrections as described in detail by Olivares et al. (2009). It is also important to place all of the SNe in the same distance scale by correcting for systematic differences among the different distance estimate methods.

The AKA corrections and distances for most SNe were calculated by Olivares et al. (2009). While the determination of Galactic extinction is straightforward using the IR dust maps of Schlegel et al. (1998) and assuming a standard reddening law as

¹IRAF is distributed by the National Optical Astronomy Observatories, which are operated by Association of Universities for Research in Astronomy, Inc., under cooperative agreement with the the National Science Foundations

Table 2.2: Telescopes and instruments used in the photometric and spectroscopic observations

Telescope	Instrument	Spec/Phot ^a
CTIO 0.9m	CCD	P
YALO 1.0m	ANDICAM	P
YALO 1.0m	2DF	S
CTIO 1.5m	CCD	P
CTIO 1.5m	CSPEC	S
Blanco 4.0m	CSPEC	S
Blanco 4.0m	2DF	S
Blanco 4.0m	CCD	P
Swope 1.0m	CCD	P
du Pont 2.5m	WFCCD	S/P
du Pont 2.5m	MODSPEC	S
du Pont 2.5m	2DF	S
du Pont 2.5m	CCD	P
Baade 6.5m	LDSS2	S/P
Baade 6.5m	B&C	S
Clay 6.5m	LDSS2	S/P
ESO 1.52m	IDS	S
Danish 1.54m	DFOSC	S/P
ESO 2.2m	EFOSC2	S
NTT 3.58m	EMMI	S
ESO 3.6m	EFOSC	S
Kuiper 61"	CCD	P
Bok 90"	B&C	S

^a Whether the instrument was used for photometry (P), spectroscopy (S) or both (S/P).

that given by Cardelli et al. (1989), with $R_V = 3.1$, determining the extinction due to host-galaxy dust is a more difficult task. Olivares et al. (2009) addressed this issue by assuming that all SNe II-P should evolve to a similar asymptotic intrinsic color at the end of the plateau phase. This is expected because of the hydrogen recombination nature of the photosphere. Therefore, color indices measured at the end of the plateau can be used to determine reddening by comparing with a sample of unreddened SNe II-P.

The distances to this sample are determined using the Standardized Candle Method (SCM), with the exception of SN 2003ef and SN 2005cs. For SN 2003ef I adopted the EPM distance estimated by Jones et al. (2009), converted to the distance scale of Olivares et al. (2009) using the conversion coefficients given by the authors. The resulting value is 48.55 ± 18.4 Mpc. For SN 2005cs, I used the distance modulus of $\mu = 29.62 \pm 0.25$ mag given by Pastorello et al 2006, which corresponds to 8.4 ± 1 Mpc. Table 2.3 shows host-galaxy extinctions and distance moduli for our sample of SNe.

2.3 Time Reference Frame

An additional important step which is necessary in order to compare the data of different SNe is to place them in a consistent reference frame of time. This is achieved by establishing an origin of time for each SN which places time intervals for the observations of all SNe on uniform basis. Time intervals are then corrected for time dilation using the redshift of each SN.

A natural choice of the origin of time would be the moment of the explosion. However, there are only 12 SNe in the sample with an accurate estimate of the explosion time (t_0) based on EPM and pre-explosion imaging (Jones et al., 2009). These estimates were obtained using two independent atmospheric models by Eastman et al. (1996) and Dessart & Hillier (2005a) (E96 and D05 hereafter, respectively), which led to two different values of t_0 for each SN. In Table 2.3 I show both values of t_0 for those 12 SNe II-P. I use additional information of the explo-

sion time found in the literature for SN 1991al, SN 199af, SN 1992am, SN 1993A, SN 1999ca, and SN 1999cr (see Table 2 of Hamuy, 2003). For SN 2003gd a value of $t_0 = 4716.5 \pm 21$ given by Smartt et al. (2004), for SN 2004dj a value of $t_0 = 5167 \pm 21$ given by Vinkó et al. (2006), for SN 2004et a value of $t_0 = 5270.5 \pm 2$ (Sahu et al., 2006), and finally for SN 2005cs a value of $t_0 = 5549.9 \pm 1$ given by Pastorello et al. (2006). All these values of t_0 are given respect to $\text{JD} = 2448000$.

An alternative approach was introduced by Olivares et al. (2009). In such work, the origin of time was defined as the moment at the middle point of the transition between the plateau and the radioactive tail (t_{PT}). The values of t_{PT} for the sample of SNe are given in Table 2.3. With this definition, I was able to place all the SNe of our sample in a common time frame. Both origins of time, t_0 and t_{PT} , are used in this thesis, depending on the context of the analysis.

Table 2.3: Host-galaxy extinctions, distances and explosion times for the sample of SNe II-P

SN Name	A_V^a	μ^a	$t_0(\text{E96})^b$ [JD-2448000]	$t_0(\text{D05})^b$ [JD-2448000]	t_{PT}^c [JD-2448000]
1991al	-0.17(21)	34.05(28)	521.998
1992af	-0.37(21)	34.15(28)	858.583
1992am	0.52(23)	36.57(025) ^d	947.43
1992ba	0.30(21)	31.33(28)	883.9(3)	879.8(5.6)	1013.714
1993A	0.06(25)	35.59(04) ^d	1106.96
1999br	0.94(25)	31.86(31)	...	3275.6(7.7)	3395.508
1999ca	0.25(21)	33.29(11) ^d	3373.19
1999cr	0.12(21)	34.56(28)	3348.88
1999em	0.24(21)	30.00(28)	3476.3(1.1)	3474.0(2)	3590.136
1999gi	1.02(21)	30.50(28)	3517.0(1.2)	3515.6(2.4)	3647.759
0210	0.31(36)	37.31(31)	4591.917
2002fa	-0.35(26)	37.16(29)	4576.632
2002gw	0.18(22)	33.41(28)	4557.9(2.7)	4551.7(7.6)	4662.195
2002hj	0.24(22)	34.93(28)	4660.231
2002hx	0.38(22)	35.49(28)	4657.707
2003B	-0.09(21)	32.18(27)	4713.878
2003E	0.78(23)	34.01(28)	4765.663
2003T	0.35(21)	35.17(28)	4654.2(2.7)	4648.9(3.4)	4759.381
2003bl	0.26(21)	34.07(30)	...	4692.6(2.8)	4804.609
2003bn	-0.04(21)	33.60(28)	4693.4(2.7)	4687.0(9)	4817.0
2003ci	0.78(23)	35.30(38)	4817.720
2003cn	-0.04(23)	34.81(28)	4804.986
2003cx	-0.27(25)	36.20(29)	4830.927
2003ef	0.98(21)	33.43(1.2) ^e	4759.8(4.7)	748.4(15.6)	4869.095
2003fb	1.24(23)	34.49(29)	4874.252
2003gd	0.33(21)	29.98(28)	4840.108
2003hd	0.01(21)	35.86(28)	4953.053
2003hg	1.97(24)	33.31(28)	4998.604
2003hk	0.44(25)	34.41(28)	4957.908
2003hl	1.72(23)	32.04(28)	4872.3(1.7)	4865.4(5.9)	5006.708
2003hn	0.46(21)	31.13(27)	4859.5(3.8)	4853.8(9.3)	4962.898
2003ho	2.19(21)	34.13(28)	4919.688
2003ip	0.56(22)	33.76(28)	5002.872
2003iq	0.25(22)	32.43(28)	4909.6(4.3)	4905.6(9.5)	5019.625
2004dj	-0.09(23)	28.14(29)	5286.428
2004et	0.13(27)	28.37(31)	5389.0
2005cs	0.72(30)	29.62(0.25) ^f	5665.705

^a Host-galaxy extinctions and distance moduli calculated by Olivares et al. (2009).

^b Explosion times calculated by Jones et al. (2009) using two atmospheric models (E96 and D05).

^c Times at the middle point of the transition between the plateau and the radioactive tail, as calculated by Olivares et al. (2009).

^d Redshift adopting $H_0 = 68$.

^e EPM distance estimated by Jones et al. (2009), converted to the distance scale of Olivares et al. (2009).

^f Distance modulus given by Pastorello et al 2006.

Chapter 3

Hydrodynamical Code

The main part of my thesis work is devoted to develop a one-dimensional hydrodynamic code in order to model bolometric light curves of SNe II-P. Due to the difficulty of modelling the core collapse from first principles, the approach extensively used in the literature, and followed in this work, is to decouple the SN explosion problem in two independent parts: a) the core collapse and formation of the shock wave (SW), and b) the ejection of the envelope. Although the exact nature of the mechanism that rips the object in two parts is not clear, the great differences in energetics and time scales (seconds for the collapse and days for the ejected envelope) allow the theoretical description of a SN II explosion to be separated into internal and external problems. The energy transferred to the envelope (which we called explosion energy) plays the role of a coupling parameter between the internal and external parts of problem. In addition, the processes which control the envelope ejection and the supernova radiation do not depend on how the energy is transferred to the envelope as long as this process occurs in a short enough time. Based on the propagation of the SW through the envelope, independently of how the shock is formed, it is possible to study the observational outcome of the explosion, such as light curves and spectra.

In § 3.1, I describe the numerical method, equations, micro-physics and ini-

tial models used to compute bolometric light curves of SNe II-P. That Section is complemented by Appendices A and B which provide a technical description of the methods. The structure of the code is presented in § 3.2. A discussion of the adopted approximations is given in § 3.3.

3.1 Calculation Method

Our supernova models are computed by numerical integration of the hydrodynamical equations assuming spherical symmetry for a self-gravitating gas. Radiation transport is treated in the diffusion approximation with the flux-limited prescription of Levermore & Pomraning (1981). The explosion is simulated by injecting a certain amount of energy near the center of the progenitor object during a very short time as compared with the hydrodynamic time-scale. This energy induces the formation of a powerful shock wave that propagates through the progenitor transforming thermal and kinetic energy of the matter into energy that can be radiated from the stellar surface. To calculate shock waves, we include, as is usually done, an artificial-viscosity term in the equations of moment and energy.

The equations and numerical method used are discussed in § 3.1.1. In § 3.1.2 I give a description of the constitutive relations included in the code. The energy deposited by radioactive decay is discussed in § 3.1.3. Finally, in § 3.1.4 the initial models are described.

3.1.1 Equations for radiation transport and hydrodynamics

The differential equations that describe the hydrodynamics and radiative transfer of the system assuming spherical symmetry and diffusion approximation in Lagrangian coordinates are: (a) velocity definition,

$$\frac{\partial r}{\partial t} = u, \quad (3.1)$$

(b) mass conservation,

$$V = \frac{1}{\rho} = \frac{4\pi}{3} \frac{\partial r^3}{\partial m}, \quad (3.2)$$

(c) momentum conservation,

$$\frac{\partial u}{\partial t} = -4\pi r^2 \frac{\partial}{\partial m} (P + q) - \frac{Gm}{r^2}, \quad (3.3)$$

(d) energy conservation,

$$\frac{\partial E}{\partial t} = \epsilon_{\text{Ni}} - \frac{\partial L}{\partial m} - (P + q) \frac{\partial V}{\partial t}, \quad (3.4)$$

and (e) radiative energy transport,

$$L = -(4\pi r^2)^2 \frac{\lambda_{ac}}{3\kappa} \frac{\partial T^4}{\partial m}, \quad (3.5)$$

where m is the Lagrangian mass coordinate chosen as independent variable in place of the radius (r) to describe the structure of the object, u is the velocity, V is the specific volume, P is the total pressure (of gas and radiation), and q is the artificial viscosity which is included in the equations to spread the pressure and energy over several mass zones at the shock front. There are many expressions for the artificial viscosity, all dependent on the velocity gradient, which aim at providing a convenient interpolation scheme between unshocked and shocked fluid. We adopt the expression given by Von Neumann & Richtmyer (1950) (see Appendix A). E is the total internal energy per unit of mass, including gas and radiation, ϵ_{Ni} is the energy deposited by the radioactive decay of nickel as I describe in § 3.1.3. In equation (3.4) we do not consider other sources of cooling or heating, such as losses due to neutrino processes or energy released by thermonuclear reactions, because the energy of the SW overwhelms these other sources. Even if neutrinos are very important in the formation of the shock wave as the explosion depends noticeably on the efficiency of their energy transfer, most of them are emitted before the shock wave reaches the stellar photosphere, so they have no effect on later epochs of the SN evolution

(see Hillebrandt, 1990; Burrows, 1991; Janka et al., 2007). The energy released by explosive nucleosynthesis is much less than the energy of the shock wave as has been previously established [Imschenik & Nadezhin (see 1965); Woosley & Weaver (see 1990); Arnett (see 1996)]. T is the temperature of both matter and radiation, κ is the Rosseland-mean opacity and L is the luminosity. Finally, λ is the so-called “flux-limiter”, included in the diffusion equation to ensure a smooth transition between diffusion and free-streaming regimes to assure causality. The expression adopted for λ is,

$$\lambda = \frac{6 + 3R}{6 + 3R + R^2}, \quad (3.6)$$

where

$$R = \frac{|\nabla T^4|}{\kappa \rho T^4} = \frac{4\pi r^2}{\kappa T^4} \left| \frac{\partial T^4}{\partial m} \right|. \quad (3.7)$$

Note that when $\kappa \rho \rightarrow \infty$ (short mean free path), $R \rightarrow 0$ and $\lambda \rightarrow 1$ as expected for the diffusion limit. But as $\kappa \rho \rightarrow 0$ (long mean free path), $R \rightarrow \infty$ and $\lambda \rightarrow 3/R$. Thus, it can be seen that the flux is limited to the value $c a T^4$, as required physically. However, flux-limited diffusion is not the correct solution for radiation transfer in optically thin regions; it is simply an interpolation between the physically correct optically thick and thin limits.

The quantities E , P , and κ are functions of ρ , T , and chemical composition. Further details on these constitutive relations are given in § 3.1.2.

The overall problem is to solve the complete structure of the object, i.e., determining the dependent variables r , u , V , T , and L as a function of m and time. Therefore, the problem reduces to solving a system of five coupled partial differential equations (3.1)–(3.5) together with the constitutive relations (see § 3.1.2) and the expression for q , λ and ϵ_{Ni} (see § 3.1.3). In addition, it is also necessary to provide boundary and initial conditions. The boundary conditions that we have adopted are:

$u = 0$ near the center (at $m = M_{\text{core}}$, where we typically set $M_{\text{core}} = 1.4 M_{\odot}$), and $P_{\text{gas}} = \rho = 0$ at the surface ($m = M$). As initial condition, we have used different initial models (see § 3.1.4), in hydrostatic equilibrium. As discussed above, we simulate the explosion by artificially adding internal energy almost instantaneously in the central region of the core.

We have developed a code in FORTRAN to numerically solve this system of differential equations using the method of finite differences. As a first step, it is necessary to discretize each equation in order to transform the system of differential equations into an algebraic one. It is important to note that the discretization process is not trivial as there is no unique way to discretize a differential equation (Bowers & Wilson, 1991). Details of the discretization and the scheme of integration are given in Appendix A. Here, I remark that the code uses a space-centering discretization with the extensive quantities evaluated at the interfaces and the intensive quantities in the midpoints of the grid zones. Two time steps are adopted in each cycle: one to advance the velocity, and the other to advance the material state variables. The time step is chosen to comply with stability and accuracy constraints (see the discussion below). Special care is taken in the centering of the opacity when discretizing equation (3.5) in order to prevent numerical noise to appear due to the propagation of the radiation flow at the steep front where the opacity changes significantly (Christy, 1967).

Depending on how the time derivatives of the differential equations are numerically evaluated, we have different schemes of integration. For example, given the equation,

$$\frac{\partial f(x, t)}{\partial t} = g(f, x, t), \quad (3.8)$$

in a single time step the numerical scheme advances the solution from time t (where we known the solution) to time $t + \Delta t$. The advanced solution can in general be written as

$$f(t + \Delta t) \simeq f(t) + \Delta t((1 - \theta) g(t) + \theta g(t + \Delta t)). \quad (3.9)$$

If $\theta = 0$ the scheme is called *explicit* (or forward time differencing) and it involves only known values of the functions at time t . In other cases, with θ between 0.5 and 1, the scheme is called *implicit* and the solution involves the initial unknown function $f(t + \Delta t)$, requiring an iterative technique to find the solution. More specifically, when $\theta = 1$ the scheme is called fully implicit (or backward time differencing) and the case of $\theta = 0.5$ is usually known as centered time differencing. Although, the *explicit* schemes are easier to solve than the *implicit* ones, the former have a stringent requirement on the time step used in the calculation in order to ensure the stability of the numerical scheme. This requirement is known as the *Courant condition*, which states that $\Delta t < \Delta x/v$ where Δx is the width of the grid zone and v is a characteristic speed which in hydrodynamics problems is adopted as the sound speed. Physically, this condition states that the information may not spread through the grid at a speed greater than the characteristic speed defined by the problem.

In our code, we use an explicit scheme for the integration of the hydrodynamic equations, but a semi-implicit scheme for the temperature, similar to the one used by Falk & Arnett (1977). The equations are linearized in δT and solved iteratively for each time step using the tridiagonal method (see Appendix A). The discretization typically uses 300 mesh points, with a finer sampling for the outer layers typically smaller than $10^{-6}M_{\odot}$. This value was chosen based on tests performed with our model and following previous works (Woosley, 1988; Ensman & Burrows, 1992) which show that the early light curve is sensitive to the mass zoning in the outer layers when a coarse grid is used.

Given that we are using an explicit hydrodynamic scheme, the time step should be chosen as a fraction of the minimum of the Courant condition for all zones in order to achieve stability. I note that we have also imposed additional conditions on the time step: we have required that changes in temperature, density and flux over one time step be less than 5%.

The formation of the shock wave (SW) following core collapse is simulated by artificially adding internal energy (“thermal bomb”) almost instantaneously in the inner region of the core. We usually set a mass cut of $1.4 M_{\odot}$ which the material assumed to collapse and form a neutron star or black hole. In order to do this, we have included an additional term in the energy equation 3.4 of the form, $dE_{exp}/dm = C \exp(-t/\tau) \exp(-m/m_0)$. This expression was arbitrarily chosen but its integral is exactly the explosion energy which is free parameter of our model. We have also tested explosions generated by injecting kinetic energy (in this case it is necessary to include an additional term in the Euler equation 3.3) and we have obtained similar results. The latter method, however, leads to very short numerical time steps, and therefore to slower calculations. We have checked the accuracy of our calculation method by testing the conservation of energy. The total amount of energy is conserved within 0.6% but if we consider the conservation of energy between two consecutive time steps, this is within 4×10^{-6} . We consider it very adequate for our purposes.

3.1.2 Input physics

The equation of state (EOS) is calculated using simple expressions for T , ρ , composition, and for the ionization degrees of hydrogen and helium which are computed assuming local thermodynamical equilibrium (LTE). Therefore, the degree of ionization is determined by solving the corresponding set of Saha equations for ionization of hydrogen and the first and second ionization of helium. Ionization of heavy elements is neglected in our EOS (but, of course, it is taken into account in the calculation of the opacity). In general, our EOS consists of two terms, the radiation and gas contribution. The latter can be also divided into electron and ion terms. Thus, for example the total pressure is written as,

$$P = P_{Rad} + P_{Gas} = P_{Rad} + P_{e-} + P_{ion} \quad (3.10)$$

with

$$P_{Rad} = \frac{a}{3}T^4, \quad P_{ion} = \frac{R}{\mu}\rho T \quad (3.11)$$

where μ is the molecular weight for the non-ionized material. The electron pressure, P_{e-} , is a much more complicated function. It is influenced by the degree of ionization (determined by Saha equation) and degeneracy effects. We calculate the pressure of degeneracy using the method described by Kippenhahn et al. (1968), although the condition of degeneracy is rarely reached in our calculation. We tested our results using a more sophisticated EOS, such as that of the Los Alamos Tables (Rogers et al., 1996), and we did not find any significant difference with respect to the results obtained using our simple EOS. This is expected due to the low densities attained in most of the layers of the models.

The Rosseland mean opacity, κ , is a function of T , ρ (or P) and chemical composition. There are tables available in the literature that provide the opacity for a wide range of T , ρ and chemical composition. In our calculations we use the OPAL opacity tables (Iglesias & Rogers, 1996, and references therein). As these tables are given for $T > 6 \times 10^3$ K, we complement them with the opacity tables provided by Alexander & Ferguson (1994) for lower temperatures which includes molecular opacities. The tables are interpolated in order to guarantee a smooth transition at $T = 10^4$ K from one to the other.

These tables allow us to calculate opacities for several metallicities. Also, for a fixed metallicity, different mixtures of H, He, C and O can be used. Although in this work we adopt a fixed value of $Z = 0.02$, departures from this value (as expected in the inner regions of the object) are taken into account as excesses of C and O with respect to the values of the adopted metallicity, at the expense of He.

Figure 3.1 shows the opacity given by the tables as a function of temperature for $Z = 0.02$ and different densities. The range of temperature shown corresponds to the values reached during the evolution of a SN II-P while the values of density are restricted to those achieved during the plateau phase. Also shown in the plot is the contribution to the opacity from electron scattering. Note that electron scattering

is the dominant source of opacity for $T > 10^4$ K and $\rho < 10^{-10}$ gr cm $^{-3}$.

The Rosseland mean opacity includes scattering and absorption processes. Scattering is the dominant process (see Figure 3.1) in the supernova ejecta until most of the electrons recombine with ions and absorption processes become an important source of opacity. On the other hand, in rapidly expanding envelopes where large velocity gradients are present, the Rosseland mean opacity underestimates the true line opacity (Karp et al., 1977), which hinders the estimation of the actual opacity in the outermost (recombined) layers. Another effect that is not included in the calculation of κ is non-thermal excitation or ionization of atoms/ions which is produced by Compton scattering of γ -rays emitted by radioactive decay of ^{56}Ni and ^{56}Co . The LTE ionization used in the calculation of κ considerably underestimates the true ionization. The correct way to treat these effects is to calculate the actual contribution of non-thermal ionization to the opacity and to include the expansion opacity of lines. However, such treatment is beyond the scope of this study. We adopt an alternative approach that has been extensively used in the literature (e.g., Shigeyama & Nomoto, 1990; Herzig et al., 1990; Swartz et al., 1991; Young, 2004) which consists of using a minimum value of the opacity (or “opacity floor”). The minimum opacity values adopted in this work are: 0.01 cm 2 g $^{-1}$ for the envelope material, and 0.24 cm 2 g $^{-1}$ for the metal-rich core material. These values were chosen by performing a comparison with results of the STELLA code. We found an excellent overall agreement between the light curves given by our code and STELLA (Blinnikov & Bartunov, 1993; Blinnikov et al., 1998) both in terms of the duration of the plateau and the morphology of the bolometric LC) when the previous values of the minimum opacity were adopted (see § 3.3. Note that STELLA is an implicit hydrodynamic code that incorporates multi-group radiative transfer, and additionally uses different opacity tables and includes the effect of line opacities (Sorokina & Blinnikov, 2002).

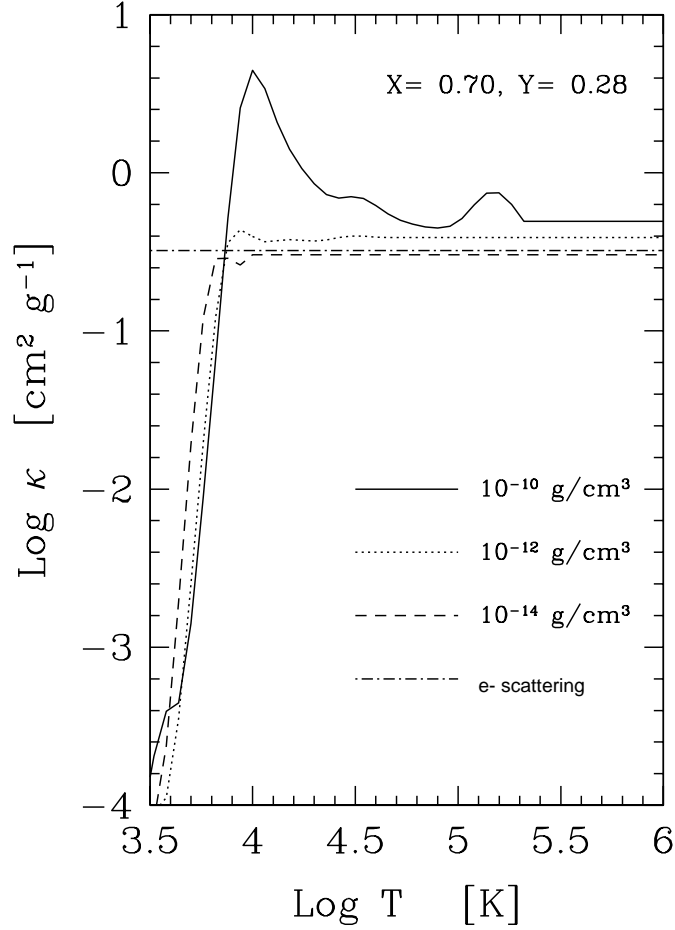


Figure 3.1: The run of the Rosseland opacity on temperature (T) and density (ρ) for solar metallicity ($Z = 0.02$) as used in our calculation without including any “opacity floor” (see discussion in Section 3.1.2). The ranges of T and ρ shown are typical for SNe II-P. The hydrogen (X) and helium (Y) mass fractions used are indicated. We also include the electron scattering opacity (considering full ionization, which is certainly unrealistic for the low temperature sector of this plot) in order to show the dominance of this source for $T > 10^4$ K and $\rho < 10^{-10}$ g cm⁻³. Note that this value of the density is reached early-on in the supernovae evolution. For lower temperatures the absorption processes become an important source of opacity.

3.1.3 Gamma-ray Deposition

During the explosive nucleosynthesis produced in supernova explosions, unstable isotopes of iron elements are formed. The decay of these isotopes and subsequent thermalization of the decay products generate extra energy that contributes to power the LC. The most abundant radioactive isotope produced is ^{56}Ni which decays with a 6.1 day half-life to ^{56}Co which in turn decays with a 77.7 day half-life to stable ^{56}Fe . The decays produce energetic γ -rays and positrons which are thermalized, providing the thermal luminosity of the SN.

In order to include this source of energy in the calculations, it is necessary to determine a local heating rate which generally is not the same as the simple radioactive decay rate. Instead, the decay rate should be modified by the probability of thermalization determined by the rate at which γ -rays and positrons deposit energy at various points in the gas as they travel through the ejecta. This problem is very complicated if tackled from first principles. A set of γ -ray transfer equations must be solved simultaneously with the hydrodynamic equations which requires a multiple-energy group Monte Carlo calculation. However, if the ejecta is optically thick to γ -rays, it is possible to assume that the gamma rays deposit their energy locally. Several studies of SNe II-P have previously assumed this hypothesis considering that the energy contribution of radioactive material is only relevant toward the end of the plateau phase. Such approach would be correct only if ^{56}Ni was deeply concentrated in the ejecta in which case gamma photons could hardly diffuse out of the regions where they form. We believe there is no justification to assume this type of ^{56}Ni distribution, as shown in studies of SN 1987A (Shigeyama et al., 1988; Woosley et al., 1988; Arnett, 1988; Blinnikov et al., 2000, among others) and the diffusion of gamma rays must be properly calculate from the location where they are emitted to the outer regions. To calculate this, we solve the gamma-ray transfer in the gray approximation for any spherically symmetric distribution of ^{56}Ni , assuming that gamma rays interact with matter only through absorption. Details of this calculation are presented in Appendix B. It has been shown by comparison with Monte Carlo simulations of Type Ia supernovae that the complex scattering process between gamma rays and electrons can be satisfactorily approximated as an

absorptive process (Sutherland & Wheeler, 1984; Swartz et al., 1995). The adopted value for the gamma-ray opacity is $\kappa_\gamma = 0.06 y_e \text{ cm}^2 \text{ g}^{-1}$, where y_e is the number of electrons per baryon.

The energy rate per gram released by Ni–Co–Fe decay is

$$\epsilon_{\text{rad}} = 3.9 \times 10^{10} \exp(-t/\tau_{\text{Ni}}) + 6.78 \times 10^9 [\exp(-t/\tau_{\text{Co}}) - \exp(-t/\tau_{\text{Ni}})] \text{ erg g}^{-1} \text{ s}^{-1}, \quad (3.12)$$

where $\tau_{\text{Ni}} = 8.8$ days, and $\tau_{\text{Co}} = 113.6$ days are the mean lifetimes of the radioactive isotopes. The amount of energy deposited at each point is given by the solution of the gamma-ray transfer multiplied by the previous expression. In Figure 3.2 we show the gamma-ray deposition¹ profile for the case of a polytrope with index $n = 3$, initial mass $10 M_\odot$ and different initial radii. The left panel is for a constant distribution of ^{56}Ni up to $3M_\odot$ and the right panel is for an exponential distribution of ^{56}Ni , also up to $3M_\odot$. Note that the diffusion of gamma rays from the region where they form becomes more noticeable as the object becomes more extended and diluted.

The possibility of using an arbitrary distribution of ^{56}Ni allows us to study different types of mixing and their effect on the resulting LC. As shown in 5.1.3, we find that radioactivity becomes an important source of energy, even during the plateau phase, if we allow an extensive mixing of ^{56}Ni .

3.1.4 Initial models

There are two different ways to determine the initial (or pre-SN) models: those coming from stellar evolution calculations (“evolutionary” models), or those from non-evolutionary calculations where the initial density and chemical composition

¹The deposition of gamma rays is defined by the energy deposited at each point normalized to the value corresponding to complete thermalization at the same location where the gamma rays are emitted.

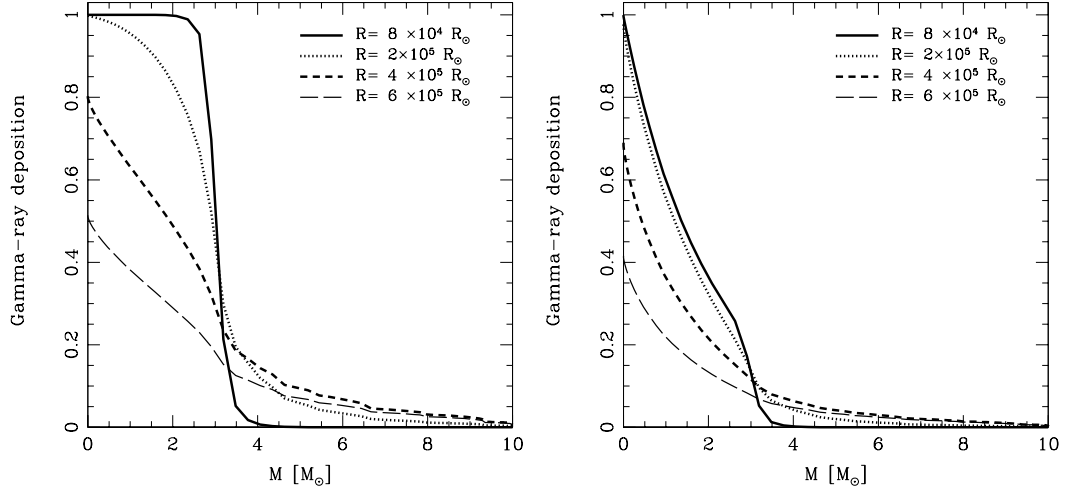


Figure 3.2: Gamma-ray deposition as a function of mass for a polytrope with index $n = 3$, initial mass $10 M_{\odot}$, and different initial radii. **(Left)** for a constant distribution of ^{56}Ni up to $3M_{\odot}$; **(right)** for an exponential distribution of ^{56}Ni , also up to $3M_{\odot}$. The diffusion of the gamma rays out of the region were they form becomes more noticeable as the object gets more extended and diluted.

are parameterized in a convenient way. Both types of models have been tested with our code.

As non-evolutionary models, we have calculated single and double polytropes. The single polytropic models were numerically computed by solving the “Lane-Emden” equation for any polytropic index (n). This allowed us to study many different configurations for different values of n , initial masses and radii, in hydrostatic equilibrium. Some examples of initial density profiles obtained using different polytropic indices are shown in Figure 3.3.

Although a single polytrope may represent very well the envelope of the real pre-supernova model, the inner dense part which is expected for this type of objects is not well reproduced with this simple initial model. One way to improve this situation is to consider two polytropes: one representing the inner dense core, and the other accounting for the outer extended envelope.

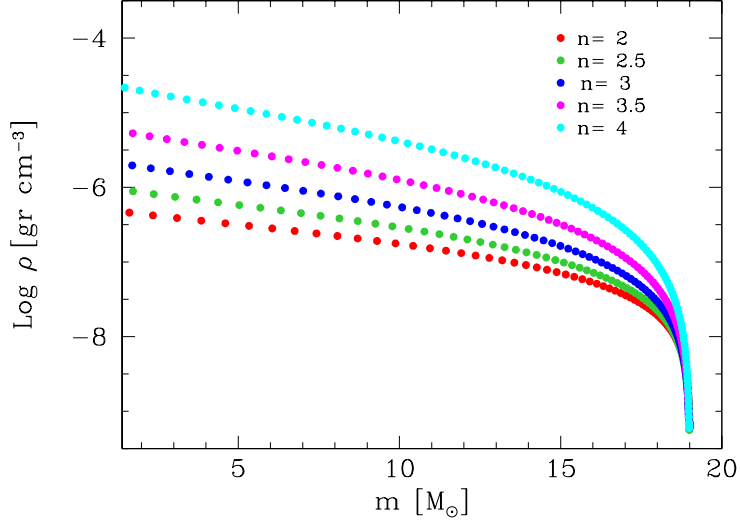


Figure 3.3: Density distribution as a function of mass for a single polytropic model using different polytropic indices, n , which are indicated in the plot. The total mass and radius in all the models are $19 M_{\odot}$ and $800 R_{\odot}$. Note that higher values of n produce more compact configurations.

The numerical calculation of double polytropic models is not trivial because the solution is extremely sensitive on the adopted initial guess value of the free parameters. Specifically, it is necessary to solve the equations of hydrostatic equilibrium and mass conservation assuming a polytropic approximation where the pressure has a dependence on density of the form: $P = K\rho^{\gamma} = K\rho^{n/(n+1)}$, where K is a constant and n is the polytropic index. Two different polytropic relations with different indices (n_i and n_o) and constants (K_i and K_o) are adopted to mimic the characteristic structure of a red supergiant. To calculate the composite polytrope, the previous equations are numerically integrated outward from the inner border (stellar core) to a pre-selected point (fitting point) using the internal polytropic relation. A second inward integration is done from the outer border (stellar surface) to the fitting point using the external polytropic relation. The problem is equivalent to a two-point boundary condition for the case where there are unknown free parameters at both ends of the domain. In our case, the free parameters are n_i , K_i and K_o , while the external index is fixed to $n_o = 3$. The inner boundary conditions are the central density (ρ_c) and the core mass (m_c), while the external boundary conditions are the

initial mass (M) and the external density (ρ_o). The integrations are performed along the radial variable r from r_c to R (radius of the object). The values of r_c , R , M and ρ_c are fixed for each configuration, while m_c , ρ_o are functions of the free parameters of the problem. Starting from initial guesses, the values of the free parameters are iteratively sought so that the solution joins smoothly at the fitting point. This process is performed using a shooting method (see Numerical Recipes, chapter 17). Once the values of n_i , K_i and K_o are found, the density (or pressure) distribution and mass distribution can be calculated. The initial temperature profile is calculated in an iterative fashion using our EOS to ensure hydrostatic equilibrium. This prevents the formation of a spurious shock wave.

Using this method a variety of initial models in hydrostatic equilibrium can be calculated by changing the fitting point, the initial mass, the radius or the central density as shown in Figures 3.4 and 3.5. The effect of the initial mass and fitting point on the density distribution is shown in Figure 3.4. The effect of the initial radius is shown in Figure 3.5. Note that different configurations can be obtained by changing the fitting point even if the initial mass and radius remain fixed. The same is valid if one changes the central density or the external polytropic index.

These parametric profiles allow us to study how the internal structure of the progenitor affects the LC. Figure 3.6 shows a comparison between LCs obtained using a single and a double polytropic model for an initial mass of $19 M_\odot$ and an initial radius of $800 R_\odot$. During the early part of the LC evolution ($t \lesssim 20$ days) both models are very similar. Significant differences appear later on. Note that the single polytropic models produce a prominent bump before the sharp decrease in luminosity which marks the end of the plateau. This bump is a consequence of the lack of a dense core in the initial model and is never observed in SNe II-P.

We have also calculated LCs using initial models derived from stellar evolution calculations. Pre-supernova models of four different sources were used: (1) “Supernova Science Center-UCSC” (<http://www.supersci.org/ucsc/>), (2) Limongi et al. (2000) (<http://web.oa-roma.inaf.it/localinfo/staff/webhost/limongi/data.html>), (3) **[Comment: Pedir cita a Omar:Benvenuto et al.]** and (4) Umeda & Nomoto (2005). Figure 3.7 shows the density distribution for some of these models. Also

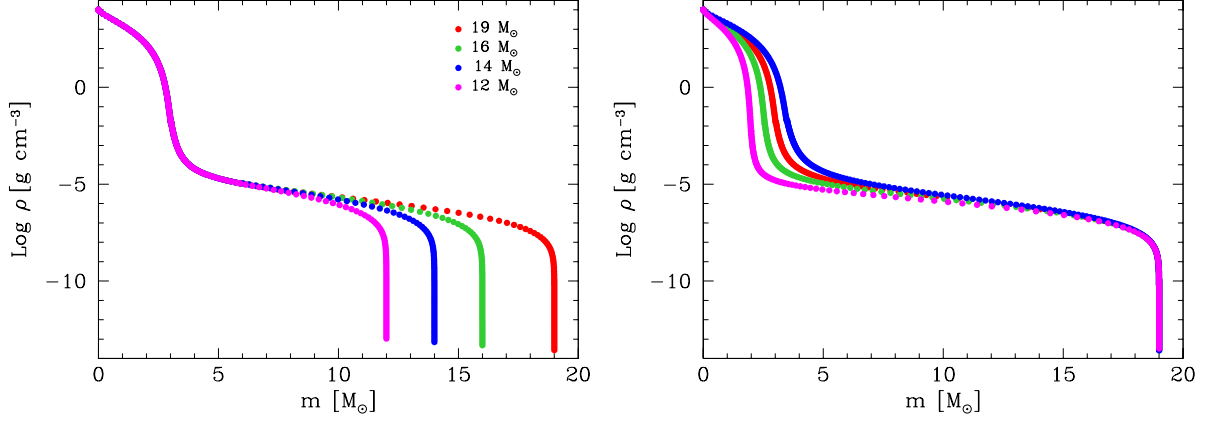


Figure 3.4: Density distribution of double polytropic models as a function of mass for a model with radius of $800 R_{\odot}$. **(Left)** The effect on the initial density of varying the mass. The values used in the calculation are indicated in the plot. **(Right)** The effect on the initial density of varying the fitting point for an mass of $19 M_{\odot}$. Note that even if mass and radius are the same, different configurations are obtained by changing the fitting point.

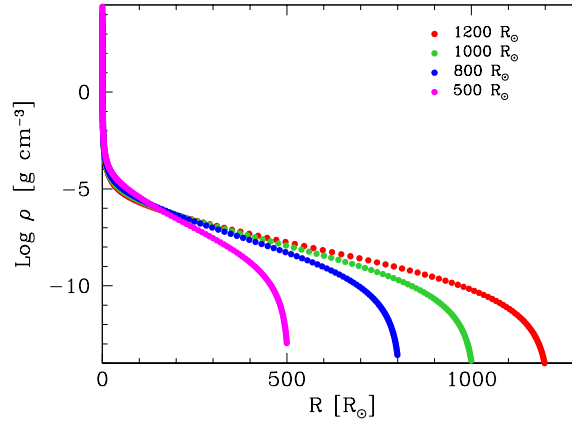


Figure 3.5: Density distribution of double polytropic models as a function of radius. The different curves represent different values of the radius used in the calculation for a fixed mass of $19 M_{\odot}$, as indicated in the plot.

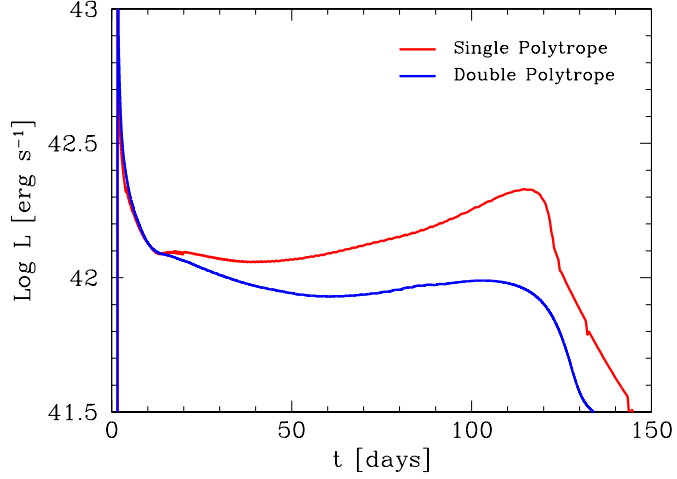


Figure 3.6: Comparison between the LC obtain using a single (red line) and double (blue line) polytrope. While the early LCs ($t \lesssim 20$ days) are very similar, important differences appear toward the end of the plateau.

shown for comparison the density distribution of a double polytropic model. The LC obtained using a pre-SN model of source (1) is shown in Figure 3.8. Note that some bumps appear around $t = 35$ days in the LC which are not present in observations. In § 3.3 a discussion using a pre-SN of source (4) is presented.

Having tested the code with various evolutionary initial models, I generally find better agreement with observations when using our parameterized double polytropic profiles, in concordance with previous studies that employ similar methods to compute the initial structure (Utrobin, 1993; Baklanov et al., 2005; Utrobin, 2007, among others). Thus is the approach adopted throughout the rest of this thesis.

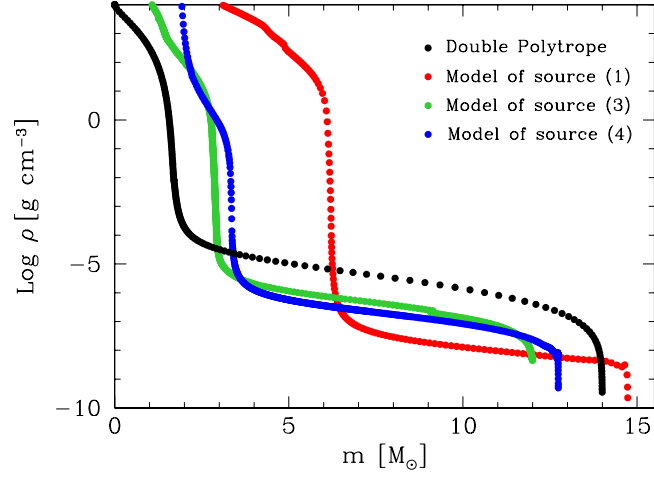


Figure 3.7: Initial density distributions from stellar evolution. The pre-SN models come from different sources, as indicated the text. A double polytropic model is also included for comparison.

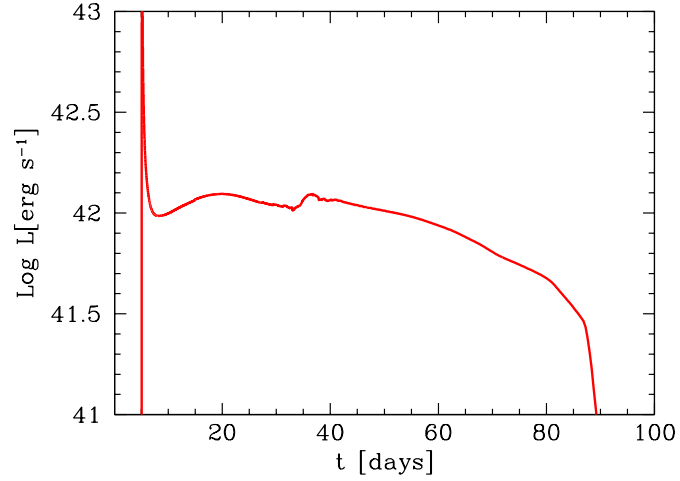


Figure 3.8: LC calculated using the initial model from stellar evolution calculations of the ‘Supernova Science Center-UCSC’. Note that some bumps appear in the LC around $t = 35$ days which are not present in observations.

3.2 Code structure

The code is organized in several subroutines with different hierarchy. Figure 3.9 schematically shows how our computational program is organized.

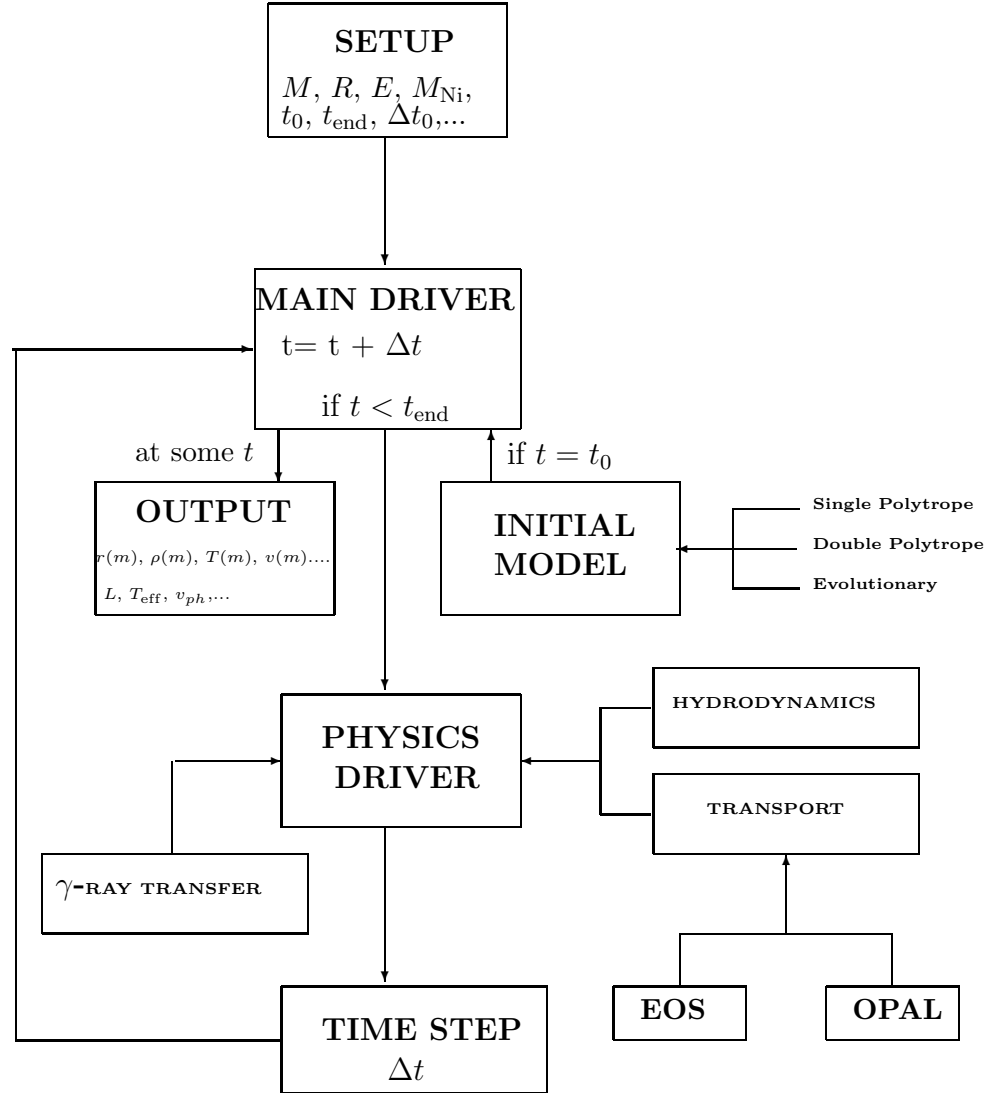


Figure 3.9: Code scheme

The main routine or “MAIN DRIVER” controls the program during the course of a calculation through a series of subroutine calls which are governed by logical

sentences based in part on the input information. The input of the program is represented in the “SETUP” block and includes the information necessary to generate a specific calculation. There, an input file is read containing the following information: type of initial model to use in the calculation (polytrope, double polytrope or evolutionary model), initial mass (M), radius (R), nickel mass (M_{Ni}), distribution of ^{56}Ni and explosion energy (E). The initial time step (Δt_0) and the ending time for the model calculations (t_{end}) are also included in this file. Other parameters which control the accuracy of the solution and the number of iterations allowed for the convergence of the iterative transfer calculations are also included there. The “PHYSICS DRIVER” block represents the piece of the code which calls subroutines that calculate the evolution of the physical quantities. Specifically, the following subroutines are called from this driver: (1) a routine to calculate the explicit hydrodynamic equations, (2) a transport routine which calculates the diffusion radiative transfer using an iterative method as described in Appendix A, and (3) the routine for solving the gamma-ray transfer (see Appendix B). The EOS and OPAL subroutines are called from the transport routine and represent the calculation of the equation of state and opacity. The results of the calculations, i.e., the model structure, $r(m)$, $P(m)$, $\rho(m)$, $T(m)$, etc., and the evolution of certain quantities such as bolometric luminosity, $L_{\text{bol}}(t)$, effective temperature, $T_{\text{eff}}(t)$, photospheric velocity, $v_{\text{ph}}(t)$, among others are written in output files at specific moments during the evolution. The writing process is schematically represented by the block “OUTPUT”. This subroutine is called from the “Main Driver” at the specific moments defined in the “SETUP” routine. After each step of calculation, a new step of time, Δt , is chosen in the “TIME STEP” block depending on stability and accuracy conditions. The “MAIN DRIVER” routine determines whether a new calculation is necessary, basically by checking that the new time step, $t = t + \Delta t$ is less than t_{end} . In that case, the whole process is repeated for time $t + \Delta t$.

Figure 3.10 shows a typical bolometric LC obtained with this code. The initial model used in the calculation is a double polytrope with initial mass $19 M_{\odot}$, initial radius $800 R_{\odot}$ and injected energy 1 foe (1×10^{51} erg s $^{-1}$). From the Figure it is possible to distinguish various phases: (1) a maximum in luminosity or “shock breakout”, (2) a phase where the luminosity is nearly constant or “plateau”, (3) a transition phase, and (4) a radioactive tail. These phases are studied in detail in

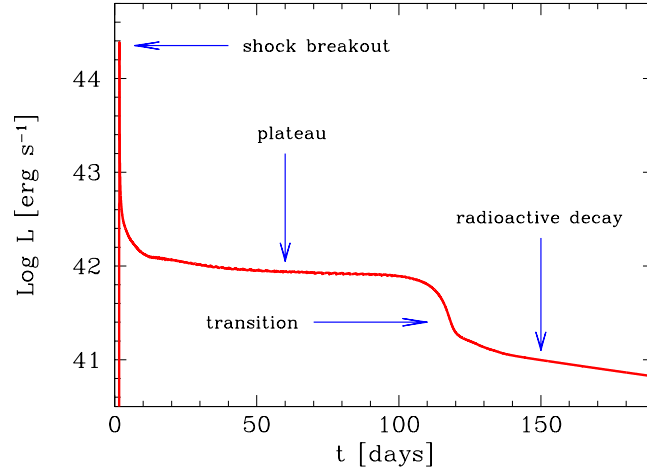


Figure 3.10: A typical bolometric LC of a SN II-P. The initial model used in the calculation was a double polytrope with initial mass $19 M_{\odot}$, initial radius $800 R_{\odot}$, and injected energy 1 foe. The different phases during the LC evolution are indicated in the plot.

3.3 Discussion on the approximations

Several approximations are made in the equations of radiation hydrodynamics. First, we assume that the fluid motion can be described by one-dimensional, radially symmetric flow. The explosion mechanism of core-collapse SNe is not well known. It may be an very asymmetric process. However, for this particular subtype of supernovae with very extended hydrogen envelopes the asymmetries expected from the explosion mechanisms itself appears to be smoothed. This is supported by recent spectropolarimetric studies (Leonard & Filippenko, 2005).

We use the equilibrium diffusion approximation to describe the radiative transfer. This approximation assumes that radiation and matter are strongly coupled with a single characteristic temperature and a spectral energy distribution described by a black body function (BB hereafter). The approximation breaks down at shock

breakout and at late phases when the ejecta is completely recombined and the object becomes transparent. Fortunately, during the plateau phase—which is our main interest—, this approximation is fairly adequate. Also note that non-LTE calculations of SN II spectra show that deviations from LTE have significant effects on spectral lines but not on the overall continuum (Baron et al., 1996; Dessart & Hillier, 2008). At late phases, for SNe that experience little interaction with the interstellar medium, as is the case of SNe II-P, the bolometric luminosity can be simply approximated as the luminosity deposited by the radioactive decay of ^{56}Co , at least during the early part of the radioactive tail. This is supported by the fact that the luminosity declines obeying an exponential law with a very similar rate to that of the decay of ^{56}Co . The radioactive scenario has been directly confirmed for SN 1987A through the detection of γ -ray lines from ^{56}Co (Matz et al., 1988). No attempt to apply our model beyond ~ 180 days is done.

During the transition between plateau and radioactive tail, the envelope is fully recombined and the notion of a photosphere loses meaning. Thus, this transition regime is poorly described with our radioactive transfer prescription and therefore a detailed analysis of this phase cannot be assessed here. As stated above, we have performed a comparison of our calculations with those of the STELLA code using the same initial model provided by Umeda & Nomoto (2005). We obtained an excellent agreement between the bolometric luminosities derived by both methods, as shown in Figure 3.11. This is very satisfactory considering that the STELLA code involves a more sophisticated treatment of the radiative transfer by solving these equations using a multi-group prescription and including the effect of line opacities (Blinnikov & Bartunov, 1993; Sorokina & Blinnikov, 2002).

Finally, I remark that the very good agreement obtained between both codes was reached using the values of opacity minimum (κ_{min}) mentioned in § 3.1.2, i.e. for the envelope material $\kappa_{\text{min}} = 0.01 \text{ cm}^2 \text{ g}^{-1}$. For other values of the opacity minimum commonly used in literature, the comparison with the STELLA code, which incorporates the effect of expansion opacity in the correct way, was not satisfactory. In order to show the effect on the LC of the value adopted for the opacity floor, I calculated models using three different values for the envelope material: $\kappa_{\text{min}}[\text{cm}^2 \text{ g}^{-1}] = 0.001, 0.01$ and 0.1 , as shown in Figure 3.12. Clearly, from this Figure, there

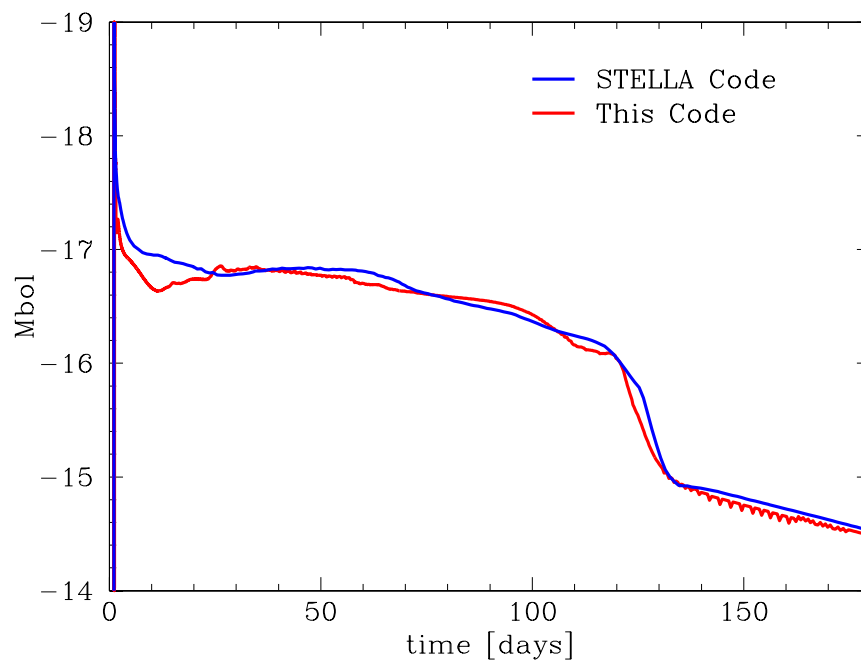


Figure 3.11: Comparison between the LC obtained with our code and the STELLA code. The initial model used was provided by Umeda & Nomoto (2005). Note the very good agreement between both LCs despite the simplifications employed here.

is a critical effect of the opacity minimum on the resulting LC. Hence, it should not be taken as a free parameter.

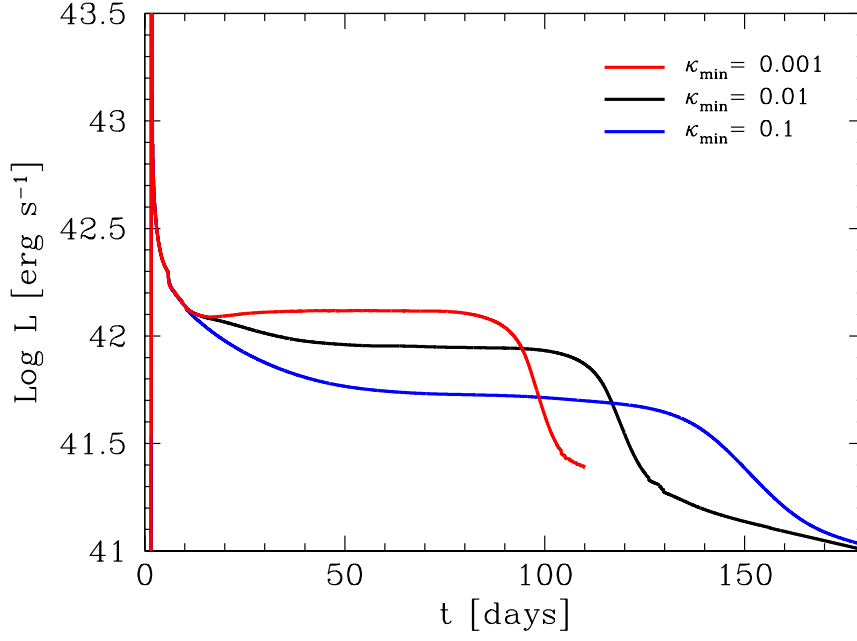


Figure 3.12: LC for three different values of the opacity minimum (κ_{\min} ; expressed in $\text{cm}^2 \text{g}^{-1}$ in the plot). Note the critical effect of the adopted opacity minimum on the LC. The value finally used in our code, $\kappa_{\min} = 0.01 \text{ cm}^2 \text{g}^{-1}$, was chosen by comparison to the STELLA code (see Figure 3.11)

Chapter 4

Comparison with observables

Since our code produces bolometric light curves and effective temperatures (T_{eff}) it proves necessary to calculate these quantities from the observed photometry in order to compare our model with observations. Although there are many SNe with optical observations, only a handful objects are available with observations over UV, optical and IR wavelengths. The purpose of this section is to use those SNe with observed bolometric light curves and explore the feasibility to derive a bolometric correction (BC) for other SNe with optical observations alone.

In §4.1, I present the calibrations derived for BC and T_{eff} from *BVI* photometry using data of three well-observed SNe II-P, SNe 1987A, 1999em and 2003hn, and two sets of atmosphere models by Eastman et al. (1996) and Dessart & Hillier (2005b) (E96 and D05 hereafter, respectively). The typical scatter of the BC is 0.11 mag and allows us to calculate bolometric luminosities for many other SNe II-P having *BVI* photometry alone, opening thus the possibility for a statistical analysis of the physical properties of this type of object (see also Bersten & Hamuy (2009)).

Additionally, the photospheric velocity is another useful parameter to compare with observations. In § 4.2, I describe the prescription used to compare the observed velocities with the photospheric velocities provided by our models.

4.1 Analysis of BC and T_{eff} -color relations

I begin this section by describing the observational and theoretical material used to calculate BC and T_{eff} . Then, in § 4.1.1 I proceed to calculate the bolometric luminosities for these data. Finally, in § 4.1.2 and § 4.1.3 I derive calibrations for BC and T_{eff} as a function of colors. Along this section, I refer to the SN evolution in terms of time or color indistinctly. This is well justified during the plateau phase in which the SN atmosphere expands, cools and monotonically turns redder.

In order to examine if a bolometric correction can be derived from optical colors, we made use of the three SNe II that possess the best wavelength and temporal coverage. Two of these are genuine SNe II-P, SN 1999em and SN 2003hn, and the third is the famous SN 1987A which, except for its peculiar light curve, shares most of the spectroscopic properties of SNe II-P. Most of the data of these three SNe were obtained at *Cerro Tololo Inter-American Observatory* (CTIO), *Las Campanas Observatory* (LCO), and the *European Southern Observatory* (ESO) at *La Silla*. For more details see Hamuy & Suntzeff (1990) and Bouchet et al. (1989) for SN 1987A, Hamuy et al. (2010) for SN 1999em, and Krisciunas et al. (2009) for SN 2003hn. The photometric bands used in this analysis were *UBVRIZJHK* for SN 1999em and SN 2003hn, and *UBVRIZJHKLM* for SN 1987A.

We adopt Cepheid distances for SN 1987A and SN 1999em with corresponding values of 50 kpc (Freedman et al., 2001) and 11.7 Mpc (Leonard et al., 2003). For SN 2003hn we used a distance of 16.8 Mpc, as derived by Olivares et al. 2008 using the Standardized Candle Method. We correct the photometry for Galactic and host-galaxy extinction. We perform such corrections using Galactic visual absorptions of $A_V^{GAL}=0.249$ for SN 1987A, $A_V^{GAL}=0.13$ for SN 1999em, and $A_V^{GAL}=0.043$ for SN 2003hn (Schlegel et al., 1998), assuming a standard reddening law with $R_V = 3.1$ as given by Cardelli et al. (1989). The values used for host-galaxy absorption are, $A_V^{host}=0.216$ for SN 1987A, $A_V^{host}=0.18$ for SN 1999em (Hamuy, 2001) and $A_V^{host}=0.56$ for SN 2003hn (Dessart, 2008), again assuming $R_V = 3.1$.

We also used in this analysis spectral energy distributions (SEDs) from two sets of SN atmosphere models (E96 and D05). These models depend on several parameters such as, luminosity, density structure, velocity and composition. For more details on the input parameters of such models the reader is referred to Eastman et al. (1996) and Dessart & Hillier (2005a). We use a total of 61 model spectra from E96, and 107 from D05. We discard 31 spectra from D05 which do not have enough UV coverage.

4.1.1 Bolometric Luminosity Calculations

By definition, the bolometric luminosity is the integral of the flux over all frequencies. This integration can be done in a straight-forward way for the spectral models of E96 and D05 summing the flux over wavelength. With the purpose to estimate bolometric corrections and colors for the models we compute *BVI* synthetic magnitudes using the filter transmission functions and zero points given by Hamuy (2001).

For the three well-observed SNe the calculation of bolometric luminosities is performed from reddening-corrected broadband magnitudes using the values mentioned in section 4.1. K-corrections are neglected due to the small redshifts involved. We began by computing a quasi-bolometric light curve using all the available broadband data. The magnitudes were converted to monochromatic fluxes at the specific effective wavelength of each filter using the transmission functions and zero points of the photometric system (Hamuy, 2001). At epochs when a certain filter observation was not available, we interpolated its magnitude in time using the closest points. The total “quasi-bolometric” flux, F_{qbol} was computed using a trapezium integration over $U - K$ for SN 1999em and SN 2003hn, and over $U - M$ for SN 1987A.

To estimate the missing flux in the UV and IR, F_{UV} and F_{IR} , we fit at each epoch a blackbody (BB) function to the monochromatic fluxes¹ as shown in Figure 4.1 for the case of SN 1999em at ~ 7 days post explosion. At early epochs the

¹These fits are restricted to the plateau phase where the envelope of the SN was optically thick, and also to the transition to the nebular phase. On the radioactive tail we did not use any UV or IR corrections.

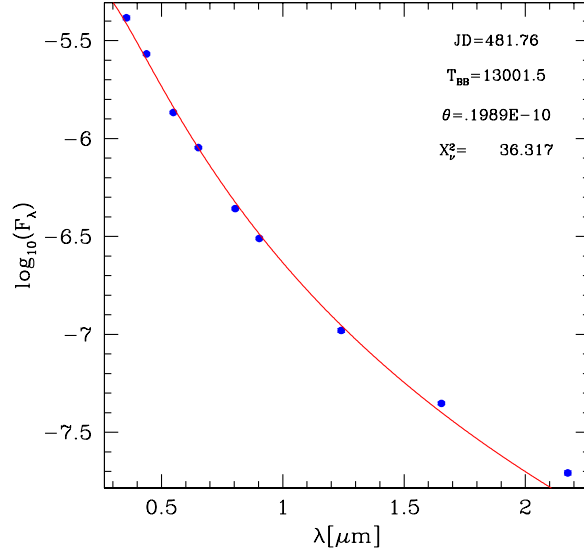


Figure 4.1: Blackbody (BB) fit to the monochromatic fluxes for the case of SN 1999em at ~ 7 days after explosion. The BB function provides a very good representation of the flux. The T_{BB} and θ shown in the inset are the color temperature and angular radius of the SN 1999em yielded by the BB fit.

BB model provided very good fits to the fluxes in all bands. As the photosphere became cooler the U -band flux started to depart from the BB model in which cases we exclude this point from the fit. At later epochs, subsequently the B -band and V -band data points show the same behavior, departing from the BB model. The reason for this is related to the strong line blanketing that develops with time in that part of the spectrum.

On the IR side the flux is extrapolated to $\lambda = \infty$ using the BB fits described above. The integral of that function between the longest observed effective wavelength and $\lambda = \infty$ is adopted as the IR correction (F_{IR}). This correction increase with time but always remains below 7% for the three SNe.

On the UV side, we extrapolate from the effective wavelength of the U band to $\lambda=0$ using the BB fit on all epochs except when the U -band flux falls below the BB model. In these cases, we extrapolate the U -band flux using a straight line to

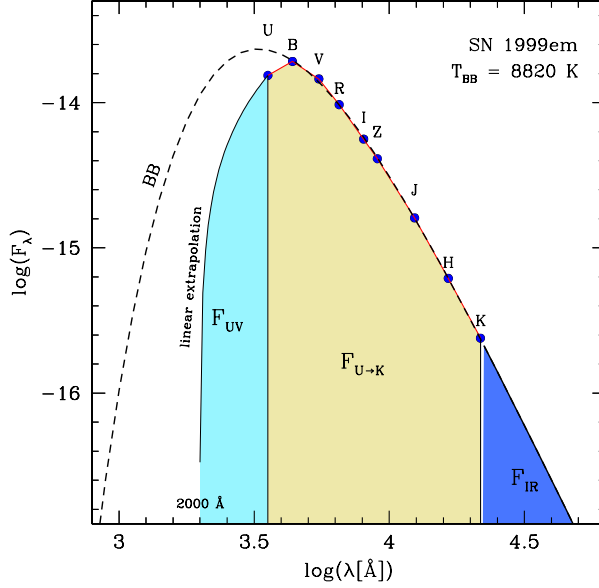


Figure 4.2: Contributions to the bolometric flux as employed this work. $F_{U \rightarrow K}$ is the “quasi-bolometric” flux computed by integration of all broad band available by each SN. F_{UV} and F_{IR} represents the UV and IR contribution calculated using a extrapolation of the BB fit to the broad band or a linear extrapolation.

zero flux at 2000 \AA . Our choice of $\lambda = 2000 \text{ \AA}$ as the wavelength where the flux goes to zero was based on the behavior of the atmospheric models for which the flux blueward of 2000 \AA is negligible in comparison with the total flux. The integrated flux under the Planck function (or straight line) between the effective wavelength of the U filter and $\lambda = 0$ (or $\lambda = 2000 \text{ \AA}$) is taken as the UV correction (F_{UV}). Figure 4.2 shows schematically the different contributions to the bolometric flux employed in this work.

The size of the F_{UV} correction relative to the total flux for the three SNe and the two sets of atmospheric models is shown in Figure 4.3 as a function of $(B - V)$. The first thing to note is the overall good agreement in F_{UV} between the observed SNe and the atmospheric models. Second, it is evident that the UV correction is very important at early epochs and becomes nearly irrelevant at the latest epochs. Thirdly, note that in the very blue end, where the UV corrections are of order 50-80%, there is some disagreement between the atmosphere models and SN 1999em.

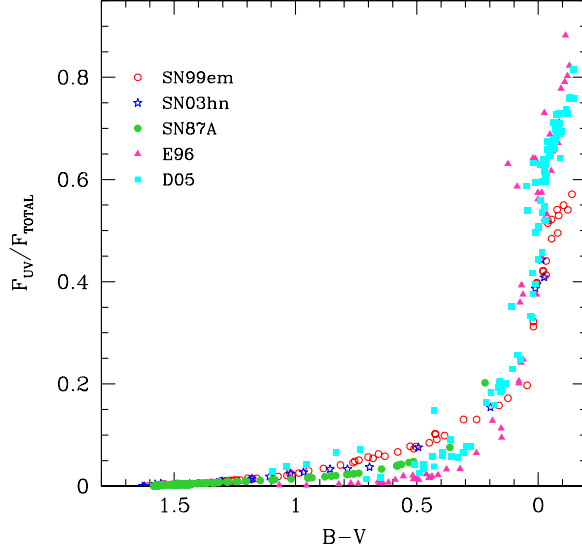


Figure 4.3: UV contribution to the total flux as a function of $(B - V)$ for SN 1987A, SN 1999em and SN 2003hn and for the models of E96 and D05. At early times, when $(B - V) \lesssim 0.2$, the UV flux represents a significant fraction of the total flux, implying larger uncertainties in the UV correction.

The spectral models suggest larger UV corrections and, as argued below, they are more trustworthy at these early epochs than the extrapolation of the broadband magnitudes. To prove this point, we calculate F_{UV} for the models using the same technique that we employ for SN 1999em, i.e. by computing synthetic magnitudes for all passbands, converting them to monochromatic fluxes, and fitting a BB to the resulting points (instead of the direct integration of the SED. In this case the UV correction proves closer to the UV correction derived from SN 1999em. We conclude that the UV extrapolation using the BB fits to the broadband magnitudes at very early epochs underestimates somewhat F_{UV} , so we end up using only the atmosphere models at such epochs. At later times ($B - V > -0.04$), where the differences between data and theory become negligible, we adopt both the models and the observed data.

The sum $F_{qbol} + F_{UV} + F_{IR}$ yields the bolometric flux F_{bol} (the integration under the solid curve of Figure 4.2). Then we transform flux into luminosity using the distances given in section 4.1. The resulting bolometric luminosities for SN 1987A,

SN 1999em and SN 2003hn are shown in Figure 4.4. As a comparison, the solid line shows the bolometric luminosity of the SN 1987A obtained by Suntzeff & Bouchet (1990). I find very good qualitative agreement between both bolometric light curves for SN 1987A. There is a systematic difference which remains smaller than 0.04 dex at all times between both calculations. Such differences are consistent with the uncertainties arising from the use of different photometric data sets and different integration and interpolation scheme.

As can be seen in Figure 4.4, the morphologies of the bolometric light curves for the three SNe are very different, especially that of SN 1987A which shows a broad maximum, not observed in classical SNe II-P, and a less luminous light curve (up to the transition to the radioactive tail). The peculiar light curve of SN 1987A is well known and is attributed to the fact that its progenitor was a compact blue supergiant that lead to a dim initial plateau and to a light curve promptly powered by radioactivity (Woosley, 1988; Shigeyama & Nomoto, 1990) . However, the three objects showed a similar initial phase of rapid fading and cooling until the outermost parts of the ejecta reached the temperature of hydrogen recombination (adiabatic cooling phase). A second phase can be distinguished for SN 1999em and SN 2003hn which corresponds to the plateau where the luminosity remained nearly constant while hydrogen was recombining. The duration and the slope of the light curve during this phase were different for each supernova. This is related to the properties of the progenitor object, mainly to the mass and radius of the hydrogen envelope. The shape of the light curve for SN 1987A during this phase was very different as mentioned above. It showed a broad maximum characterized by a slow rise of ~ 90 days followed by a more rapid decline for about 30 days. Finally, I can distinguish a third phase, the radioactive tail which has similar slope for all three SNe. Here, the luminosity exhibits a linear decline, and it is dominated by the radioactive decay of ^{56}Co into ^{56}Fe . The luminosity in this part of the light curve is a direct indicator of the amount of ^{56}Ni synthesized in the explosion (Woosley et al., 1989), the parent product of ^{56}Co . We deduce from this that SN 1987A produced more ^{56}Ni than the other two SNe.

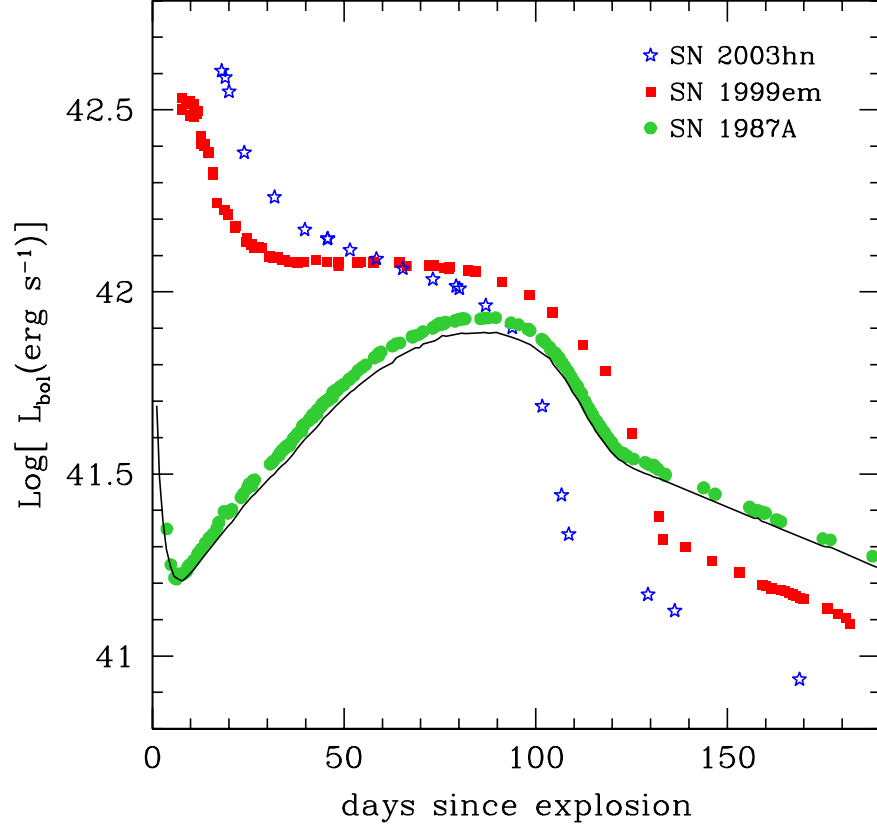


Figure 4.4: Bolometric luminosity of SN 1987A, SN 1999em and SN 2003hn computed from the integration of broadband optical and near-infrared data plus UV and IR contributions as explained in section 4.1.1. For comparison we include the bolometric luminosity of SN 1987A obtained by Suntzeff & Bouchet (1990)(solid line).

4.1.2 Bolometric corrections versus Color

There are many SNe that lack IR and UV observations for which it is not possible to calculate the bolometric luminosity using the method described in the previous section. For these cases it is necessary to know the bolometric correction required to convert a V -band magnitude into a bolometric flux, i.e.,

$$BC = m_{bol} - [V - A_V], \quad (4.1)$$

where A_V is the total visual extinction and m_{bol} is the bolometric magnitude in the Vega system. Note that, since BC is defined as a magnitude difference, it is independent of the distance assumed for each object.

We calculate BC at all epochs for each of the calibrating SNe and all of the SN models using the bolometric luminosities computed in section 4.1.1. The bolometric fluxes were converted into Vega magnitudes in the following manner,

$$m_{bol} = -2.5 \log_{10} F_{bol} + 11.64, \quad (4.2)$$

where the zero point is obtained by integrating the SED of Vega given by Hamuy(2001) and forcing the resulting magnitude to vanish, i.e., $m_{bol}(\text{Vega}) = 0$.

We analyzed the dependence of the BC on color, using $(B - V)$, $(V - I)$ and $(B - I)$. The main reason why we did not try colors involving the R band is because our sample (Hamuy et al., 2010) has few SNe with R -band observations. Figures 4.5 and 4.6 show the resulting corrections as a function of the mentioned colors (corrected for dust) for SN 1987A, SN 1999em, SN 2003hn, and the models of E96 and D05. In each of these plots the vertical bar indicates the approximate color corresponding to the end of the plateau. To the red of this mark are shown the BC corresponding to the transition between the plateau and the radioactive tail for the

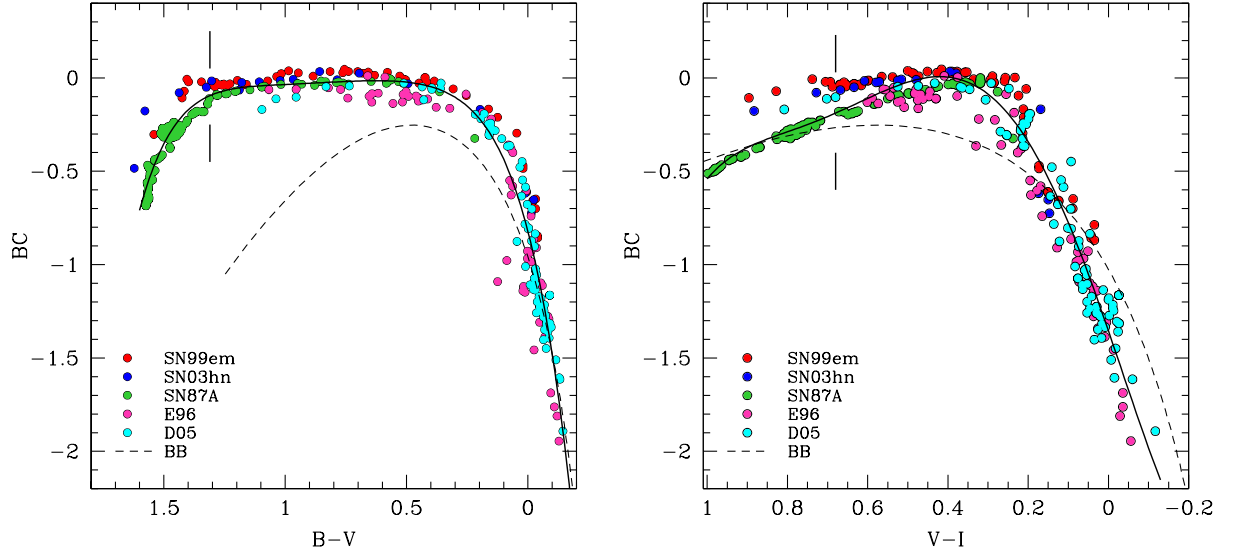


Figure 4.5: Bolometric corrections versus $(B - V)$ (**left**) and $(V - I)$ (**right**) for SN 1999em (open circles), SN 2003hn (stars), SN 1987A (filled circles) and the models of E96 (triangles) and D05 (squares). The vertical lines indicate the color at the end of the plateau phase. The solid lines show polynomial fits to the points. The dashed curves correspond to the bolometric corrections of a blackbody spectrum.

three SNe (no atmosphere models cover this phase). We do not include any of the nebular data in these diagrams, since the BB fits are not appropriate to extrapolate UV or IR fluxes at these epochs.

These plots reveal a remarkable correlation between BC and intrinsic color, both for the objects and the models. It is very satisfactory that, even though SN 1987A has a very different light curve compared with normal SNe II-P, it matches quite well the behavior of the other two SNe and the models. At very early times the BCs are quite large owing to the relatively larger flux contribution of the UV. During most of the plateau the BC remains very small around a value of zero, which implies that the V magnitude provides a very close proxy bolometric magnitude. During the transition from the plateau to the radioactive tail (redward from the vertical bar) the BC starts to depart from zero due to the larger flux contribution in the IR. At this phase SN 1987A shows some discrepancies, at the level of ~ 0.1 - 0.2 mag, with

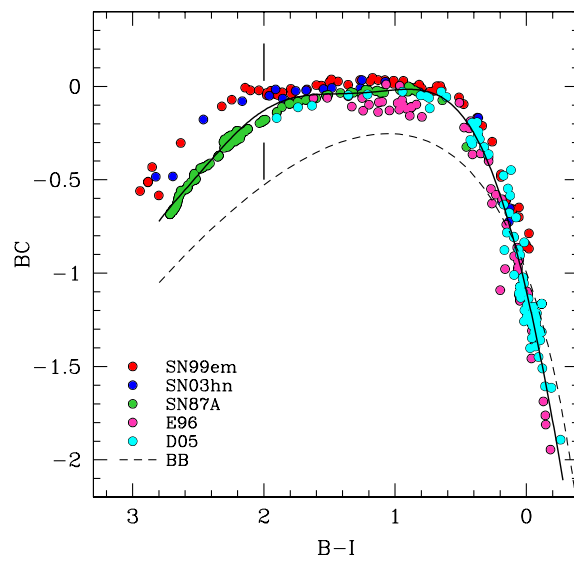


Figure 4.6: Bolometric corrections versus $(B - I)$ for SN 1999em (open circles), SN 2003hn (stars), SN 1987A (filled circles) and the models of E96 (triangles) and D05 (squares). The vertical line indicates the color at the end of the the plateau phase. The solid line shows a polynomial fit to the points. The dashed curve corresponds to the bolometric corrections of a blackbody spectrum.

respect to the other two SNe. Since the bolometric fluxes for SN 1987A comprise two more IR bands, L and M , we examine the possibility that these discrepancies could be due to this fact. For this, we exclude the L and M bands for SN 1987A and recompute the bolometric flux in the same manner as for the other two SNe, i.e, by calculating F_{IR} as the extrapolation of a BB fit to $U - K$ photometry. This exercise shows that, while the BC corrections over the plateau phase do not change in any significant way (lending support to the F_{IR} derived from BB fits), by the end of the plateau and at later times the new BCs increase and get closer to the other two SNe. The conclusion is that the differences observed during the transition are due to an inaccurate estimate of F_{IR} from the BB fits restricted to $U - K$ photometry. Adding L and M photometry at these late epochs does help and provides a more accurate estimate of F_{IR} . Therefore, during the transition we decided to exclude the BCs derived from SN 1999em and 2003hn.

A good representation of the correlation between BC and colors can be obtained with polynomial fits of the form,

$$BC(color) = \sum_{i=0}^n a_i (color)^i, \quad (4.3)$$

where the order n varies for each color. Table 4.1 lists the coefficients obtained for the fit of each color, their range of validity and the number of data points used. The fits have dispersions (rms) of 0.11 mag for $(B - V)$, 0.11 mag for $(V - I)$ and 0.09 mag for $(B - I)$ in the whole range (plateau plus transition to the radioactive tail).

The corresponding polynomials fits are also shown with solid lines in Figure 4.5 and 4.6. As a comparison, the dashed lines in these Figures show the BC derived for a blackbody. The blackbody models represent well the data at early times (bluest colors), but evidently differ from the atmosphere models and the observed SNe at later epochs.

As argued in section 4.1.1, we have good reasons to trust more the atmosphere models than the early data of SN 1999em, so we decided to exclude the latter from

Table 4.1: Coefficients of the fits to $BC(color)^a$.

a_i	$B - V$	$V - I$	$B - I$
a_0	-0.823	-1.355	-1.096
a_1	5.027	6.262	3.038
a_2	-13.409	-2.676	-2.246
a_3	20.133	-22.973	-0.497
a_4	-18.096	35.542	0.7078
a_5	9.084	-15.340	0.576
a_6	-1.950	...	-0.713
a_7	0.239
a_8	-0.027
ranges	$[-0.2, 1.65]$	$[-0.1, 1]$	$[-0.4, 3]$
No. points	512	465	512
rms [mag]	0.113	0.109	0.091

$$^a BC(color) = \sum_{i=0}^n a_i (color)^i$$

our fits. Therefore, our calibration should be considered more uncertain here. A further complication at early phases is the steep dependence of the BC on color. This means that a slight error in the measurement of the color, such as that due to a poor extinction determination, could cause a significant error in the determination of the BC. This problem is less pronounced if we use $(V - I)$ to estimate BC at these epochs. We also test if a bolometric correction with respect to the R band instead of V would improve the situation, but we do not find any improvements.

Using the coefficients given in Table 4.1, it is possible to derive a bolometric luminosity for any SN II-P using only two (or three in the case of the $(B - I)$ color) optical filters. If one knows the extinction and the distance to the object the bolometric luminosity can be computed as follows:

$$\log L[\text{erg s}^{-1}] = -0.4 [BC(color) + V - A_{total}(V) - 11.64] + \log(4\pi D^2), \quad (4.4)$$

where D is the distance in cm to the SN and $A_{total}(V)$ is the total, host plus Galactic

visual extinction. Note that combining this equation with equations (4.1) and (4.2), the luminosity becomes independent of the arbitrary zero points chosen for the Vega magnitude scale, and it only depends on the observed flux density, color, extinction and distance.

The calibrations of BC versus colors shown above are only valid during the optically thick phases since they involve BB fits to the photometry. In the nebular phase, we calculated BCs for the three SNe using the integrated flux between the observed bands (i.e. $U - K$ for SN 1999em and SN 2003hn, and $U - M$ for SN 1987A). We did not attempt to add any flux beyond these limits since we did not have any physical model to extrapolate. As shown in the left panel of Figure 4.7 the BC for SN 1987A is almost independent of color, with a value ~ -0.7 mag and a scatter of only 0.015 mag. The other two SNe yield BCs 0.2–0.3 mag higher, with a slight dependence on color. We investigate whether these differences could be due to the inclusion of the two additional bands for SN 1987A: we removed the L and M bands from the BC and, not surprisingly, the agreement proved much better (Right panel of Figure 4.7). We conclude that the L and M contributions to the bolometric flux is not negligible at the nebular phase. Hence, we take the value of -0.70 derived from SN 1987A as the best estimate of the BC at the onset of the nebular phase.

We conclude this section with the claim that we have implemented a robust method to estimate BCs for SNe II-P which allows one to derive bolometric luminosities. If we trust the late behavior of SN 1987A as being representative of SNe II-P in general, our analysis implies an overall accuracy of 0.05 dex in BCs. Clearly, it would be interesting to check this result using L and M photometric data of other SNe II-P, but such data are currently unavailable. Our calibrations have the potential to be applied to many SNe observed over a limited wavelength range.

4.1.3 Effective Temperature-Color Relation

Along with bolometric luminosity, the effective temperature is a critical parameter in the comparison of observations with hydrodynamical models. Each model spectrum

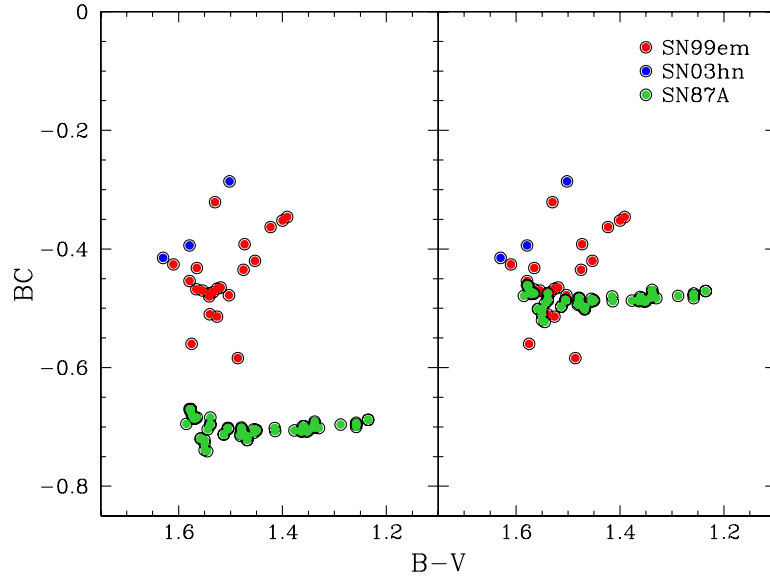


Figure 4.7: (**Left**) Bolometric corrections obtained during the radioactive tail phase versus $(B - V)$, as derived using U through M photometry for SN 1987A (filled circles), and U through K photometry for SN 1999em (open circles) and SN 2003hn (stars). (**Right**) Same as before, but excluding the L and M bands for SN 1987A.

of E96 and D05 has an associated effective temperature (T_{eff}), defined by the relation $L = 4\pi R_{ph}^2 \sigma T_{eff}^4$ where L is the input luminosity of the atmospheric models and R_{ph} , the photospheric radius, is an output of the models. I examined the dependence of T_{eff} on $(B - V)$ and $(V - I)$ colors derived via synthetic photometry from the model spectra, as described in section 4.1.1. The purpose of this analysis was to provide a calibration between temperature and color which could be used to easily derive estimates of T_{eff} from observed colors for any SN II-P. Note, however, that T_{eff} does not have a direct physical meaning for this type of object. It is simply a convenient contact point between hydrodynamical models and observations.

Figure 4.8 shows the effective temperature versus synthetic $(B - V)$ and $(V - I)$ colors for E96 and D05 models. As expected, there is a tight correlation between these quantities for each set of models. At early epochs, when $(B - V) \lesssim 0.2$ and $(V - I) \lesssim 0.3$, both models show consistent values of the effective temperature within their internal dispersion. Later on, however, when the plateau phase is well established, there are systematic differences in the behavior of both sets, with the models of D05 giving larger effective temperatures. Similar differences have been reported in the literature with regard to the dilution factors calculated from both sets of models (Dessart & Hillier, 2005b; Jones et al., 2009), but there has been no clear explanation for the discrepancies. Note that $T_{eff} (\propto \sqrt{R_{ph}})$ is an output of the atmosphere model and depends on complicated details of the solution of radiation transport through the envelope, such as non-LTE treatment of the different species and metal line opacities.

In order to represent the correlation between T_{eff} and colors shown in Figure 4.8, we fit polynomial functions of the form,

$$T_{eff}(color)[10^4 K] = \sum_{i=0}^n a_i (color)^i. \quad (4.5)$$

The fits were done for each set of models separately and they are shown in Figure 4.8 with solid lines. The coefficients of the fits, ranges of validity for $(B - V)$ and $(V - I)$ colors, and dispersions are given in Table 4.2. The fits to the E96 models are

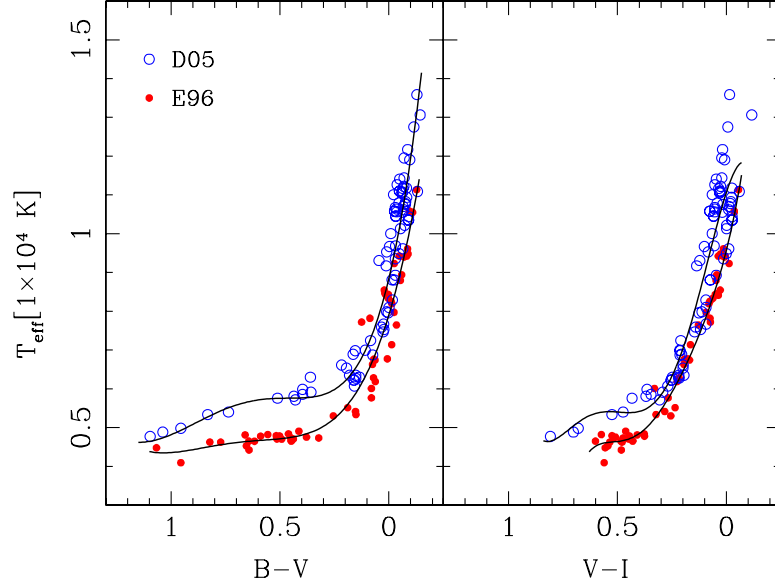


Figure 4.8: Effective temperature versus $(B-V)$ (**left**) and $(V-I)$ (**right**) from the models of E96 (filled circles) and D05 (open circles). The solid lines show polynomial fits for each set of models.

characterized by a scatter of ~ 500 K in $(B-V)$ and ~ 350 K in $(V-I)$. For the D05 models the scatter is ~ 670 K in $(B-V)$ and ~ 800 K in $(V-I)$. We do not have any strong argument to rule out either set of models. We therefore keep both results even if they show significant systematic differences. But we notice that the value of T_{eff} during the recombination phase (where it is nearly constant) appears to be somewhat underestimated ($T_{eff} \sim 4600$ K) by E96. We recall that these calibrations are only valid until the end of the plateau phase.

In Figure 4.9 we show how these calibrations work for estimating T_{eff} for SN 1987A, SN 1999em, and SN 2003hn. As a comparison we included in these plots color temperatures obtained from the BB fits described in section 4.1.1. Note that for the three SNe the color temperatures are greater than T_{eff} , which is expected for “dilute” atmospheres whose continuum opacity is dominated by electron scattering. As said above, the usefulness of these fits is that they allow one to obtain T_{eff} for any SN II-P from their $(B-V)$ or $(V-I)$ colors, and thereby use this quantity to compare with hydrodynamical models. Note that we could equivalently have chosen

Table 4.2: Coefficients of the fits to $T_{eff}(\text{color})^a$.

	$B - V$	$B - V$	$V - I$	$V - I$
a_i	<i>E96</i>	<i>D05</i>	<i>E96</i>	<i>D05</i>
a_0	0.790	0.884	0.957	1.106
a_1	-1.856	-2.340	-2.254	-1.736
a_2	4.055	6.628	5.922	-6.403
a_3	-3.922	-8.456	-18.476	33.762
a_4	1.368	4.619	36.058	-48.260
a_5	\dots	-0.849	-25.291	22.362
ranges	$[-0.2, 1.15]$	$[-0.2, 1.15]$	$[-0.1, 0.65]$	$[-0.07, 0.83]$
rms [K]	500	670	350	800

$$^a T_{eff}(\text{color})[10^4 K] = \sum_{i=0}^n a_i (\text{color})^i$$

to calibrate R_{ph} vs color.

4.2 Photospheric velocities

Another important parameter to compare with observations is the photospheric velocity yielded by our models. Expansion velocity estimates from the minimum of several spectral lines (H_α , Fe II $\lambda 5169$, H_β and H_γ) of our data set were given by Jones et al. (2009). Since each line forms at a different shells, it is not straight forward to compare the observed velocities with photospheric velocities. Jones et al. (2009) got around this problem and derived congruent calibrations between the velocity derived from the absorption minimum of such lines and the photospheric velocity using two independent atmosphere models (E96 and D05). As noted by Jones et al. (2009) H_β provides a very good proxy to the photosphere velocity as it is not highly saturated as H_α , and is present over most of the SN evolution. Therefore, in the comparisons with our models, we chose to use the calibration given by Jones et al. (2009) for this particular line. However, in spite of the satisfactory behavior of this calibration in the high-velocity regime ($v \gtrsim 5000 \text{ km s}^{-1}$), for lower velocities the atmosphere models fail to reproduce the behavior shown by the data (see Figure 9 of Jones et al., 2009). Thus, we decided to complement our comparison with velocities

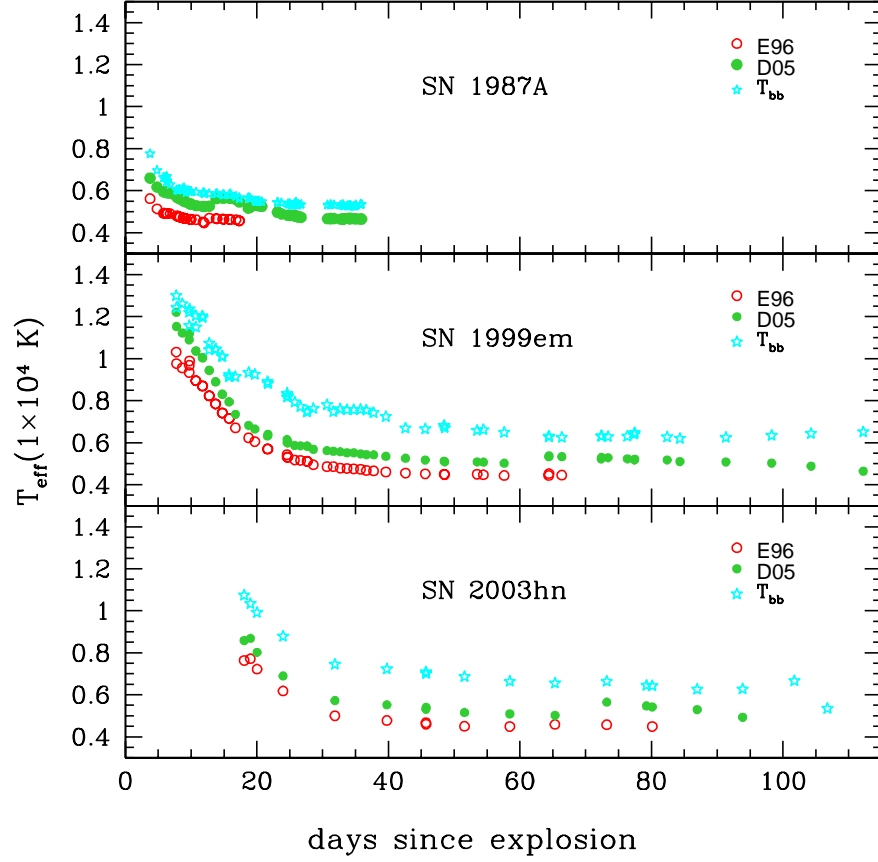


Figure 4.9: Effective temperatures for SN 1987A (**upper panel**), SN 1999em (**middle panel**) and SN 2003hn (**bottom panel**) as a function of time since explosion calculated using the polynomial fits given in table 4.2 for the models of E96 (open circles) and D05 (filled circles). As a comparison we include in these plots the color temperatures obtained from the BB fits described in section 4.1.1.

estimated from the Fe II $\lambda 5169$ line for the case where it is present at later phases of the SN evolution and therefore the velocities are below the limit imposed by the calibration of hydrogen lines.

For consistency with the atmosphere models, we define the photospheric position for our hydrodynamical models as the layer where the total continuum optical depth is $\tau = 2/3$. Note that to calculate τ we do not include the opacity floor (see discussion in section 3.1.2) because such minimum is only included to take into account line effects, and therefore is a bound-bound opacity that does not contribute to form the continuum. With this definition, the photosphere follows the recombination wave, as we show in section 5.1.3, due to the fact that electron scattering is the dominant source of opacity (see Figure 3.1). Had we included the opacity floor in the definition of τ , the $\tau = 2/3$ surface would be pushed well above the recombination front.

We remark that with this definition, the photosphere is essentially the surface of last scattering. However, the surface where the continuum is actually formed is located in a deeper layer called the “thermalization depth” and this is due to the dominance of the electron scattering over the absorption processes (Sobolev, 1980; Hoflich, 1991; Montes & Wagoner, 1995). With our simple prescription of radiative transfer we cannot accurately determine the location of the thermalization depth because there radiation decouples from matter. Note that the color temperature, determined by a black body fit to the broad-band photometry, is nearly coincident with the temperature of the thermalization depth but is greater than the effective temperature (as also shown in Figure 4.9).

Chapter 5

Hydro-Model for SN 1999em

In this Chapter, I present a detailed study of the prototype SN 1999em using the hydrodynamical code described in Chapter 3. The choice of this object was motivated by the fact that it is one of the best observed SNe of its type, both in terms of wavelength coverage and temporal sampling. In § 5.1 I present the bolometric light curve and photospheric velocities for this object resulting from model calculations. A remarkably good agreement with observations was obtained using the following physical parameters: $E = 1.25$ foe, $M = 19 M_{\odot}$, $R = 800 R_{\odot}$ and $M_{\text{Ni}} = 0.056 M_{\odot}$. In this analysis, I find that an extensive mixing of ^{56}Ni is required in order to reproduce a plateau as flat as that shown by the observations. In § 5.2 I discuss how our results compare with two previous hydrodynamical studies of SN 1999em (Baklanov et al., 2005; Utrobin, 2007). Finally, in § 5.3 I study the possibility of fitting the observations with lower values of the initial mass consistently with the upper limits that have been inferred from pre-supernova imaging of SN 1999em in connection with stellar evolution models. I cannot find a set of physical parameters that reproduce well the observations for models with pre-supernova mass of $\leq 12 M_{\odot}$, although models with $14 M_{\odot}$ cannot be fully discarded.

5.1 High-Mass Model of SN 1999em

SN 1999em was discovered shortly after explosion on 1999 October 29 UT by the LOSS program (Li, 1999). Based on EPM study by Jones et al. (2009), we assume SN 1999em exploded three days before discovery. This is consistent with the constraint imposed by a negative detection (limiting magnitude 19) on an image obtained on 1999 October 20 UT. In order to compare with our model, we correct the times elapsed since explosion by time dilation based on the redshift of the host galaxy. We adopted the Cepheid distance of 11.7 Mpc given by Leonard et al. (2003) to compute bolometric luminosities as explained in § 4.1.2 using photometric data obtained at *Cerro Tololo Inter-American Observatory* (CTIO), *Las Campanas Observatory* (LCO), and the *European Southern Observatory* (ESO) at *La Silla* (Hamuy, 2001).

We use a pre-supernova model with initial parameters consistent with the optimal hydrodynamical model of Utrobin (2007). Specifically, we adopt an initial mass of $19 M_{\odot}$, radius of $800 R_{\odot}$, and explosion energy of $E = 1.25$ foe ($1 \text{ foe} = 1 \times 10^{51}$ erg). This energy was released as thermal energy near the core of the object in a very short time scale as compared with the hydrodynamic time scale of our model. We also assume a nickel mass of $0.056 M_{\odot}$ which was determined by the luminosity of the radioactive tail. This parameter is quite different to the nickel mass of $0.036 M_{\odot}$ used by Utrobin (2007) which was determined using the quasi-bolometric luminosity given by Elmhamdi et al. (2003). Their luminosity was based on the integration of only *UBVRI* photometry with a constant value of 0.19 dex added to take into account the infrared luminosity, while our bolometric luminosity is based on a quantitative study of the bolometric correction for SNe II-P (see § 4). Note also that our value for the nickel mass is closer to the estimate of $0.06 M_{\odot}$ given by Baklanov et al. (2005). In the following analysis, we denote this model as M19R8E1.25NI56.

In our calculations we remove the central $1.4 M_{\odot}$ which is assumed to form a neutron star. The initial density profile as function of mass and radius for model M19R8E1.25NI56 is shown in Figure 5.1. Note that the initial structure is composed

of a dense core and an extended envelope characteristic of a red supergiant. The chemical composition profiles are shown in Figure 5.2. The outer parts of the envelope, $M > 9 M_{\odot}$, have a homogeneous composition with mass fractions for hydrogen of $X = 0.735$, for helium of $Y = 0.251$, and a metallicity of $Z = 0.02$. From there inward, hydrogen and helium are mixed in order to prevent a sharp boundary between the H-rich and the He-rich layers. Such sharp boundaries are characteristic of stellar evolution models but fail to reproduce the observations. Note that we allow H to mix very deep inside the core and ^{56}Ni is mixed out in the envelope up to $\sim 15 M_{\odot}$. This type of mixing is presumably due to Rayleigh-Taylor instabilities that occur behind the shock front, as obtained in multi-dimensional hydrodynamic calculations (Mueller et al., 1991; Kane et al., 2000) and supported by studies of SN 1987A (Shigeyama et al., 1988; Woosley et al., 1988; Arnett, 1988; Blinnikov et al., 2000, among others). The presence of H in the core leads to a smooth transition between the plateau and the radioactive tail. The distribution of ^{56}Ni to external layers helps to reproduce a plateau as flat as that observed in SN 1999em (see section 5.1.3).

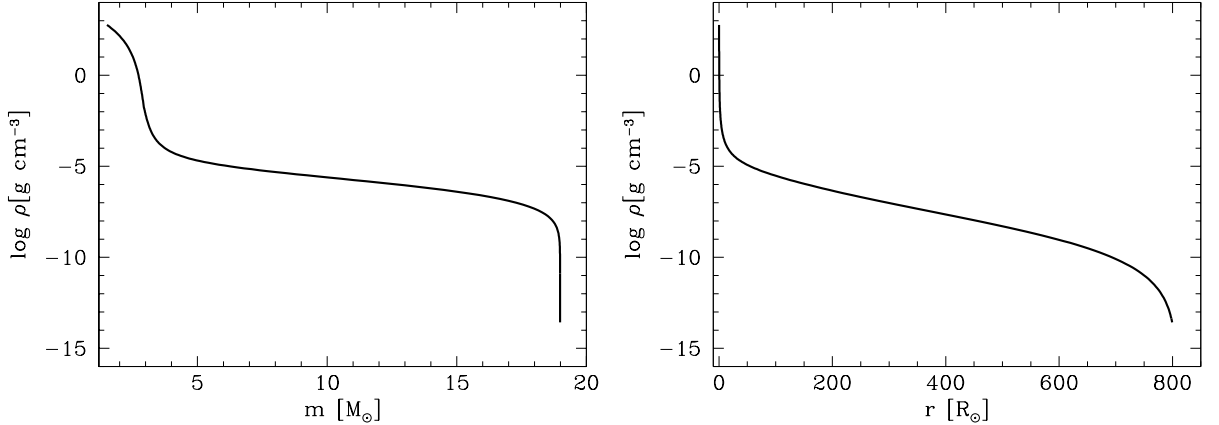


Figure 5.1: Initial density distribution with respect to interior mass (**left**) and radius (**right**) for the pre-supernova model M19R8E1.25Ni56.

Figure 5.3 shows a comparison between the bolometric light curve (solid line) obtained with our code for model M19R8E1.25Ni56, and the observations of SN 1999em (dots). The luminosity due to $^{56}\text{Ni} \rightarrow ^{56}\text{Co} \rightarrow ^{56}\text{Fe}$ (dashed line) is also shown. Note the very good agreement between model and observations. The largest difference ap-

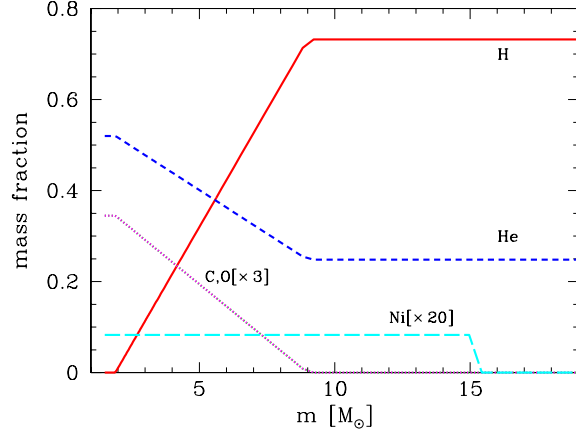


Figure 5.2: Abundance distribution in the pre-supernova model M19R8E1.25NI56 with respect to Lagrangian mass. For clarity, the abundance of carbon (C) and oxygen (O) were multiplied by 3 and the abundance of ^{56}Ni , by 20. Note that the ^{56}Ni is uniformly mixed in the outer envelope until $15 M_{\odot}$.

pears during the earliest phase and the transition to the radioactive tail. At earliest epochs our bolometric corrections have the highest uncertainties, as noted in § 4.1.2, and during the transition between the plateau and the radioactive tail, the diffusion approximation breaks down because the object is almost completely recombined and the photosphere is not well defined. During the tail, the bolometric luminosity is completely determined by the luminosity of radioactive decay, which makes our calculations more reliable. Although not shown here, our code shows that the shape of the light curve at the end of the plateau is very sensitive to the properties of the core, such as mixing and the form of the density transition between the helium-rich core and the hydrogen-rich envelope. In principle, it is possible to find an even better fit to the observations but, given the uncertainties introduced by our approximations, such a detailed study should be considered as meaningless.

Figure 5.4 shows the photospheric velocity evolution of our model compared with observed photospheric velocities as explained in § 4.2. We have also included in the plot the spectroscopic velocities measured from the absorption minimum of the Fe II $\lambda 5169$ line (Jones et al., 2009), revealing that the velocities estimated from this line samples quite well the photospheric velocity at all epochs when it is present. However, it is not present at the very earliest times ($t < 10$ days). Note the very good

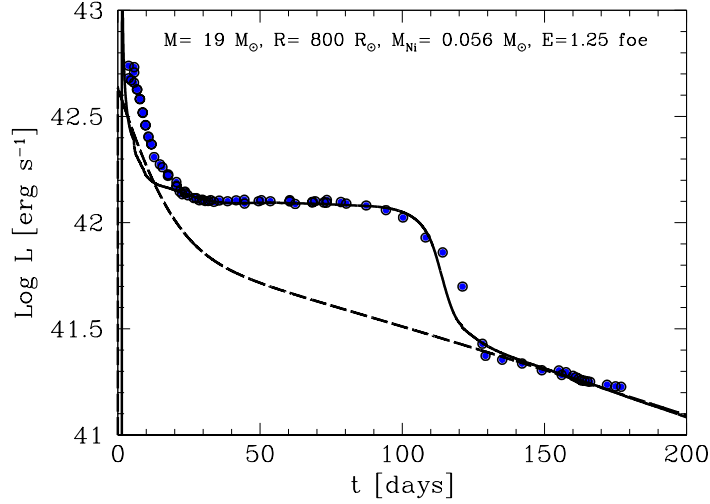


Figure 5.3: The bolometric light curve for model M19R8E1.25NI56 (solid line) compared with the data of SN 1999em as calculated by Bersten & Hamuy (2009) (blue dots). The luminosity due to the $^{56}\text{Ni} \rightarrow ^{56}\text{Co} \rightarrow ^{56}\text{Fe}$ decay is also shown (dashed line). The physical parameters used in the model are indicated.

overall agreement between model and observations. Fe II velocities match quite well the model photospheric velocities except at the latest times. However, it is important to remark that the photospheric velocity is to be considered a good discriminator between models only at the early phases of the evolution while the object is not completely recombined. This is because, line velocities become poor photospheric velocity indicators with time, and the photosphere begins to lose its meaning in our models as the ejecta becomes nearly completely recombined at the end of the plateau.

As shown in Figures 5.3 and 5.4 we obtain a remarkably good agreement with observations (bolometric light curve and photospheric velocity evolution) for SN 1999em despite the simplifications used in our code. These results are very encouraging and give us confidence in the capability of our code to infer physical parameters and to study their effect on the observed quantities with the ultimate aim of understanding the physics of SNe II-P.

In the following subsections, we describe in some detail the evolution of the

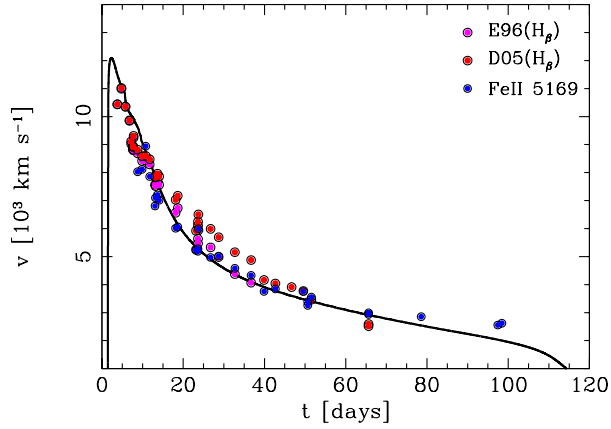


Figure 5.4: Evolution of the expansion velocity of the photosphere for model M19R8E1.25NI56 (solid line) compared with observed photospheric velocities calculated by Jones et al. (2009) using a calibration between the velocity derived from the absorption minimum of H_β and two atmosphere models: E96 (filled squares) and D05 (open circles). We also include the velocities calculated from Fe II $\lambda 5169$ (filled circles).

SN for this particular model. At a glance, the LC is distinguished by three phases: a) an outburst followed by strong cooling, b) a plateau, and c) a radioactive tail. Each phase is essentially determined by the interplay between the main heating and cooling mechanisms. We thus focus our discussion on these processes along the SN evolution. As a reference, Table 5.1 gives a summary of some properties of the model at characteristic times during the evolution. The initial phase due to shock breakout is discussed in § 5.1.1, the adiabatic-cooling phase where the homologous expansion is reached is addressed in § 5.1.2, the cooling and recombination phase is described in § 5.1.3, and finally the radioactive-decay processes that power the tail are explained in § 5.1.3.

5.1.1 Shock wave propagation and the early evolution

A powerful shock wave (SW) begins to propagate outward through the envelope when we artificially inject energy near the center of the star (assumed to occur

Table 5.1: Properties of model M19R8E1.25NI56 at selected time of their evolution.

Phase	t [days]	$\log(L_{bol})$ [erg s ⁻¹]	$\log(T_{eff})$ [K]	$\log(T_{ph})$ [K]	R_{ph} [10 ¹⁴ cm]	v_{ph} [10 ⁸ cm s ⁻¹]	E_{rad}/E_0^a (%)	E_K/E_0^a (%)
Peak	1.5	44.5	5.05	5.03	0.54	3.36	0.04	72
Adiabatic Cooling	5	42.4	4.10	4.05	3.8	11.5	0.2	93
Plateau	50	42.1	3.73	3.77	14.7	3.47	0.65	99
Transition	114	41.7	3.74	3.74	10	1	1.2	99.7

^a E_{rad} is defined by $\int_0^t L_{bol} dt$ and E_K is the total kinetic energy in the mass motions. In the table we show these quantities normalized to the initial injected energy of model M19R8E1.25NI56, $E_0 = 1.25$ foe.

at $t = 0$). This energy is initially released as internal energy, and part of it is rapidly transformed into kinetic energy (e.g., by $t = 0.5$ days, the total energy is approximately equally divided between kinetic and internal energy). The velocities acquired by matter are so high that they exceed the local speed of sound, leading to the formation of a SW. The SW heats and accelerates the matter depositing mechanical and thermal energy into successive layers of the envelope until it reaching the surface, where photon diffusion dominates the energy transfer, and energy begins to be radiated away.

Figure 5.5 shows the effect of the SW propagation on different physical quantities (velocity, density and temperature) inside the star. The shock front is evidenced as a sudden change in these quantities. As the shock moves outward, the material behind is accelerated and heated. Note that the outermost layers, with a sharp decline in density, acquires very high velocities. It represents a small fraction of the star. It is also clear from the velocity profiles that the inner parts of the object are decelerated. This deceleration is due to the interaction of the dense core with the extended hydrogen-rich envelope. The bottom right figure shows changes in radius for different shells. From this we can deduce the location of the shock front at any time as that of the innermost shell which has constant radius.

At $t = 1.36$ days, the SW reaches the surface of the object, which produces the first electromagnetic manifestation of the explosion (although neutrinos and gravitational waves escape well before). The effective temperature and bolometric luminosity suddenly rise and reach their maximum values a few hours after breakout, specifically, at $t = 1.47$ days with values of $L_{peak} = 3 \times 10^{44}$ erg s⁻¹ and $T_{peak} = 1.1 \times 10^5$ K

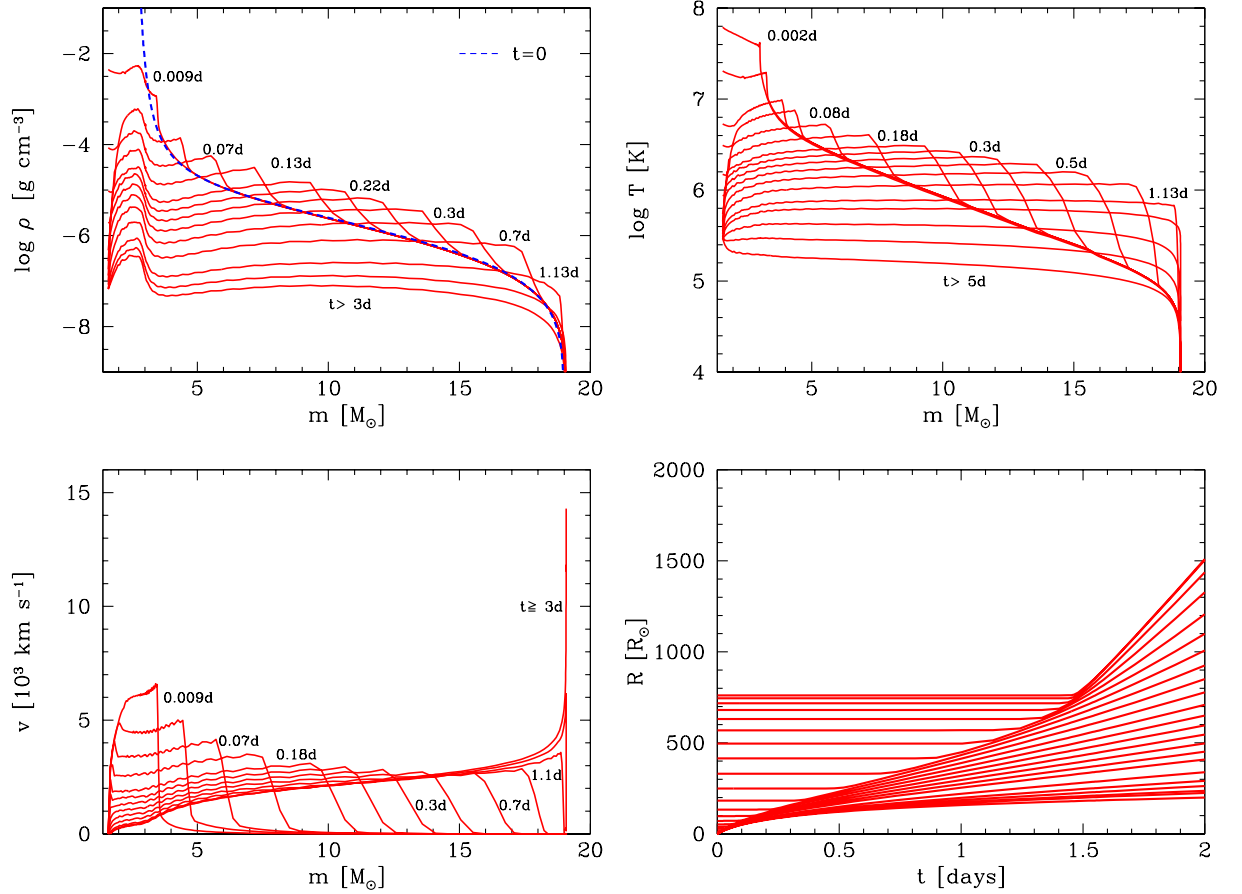


Figure 5.5: Changes in density (**top left**), temperature (**top right**), and velocity (**bottom left**) profiles as a function of interior mass during shock propagation for model M19R8E1.25NI56. Some of the curves are labeled with the time elapsed since the energy is injected. The initial density profile is also shown ($t = 0$; blue dashed line). Note that a very small amount of material near the surface is strongly accelerated as the SW passes through the steep density gradients present in the outermost layers. **Bottom right:** temporal evolution of the radial coordinates corresponding to different interior layers.

as shown in Figure 5.6. At these temperatures, the peak of the emitted spectrum is in the UV range.

Hereafter, the star begins to expand and cool very quickly, leading to an increase in photospheric radius and a decrease in temperature in the external layers. The bolometric luminosity abruptly decreases but, according to the decrease in effective temperature and consequent shift of the emission peak to longer wavelengths, the luminosity in the optical range increases. As a result, a sharp peak in bolometric luminosity and temperature is produced, as shown in Figure 5.6. In our model we obtain a decrease of 1.5 dex in luminosity only 6.8 hours after peak brightness. During this time the total energy radiated is 2.2×10^{48} erg, emitted essentially as a UV flash. The short duration of the breakout explains why so few SNe II-P have been observed during this phase.

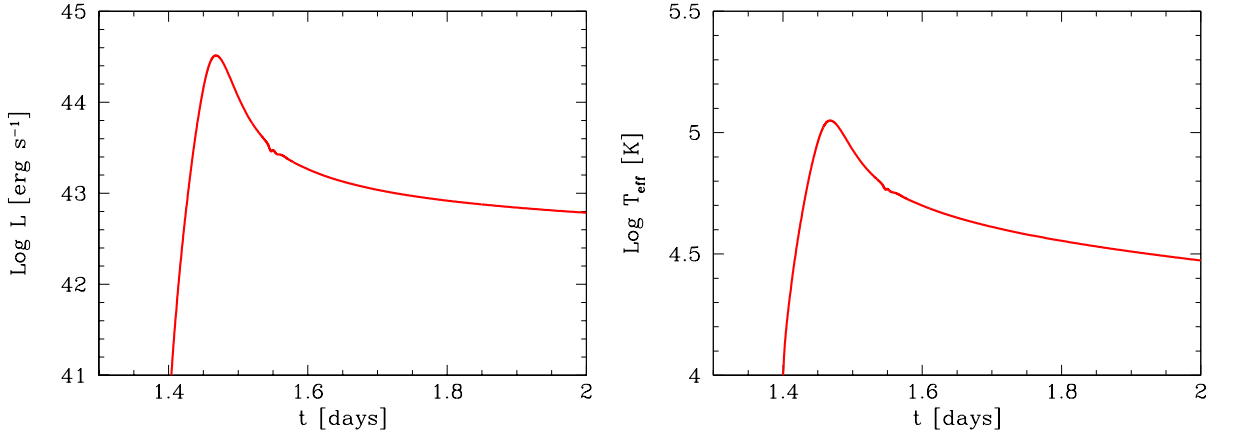


Figure 5.6: Bolometric luminosity (**left**) and effective temperature (**right**) during shock breakout

At temperatures as high as those left by the passage of the shock wave, the stellar matter is completely ionized which implies that the breakout is accompanied by a strong increase in opacity. The position of the photosphere during the outburst nearly coincides with the outermost shell. This behavior continues until the onset of recombination. Therefore, at early stages previous to recombination, the velocity of matter in the photospheric position samples the very high velocities of the outermost layers and reaches values close to $1.2 \times 10^4 \text{ km s}^{-1}$.

From the energetics point of view, by $t = 0.5$ day the total energy is approximately divided in equal proportions between internal, dominated by radiative contribution, and kinetic components. Short after breakout the kinetic energy completely dominates the energetics (the energy radiated away at any given time is less than 1.5% of the total energy).

It is possible to estimate the average velocity during the SW propagation: given that the SW takes 1.36 days to emerge and considering a radius of $R = 5.5 \times 10^{13}$ cm ($800 R_{\odot}$), we obtain an average speed of $v = 4680$ km s $^{-1}$. It is also interesting to calculate the expected time for breakout using the analytic expression given by Shigeyama et al. (1987),

$$t_{\text{bk}} \simeq 1.6 \left(\frac{R_0}{50 R_{\odot}} \right) \times \left[\left(\frac{M_{\text{ej}}}{10 M_{\odot}} \right) / \left(\frac{E}{1 \times 10^{51} \text{ erg}} \right) \right]^{1/2} \text{ hr}, \quad (5.1)$$

where R_0 is the initial radius, M_{ej} is the ejected mass, and E is the explosion energy. Using the values for our initial model we obtain $t_{\text{bk}} = 1.26$ days, in very good agreement with our numerical calculation.

5.1.2 Adiabatic cooling and homologous expansion

The breakout is followed by a violent expansion, resulting in the cooling of the outermost layers. During expansion, only a small fraction of the photon energy can diffuse into the surroundings. Therefore, it is possible to consider the cooling process to be approximately adiabatic and this approximation remains valid while the time-scale for radiation diffusion is much longer than the expansion time-scale¹. Note that there are two mechanisms to cool a SN: (a) loss of photons or diffusion cooling, and (b) its own expansion or “adiabatic cooling”. If one of these processes dominates then we say that the cooling is carried out by such process. In our model, more than

¹The expansion time-scale, $\tau_{\text{h}} = R/v$, increases with time while the diffusion time-scale, $\tau_{\text{d}} = \kappa \rho R^2 / c$, decreases because $\rho \propto R^{-3}$. Thus, there is a time after which the condition for this approximation breaks down.

90% of the decrease in internal energy happens as adiabatic cooling during the first 18 days after explosion, when the first layers with neutral hydrogen appear. After that, diffusion cooling begins to be significant and the adiabatic cooling phase comes to an end.

The internal temperature (and internal energy) decreases almost adiabatically, i.e. proportional to r^{-1} due to the dominance of the radiative term, and quickly reaches a value near the recombination temperature of hydrogen. Quantitatively, the effective temperature goes from values close to 10^5 K at the time of the burst when the matter is totally ionized, to $T_{\text{eff}} = 10^4$ K five days later. At these temperatures hydrogen begins to recombine. At the same time, the luminosity reaches $L = 1.9 \times 10^{42}$ erg s $^{-1}$ and the photospheric radius rapidly increases to $R_{\text{ph}} = 5.2 \times 10^{14}$ cm. After that, the luminosity decreases slightly as a result of the slower decrease in temperature and continuous increase in radius. By day 18, when the first layers of neutral hydrogen appear, we have $T_{\text{eff}} = 6960$ K, $L = 1.2 \times 10^{42}$ erg s $^{-1}$, and $R_{\text{ph}} = 9.1 \times 10^{14}$ cm. Note the slight change in luminosity, of only 0.14 dex, between day 7 and 18 (Figure 5.3).

A few days after breakout, the acceleration of the material comes to an end and the expansion becomes homologous. The matter reaches velocities of the order of 1.2×10^4 km s $^{-1}$ in the outermost layers and the object enters a state of free expansion where forces of pressure and gravitation do not have any dynamical effect on the system. The homologous regime is characterized by a constant velocity in each layer, a linear growth of the radial coordinate with time ($r \propto t$) and a density distribution decreasing with time as $\rho \propto t^{-3}$. This behavior is clearly shown in Figure 5.5 for $t > 3$ days and in Figure 5.7. The nearly constant shape of the density and temperature profiles at late times are a result of the expansion being approximately homologous. This is also evident in the linear behavior of the radial coordinates for different mass shells. The condition of constant velocity is very nearly satisfied for each shell, although the transition between acceleration and homologous expansion happens at slightly different times for different mass shells (see Figure 5.7)².

²After day 8, the photosphere remains located in shells where homology has been reached. Therefore, our models show that the expanding photosphere method (EPM) which is used to estimate distances assuming homologous expansion, can be safely applied at epochs later than this.

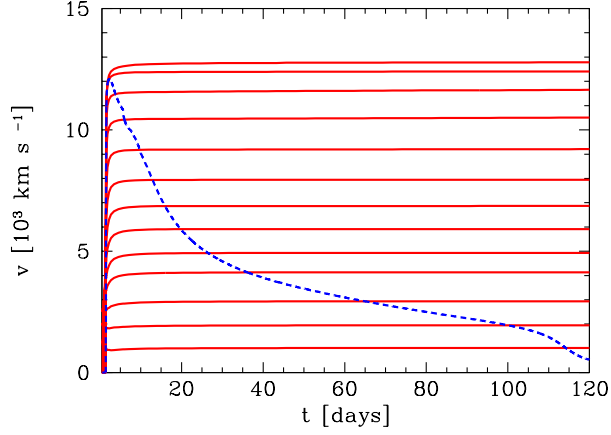


Figure 5.7: Evolution of the velocity for different layers (solid lines) and the velocity of material at the photospheric position (dashed line). Note that the asymptotic constant velocity is reached at latter times for the more external shells.

As mentioned in § 5.1.1, at the time of breakout the internal energy of the envelope is small compared to the kinetic energy. Moreover, the object expands by a factor of ~ 17 during this phase to a radius of $R_{\text{ph}} \sim 9 \times 10^{14}$ cm, before it becomes transparent. Thus, most of the internal energy left by the passage of the shock has been already degraded by the adiabatic expansion, and only a small residual will be released as observable radiation in the following phase.

5.1.3 Cooling and recombination wave

The appearance of regions with neutral hydrogen determines the onset of a recombination wave (RW). The duration of the RW is related to the total hydrogen mass and how deep hydrogen has been mixed into to the progenitor object. As time goes on, hydrogen recombination occurs at different layers of the object as a wave propagates inwards (in Lagrangian coordinate; see Figure 5.8, top). Because the opacity is dominated by electron scattering, it decreases abruptly outwards at the recombination front (Figure 5.8, top right), increasing the transparency of these layers and allowing the radiation to easily go away. Consequently, the internal energy (mostly of the radiation field) is efficiently radiated away, and the temperature drops sharply from

~ 10000 K to ~ 5500 K at the recombination front (Figure 5.8, bottom). In other words, a cooling wave associated with the transparency and induced by a recombination wave propagates inward through the envelope. This is usually called “cooling and recombination wave” (CRW).

In our model the recombination begins approximately at day 18. From then on, a CRW develops which moves inward in mass until all the matter is completely recombined by day 130 when the recombination front reaches the innermost H-rich layers of the envelope (at $m = 2 M_{\odot}$ in our model), and the luminosity suddenly drops, defining the end of this phase. The propagation of the CRW is clear in Figure 5.8 where the evolution of the fraction of ionized hydrogen and temperature profiles as a function of mass for selected times are shown. Note also the behavior of the opacity (see Figure 5.8, top right) which depends strongly on the ionization state of the matter. In our model, a strong drop in the opacity of the outer layers is seen at day ~ 18 , which leads to a considerable decrease in the optical depth of these layers and causes an inward drift in mass of the photosphere — defined at a fixed optical depth of $\tau = 2/3$. The photosphere begins to follow the CRW, as shown in Figure 5.8. It is important to note that we define the position of the photosphere using only continuum opacity sources, i.e. excluding the opacity floor (see section 4.2).

The photosphere, as defined here, is nearly coincident with the outer edge of the CRW. Therefore it is just the location of the photosphere with respect to the CRW what sets the value of the photospheric temperature close to the temperature of hydrogen recombination ($T \sim 5500$ K). However, note that the effective temperature does not necessarily have a constant value. Since the effective temperature is defined as $T_{\text{eff}}^4 = L/\pi\sigma R_{\text{ph}}^2$ and the luminosity remains nearly constant outside the recombination front (see Figure 5.10), any changes in effective temperature are related to changes in photospheric radius.

The CRW divides the object in two distinct regions: (a) an inner zone which is hot, optically thick and ionized, and (b) an outer zone which is relatively cold, optically thin and completely recombined. Matter in the inner zone is opaque: radiative transfer is too inefficient to produce any appreciable flow of radiative energy (this would be strictly fulfilled if ^{56}Ni were confined to the innermost layers; see the dis-

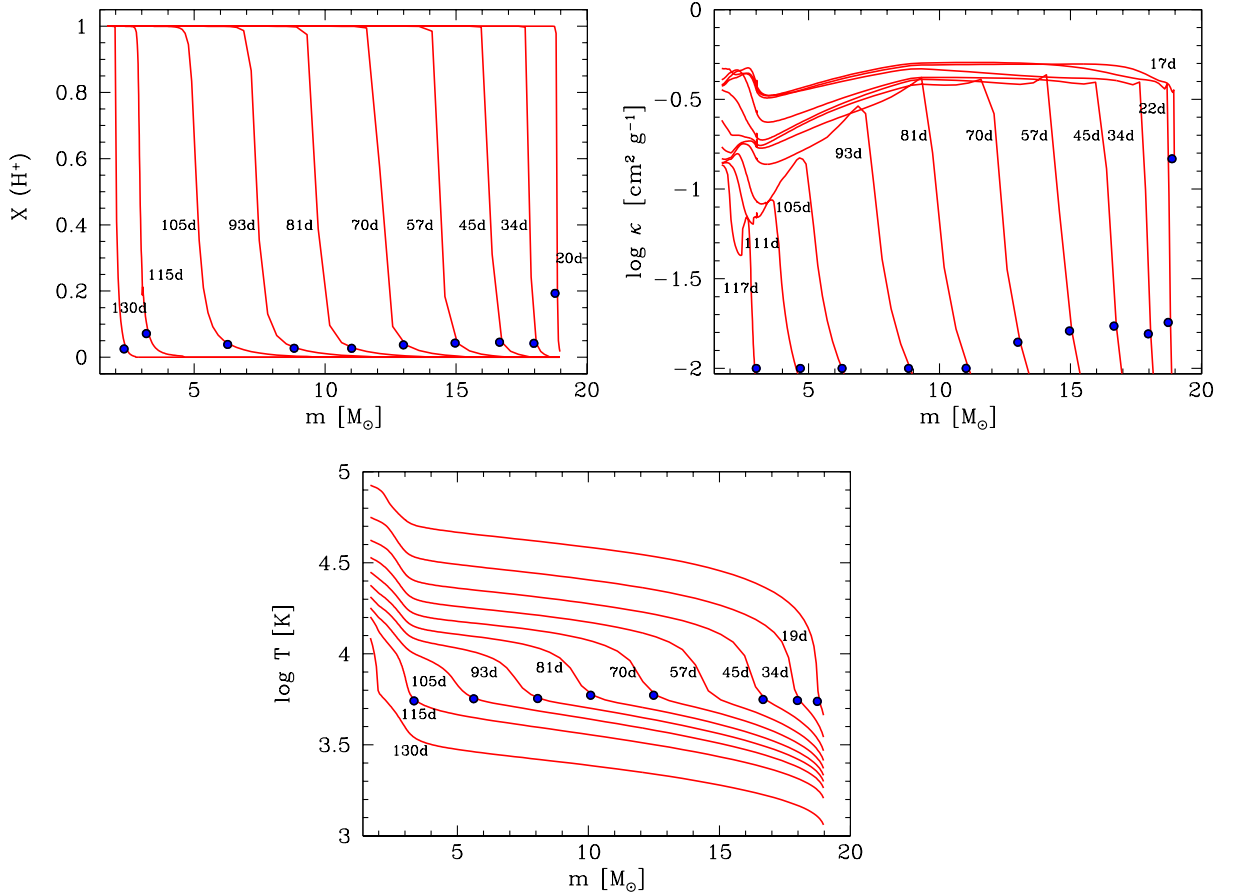


Figure 5.8: Evolution of the fraction of ionized hydrogen (**top left**), opacity (**top right**), and temperature (**bottom left**) as a function of mass. The time elapsed since the energy is injected and the photospheric position (blue dot) are indicated for each curve. The photosphere is nearly coincident with the outer edge of the CRW which moves inward in mass coordinate. Note also that the opacity in the outer shells is nearly constant with a value of $0.4 \text{ cm}^2 \text{ g}^{-1}$, close to the electron-scattering opacity for matter composed of pure hydrogen, above which it suddenly drops.

cussion below) and the matter cools down almost adiabatically. On the other hand, the external layers are transparent and practically do not radiate. Therefore, it is within the CRW interphase where almost the entire radiant flux is released. When matter passes through the CRW, particles begin to be cooled by radiation, emitting more light than they absorb, and the radiant flux increases. This way, the radiative flux emerging from the CRW front carries away internal energy of the matter that is cooled by the wave. More details on the properties of the CRW are given by Grassberg et al. (1971).

Note that the bulk of the radiation does not diffuse to the photosphere; the photosphere instead moves inward, allowing the radiation to escape sooner than it would for a photosphere fixed at the outer boundary of the ejected mass. That is, the recombination process is responsible for the energy release during this phase. **It should be noted that most of this energy comes from the energy deposited by the SW and not from the recombination itself.** In order to test the previous statement, we ran our code without including the energy released by recombination of ions with electrons. The result was that no appreciable change appeared; quantitatively, the differences between both calculations are less than 0.04 dex during all the evolution (see Figure 5.9).

Note, however, that in model M19R8E1.25Ni56 where we assumed an extended ^{56}Ni mixing, the flux of energy inside the CRW is not negligible (see left panel of Figure 5.10). This is due to the fact that the photosphere meets regions with radioactive material earlier than in the case where ^{56}Ni is confined to the innermost layers. Therefore, the energy deposited by radioactive decay provides additional power to the LC. A different behavior is seen when ^{56}Ni is confined to the innermost layers (inside $2.5 M_{\odot}$; see right panel of Figure 5.10). In this case, the statement that the energy flux inside the CRW is very small is fulfilled at least until day ~ 120 when the radiative diffusion of the radioactive decay from the central layers begins to dominate. At earlier times, it is possible to see the outward diffusion of radioactive energy. Note also that for both models the luminosity outside the front is nearly constant.

The assumption of extended mixing was necessary in order to obtain a plateau

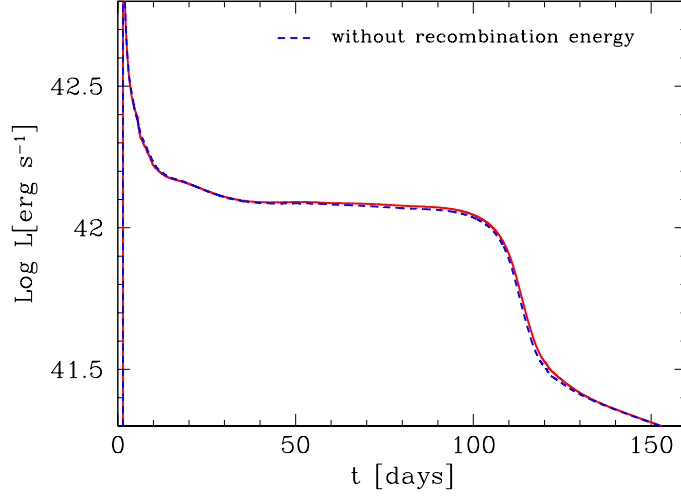


Figure 5.9: Comparison between bolometric light curves with (solid line) and without (dashed line) energy released by recombination. It is clear that the recombination of ions with electrons does not contribute significantly to the light curve. The differences between both calculations are less than 0.04 dex during whole the evolution.

as flat as the one observed for SN 1999em. Figure 5.11 shows a comparison of the bolometric LC for three cases: 1) with extended ^{56}Ni mixing, 2) no mixing, and 3) without ^{56}Ni . For case 1), ^{56}Ni begins to affect the LC by day ~ 35 while for case 2) the effect of nickel heating is delayed until day ~ 75 . On the other hand, in the former case there is a less direct energy deposition at the center of the object, and the plateau declines earlier and steeper to the tail than in case 2). Our assumption of mixing of ^{56}Ni into the hydrogen envelope is not unreasonable as shown in studies of SN 1987A (Shigeyama et al., 1988; Woosley et al., 1988; Arnett, 1988; Blinnikov et al., 2000, among others). This type of mixing is presumably due to Rayleigh-Taylor instabilities that occur behind the shock front, as obtained in multi-dimensional hydrodynamic calculations (Mueller et al., 1991; Kane et al., 2000). However, it is important to note that Utrobin (2007) found an excellent agreement with observations of SN 1999em by confining ^{56}Ni to the innermost layers and good agreement with observations of SN 1987A assuming moderate ^{56}Ni mixing (Utrobin, 1993, 2004).

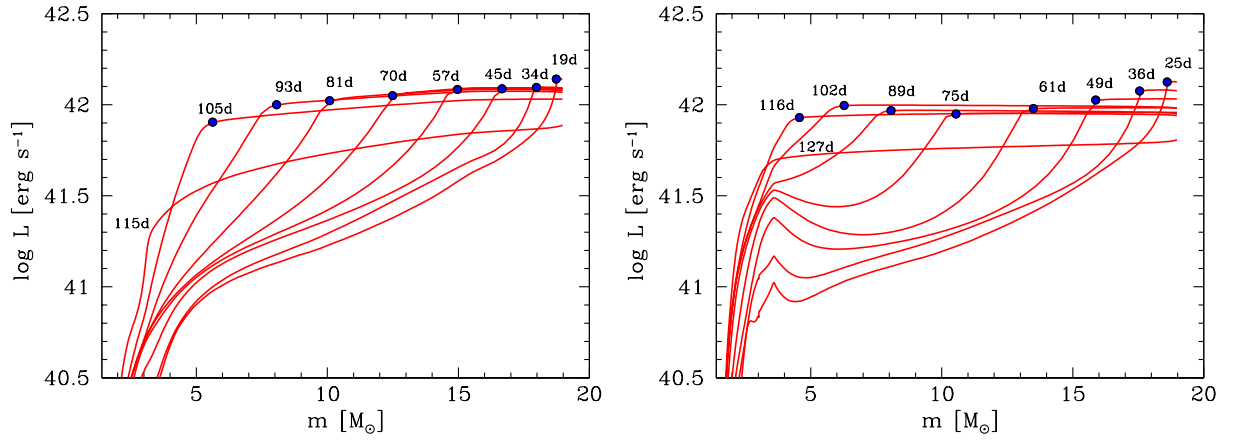


Figure 5.10: Evolution of the interior luminosity as a function of mass. The labels indicate the time since explosion. **Left:** ^{56}Ni is mixed into the hydrogen-rich envelope up to $15 M_{\odot}$. **Right:** ^{56}Ni is confined to the layers inside $3.5 M_{\odot}$. The inward propagation of the recombination front is clear in both cases. In the mixed case, the recombination front propagates slower than in the unmixed one because the temperature near the front is higher due to radioactive heating. Note that for the unmixed case the outward diffusion of the radioactive energy is clear while for the mixed case this effect occurs too early to be noticeable.

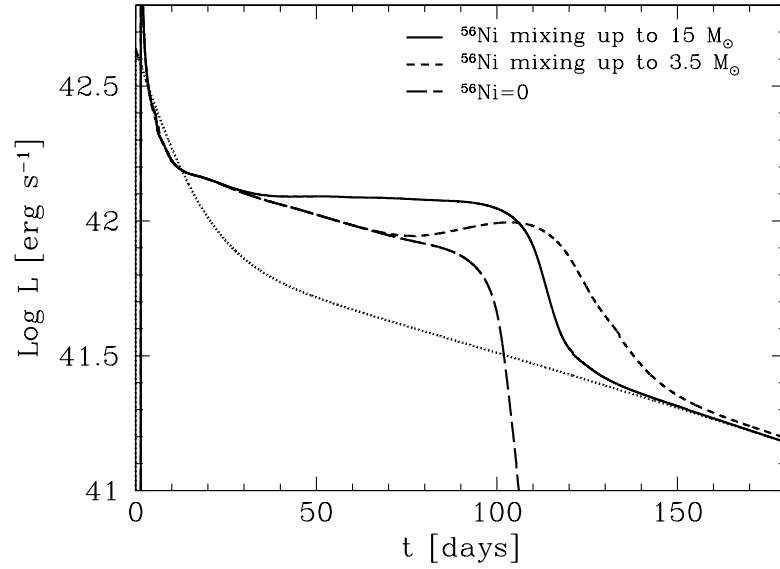


Figure 5.11: Comparison between bolometric light curves for extended ^{56}Ni mixing (solid line) and a model with mixing of ^{56}Ni up to $3.5 M_{\odot}$ (short-dashed line). We also include the case of a model without ^{56}Ni (long-dashed line) in which case the LC falls abruptly after the plateau phase. The presence of ^{56}Ni extends the plateau and increases the luminosity. This is essentially produced when the CRW reaches layers with ^{56}Ni which can thereby power the LC directly. The extended ^{56}Ni mixing reveals this effect earlier in the evolution, which produces a flat plateau in concordance with the observations of SN 1999em.

The evolution of the velocity of matter at the photospheric position v_{ph} , photospheric radius (R_{ph}) and mass above the photosphere (M_{ph}) are shown in Figure 5.12. Initially, the photospheric velocity evolves rapidly, the photospheric position follows a linear behavior, and there is very little mass above the photosphere. Later on, when the recombination sets in at $t \sim 18$ day, R_{ph} begins to differ noticeably from the linear behavior, the mass above the photosphere increases, and v_{ph} decreases because it samples increasingly inner, slower material. Finally, when all the matter is recombined at $t \sim 110$ days, R_{ph} and v_{ph} sharply turn down and the luminosity undergoes a rapid decrease. Note, however, that the photospheric radius does not drop immediately to zero. This is due to the heating caused by radioactive decay which produces some ionization of the gas. On the other hand, the luminosity undergoes a rapid decrease to values close to the luminosity of radioactive decays. If there was no ^{56}Ni (case 3) the SN luminosity would abruptly vanish at this point, as shown with a long-dashed line in Figure 5.11.

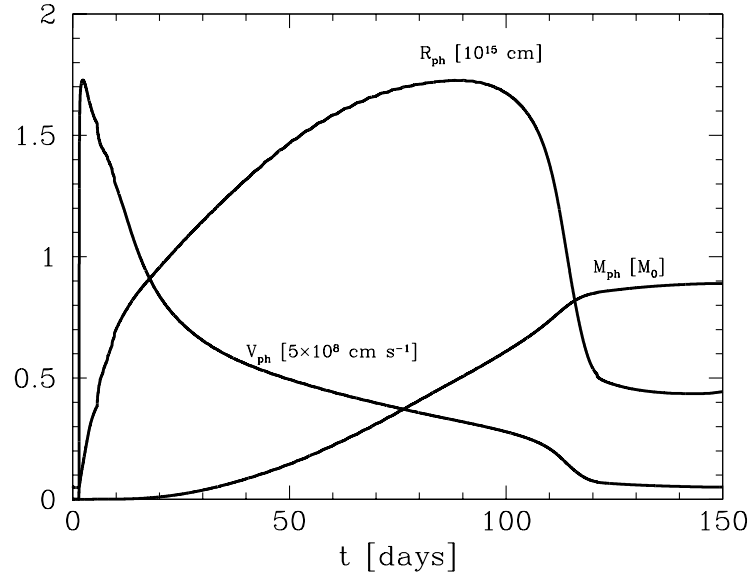


Figure 5.12: Evolution of photospheric radius (R_{ph}) in units of 10^{15} cm, photospheric velocity (V_{ph}) in units of 5×10^8 cm s $^{-1}$, and mass above the photosphere (M_{ph}) in units of M_0 ($M_0 = 19 M_{\odot}$) for model M19R8E1.25NI56.

In conclusion, the CRW has a duration of ~ 100 days. The luminosity experiences small changes during the CRW propagation. In order to produce a plateau as

flat as that observed in SN 1999em, we need to invoke significant Ni mixing in the H-rich envelope. **Thus, the plateau can be seen as a combination of CRW properties plus some additional energy provided by radioactivity.** Defining, from an empirical point of view, the plateau phase as the period of time when the luminosity remains constant within 0.5 mag of the value at day 50, its duration is 103.5 days, and the total energy emitted during this phase is $\sim 1.12 \times 10^{49}$ erg. Note, that with such definition the plateau phase includes the final stages of the early adiabatic cooling phase and not only the recombination phase.

Radioactive tail

The late behavior of the LC (at $t > 130$ days) is dominated by the energy released from radioactive decay. Without radioactive material, the luminosity would abruptly vanish when hydrogen gets completely recombined as shown in Figure 5.11. Instead, the observed LC decreases to values close to the instantaneous rate of energy deposition by the radioactive decay,

$$L \sim 1.43 \times 10^{43} M_{\text{Ni}}/M_{\odot} \exp(-t/111.3). \quad (5.2)$$

The decline of the LC at $t > 130$ days is nearly linear in concordance to the exponential decline of the radioactive decay law. That is, the diffusion time for optical photons becomes so small that the decay energy is radiated away nearly instantaneously, while the gamma-ray optical depth is still sufficiently large in order to allow a nearly complete local deposition of the decay energy. The bolometric luminosity in this part of the LC is a direct measure of the Ni mass synthesized in the explosion.

5.2 Comparison with other hydro-models of SN 1999em

In this Section, we compare our results with those of previous hydrodynamical studies of SN 1999em. There are two previous such studies of SN 1999em: one by Baklanov et al. (2005) (BBP05 hereafter) and another by Utrobin (2007) (U07 hereafter). In Table 5.2, we summarize the physical parameters obtained for SN 1999em in the three works along with the distance, explosion time, and the chemical composition assumed in each model. It is interesting to note that the three studies employ initial density distributions and chemical composition distributions of non-evolutionary models. In our work we assume H and He profiles very close to those adopted by U07, yet a very different ^{56}Ni distribution. While we assume an extended, uniform mixing of Ni (see Figure 5.2), U07 confined ^{56}Ni to the innermost layers (see their Figure 2). In the case of BBP05, H and He were assumed to be uniformly mixed throughout the envelope and a radial distribution of ^{56}Ni up to $\sim 15 M_{\odot}$ was adopted (see their Figure 9). Therefore, our ^{56}Ni distribution and the resulting ^{56}Ni mass are closer with those of BBP05 than those of U07. We also note that the mass of the compact remnant — which is left aside from the calculations — is different in all three works. We assume a compact remnant of $1.4 M_{\odot}$ while U07 assumed $1.58 M_{\odot}$ and BBP05 removed everything within a radius of $R_C = 0.1 R_{\odot}$.

Table 5.2: Comparison between physical parameters for SN 1999em from three different hydrodynamical codes

Code	D [Mpc]	t_0 [JD-2451000]	X_{sup}	Z	E [foe]	M [M_{\odot}]	R [R_{\odot}]	M_{Ni} [M_{\odot}]	Ni mixing [M_{\odot}]
This work	11.7	477.90	0.735	0.02	1.25	19	800	0.056	~ 15
BBP05 ^a	12	468.90	0.7	0.004	1	18	1000	0.06	~ 15
U07 ^b	11.7	476.90	0.735	0.017	1.3 ± 0.1	20.58 ± 1.2	500 ± 200	0.036 ± 0.009	~ 2.5

^a Baklanov et al. (2005)

^b Utrobin (2007)

The approaches used in each work are very different. U07 used a hydrodynamical code with a one-group approximation for the radiative transport, including non-LTE treatment on opacities and thermal emissivity, non thermal ionization,

and expansion opacity. Their calculations, although involving a more sophisticated radiative transfer treatment, yielded bolometric light curves comparable to those given by our code. However, the procedure to produce the observed bolometric light curve for SN 1999em was quite different in both cases. While U07 based their calculations on the integration of *UBVRI* photometry with a constant value of 0.19 dex added to take into account the infrared luminosity, we derived *UBVRIJKLM* bolometric luminosities from color-dependent bolometric corrections. As noted by Bersten & Hamuy (2009), the inclusion of the *L* and *M* bands in the calculation of the bolometric correction during the tail phase is very important and it most likely leads to the difference in the nickel mass estimated in this work and in U07. BBP05, in turn, used a multi-group hydrodynamical code which allows to calculate LC in different photometric bands. This code also included the expansion opacity effect. Therefore, BBP05 were able to compare their model with *UBVRI* LC separately without being affected by the uncertainties in the calculation of bolometric luminosities.

Table 5.2 As shown Table 5.2 in the parameters yielded by our calculations are intermediate between those estimated by BBP05 and U07. The largest differences are $2.6 M_{\odot}$ in mass, $500 R_{\odot}$ in radius, 0.3 foe in energy, and $0.045 M_{\odot}$ in ^{56}Ni mass. It is quite satisfactory that our simple prescription for the radiative transfer yields physical parameters similar to those obtained from more sophisticated codes, considering that (a) the models and methods used in each study are quite different, (b) there are differences in assumed quantities, such as distance, explosion time, mass cut, photometry, and (c) there may be a degree of degeneracy among explosion energy, initial radius and initial mass within each model.

5.3 Low Mass Model of SN 1999em

The mass of the progenitors of SNe II-P can be derived from hydrodynamical modeling of light curves and expansion velocities, or from the detection of the pre-supernova object in archival images of the host galaxy in connection with stellar evolution models. At the moment three progenitor stars of SNe II-P have been firmly detected and

there have been negative detections for 17 other objects which have led to upper limits of the progenitor star masses (Smartt et al., 2009). Among these, only three SNe II-P have masses derived using hydrodynamical models: SN 1999em, SN 2004et, and SN 2005cs. In all of these cases the masses estimated from the hydrodynamical modeling are systematically higher than the values derived from the other method. These discrepancies have been noted previously in the literature (Utrobin & Chugai, 2008; Smartt, 2009). For the particular case of SN 1999em, the pre-supernova images give an upper limit of $15 M_{\odot}$ for the progenitor star in the ZAMS. It is expected that the mass of the pre-supernova object should be lower than this due to possible mass loss episodes during the evolution of the star. In this Section we use our hydrodynamical model to explore a low mass range, consistent with pre-supernova imaging of SN 1999em, in order to test how well we can reproduce the observed properties of this object.

We calculate several models using two different values of the pre-supernova mass: $M = 12 M_{\odot}$ (see Figures 5.13 and 5.14), and $M = 14 M_{\odot}$ (see Figures 5.15 and 5.16). In all Figures, we show the bolometric light curves and photospheric velocities (v_{ph}) for different values of the injected energy (E), initial radius (R), and degree of ^{56}Ni mixing. Table 5.3 gives a summary of the parameters used. We remark that in all of these models, we have assumed the same value for the ^{56}Ni mass as that of model M19R8E1.25NI56, i.e. $0.056 M_{\odot}$, because this value is required to fit the tail of the LC. Also note that the degree of ^{56}Ni mixing is taken as a fraction of the initial mass of the object in order to compare the different degrees of mixing in a consistent way when models with different initial mass are used. For example, a model with a mixing of ^{56}Ni up to $0.8 M_0$ has an equivalent degree of ^{56}Ni mixing as that of model M19R8E1.25NI56.

For the case of $12 M_{\odot}$, we have calculated nine models. We first analyze the effect on the results of the variation of one parameter while keeping the other parameters fixed. In the upper panel of Figure 5.13 we show the effect on the LC and v_{ph} of the variation of E for a model with $R = 800 R_{\odot}$ and ^{56}Ni mixing up to $0.8 M_0$. In the bottom panels of Figure 5.13, we show the effect of varying R , for a model with $E = 1$ foe and for the same ^{56}Ni mixing. The sensitivity of the LC and v_{ph} on the extent of ^{56}Ni mixing is shown in the upper panel of Figure 5.14 for a

model with $E = 1$ foe and $R = 800 R_{\odot}$.

An examination of these Figures yields the following conclusions: 1) higher injected energy produces higher luminosity and a shorter plateau, 2) larger initial radius produces higher luminosity and a longer plateau, 3) more extended ^{56}Ni mixing produces higher luminosity and a shorter plateau, 4) ^{56}Ni mixing and initial radius have a small effect on the v_{ph} evolution as compared with that of the explosion energy, and 5) as expected, there is no effect of any of these parameters on the tail luminosity. Note that the sensitivity of the LC on E , R , and ^{56}Ni mixing is in qualitative concordance with analytic studies by Arnett (1980), Popov (1993), and previous numerical studies by Litvinova & Nadezhin (1983, 1985) and more recently by Young (2004) and Utrobin (2007).

Although we have considered several values of E , R , and ^{56}Ni mixing, neither of the models with $M = 12 M_{\odot}$ gives a good representation of the observations of SN 1999em. Note that we have calculated also two other models, M12R15E05NI56 and M12R15E08NI56, adopting even higher values of the initial radius. These models are shown in the bottom panel of Figure 5.14. Despite the good representation of the LC provided by model M12R15E05NI56, it fails to reproduce the observed photospheric velocities. We conclude that it is not possible to reproduce the observations of SN 1999em using models with a pre-supernova mass of $M = 12 M_{\odot}$. Clearly, masses lower than this value would also fail to match the observations.

For the case of $14 M_{\odot}$, we have calculated ten models for different combinations of R , E and ^{56}Ni mixing. Specifically, we used three different values of the initial radius: $R = 800, 1000$, and $1200 R_{\odot}$, four values of explosion energy: $E = 1.1, 1.0, 0.9$, and 0.8 foe, and three different degrees of ^{56}Ni mixing: $0.2, 0.5$, and $0.8 M_0$ (see Table 5.3). Figures 5.15 and 5.16 show the results of these models. At first sight we find that these models agree better with the observations than the $12 M_{\odot}$ ones. Therefore the case of $14 M_{\odot}$ deserves a more detailed analysis. As described below, we chose the grid of parameters based on the known effects of each physical parameter on the light curves and velocities, and trying to reach the best possible agreement with the observations. As noted in Section 5.1, in order to assess the validity of models we will focus on how well they reproduce the observed plateau

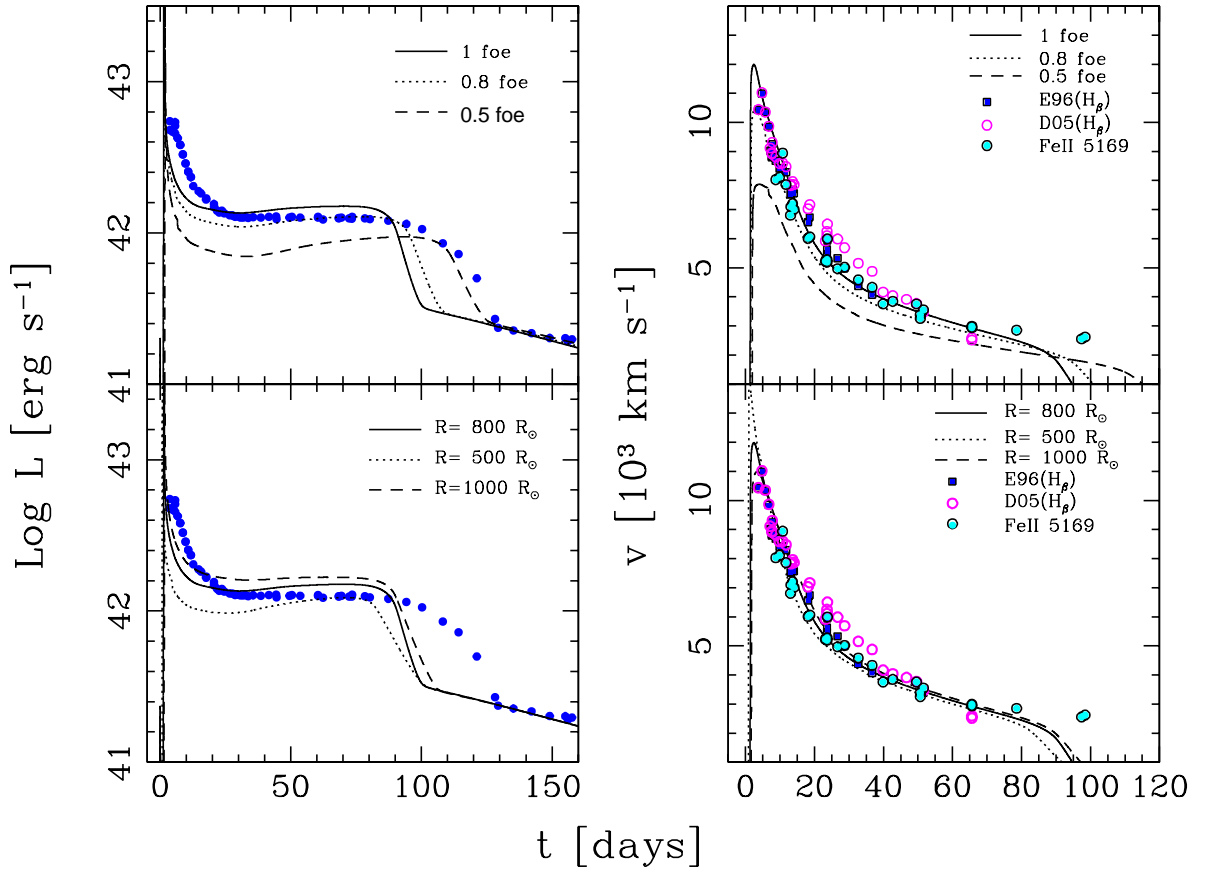


Figure 5.13: Comparison between models and observations of SN 1999em for a low value of the pre-supernovae mass of $M = 12 M_{\odot}$ and the same value of ^{56}Ni mass and mixing than for the reference model M19R8E1.25Ni56. **(Left panels):** bolometric LCs. **(Right panels):** photospheric velocity evolution. **(Upper panels):** models with different explosion energies as indicated in the labels, and a fixed value of $R = 800 R_{\odot}$. **(Lower panels):** models with different initial radii as indicated in the labels, and a fixed value of $E = 1$ foe.

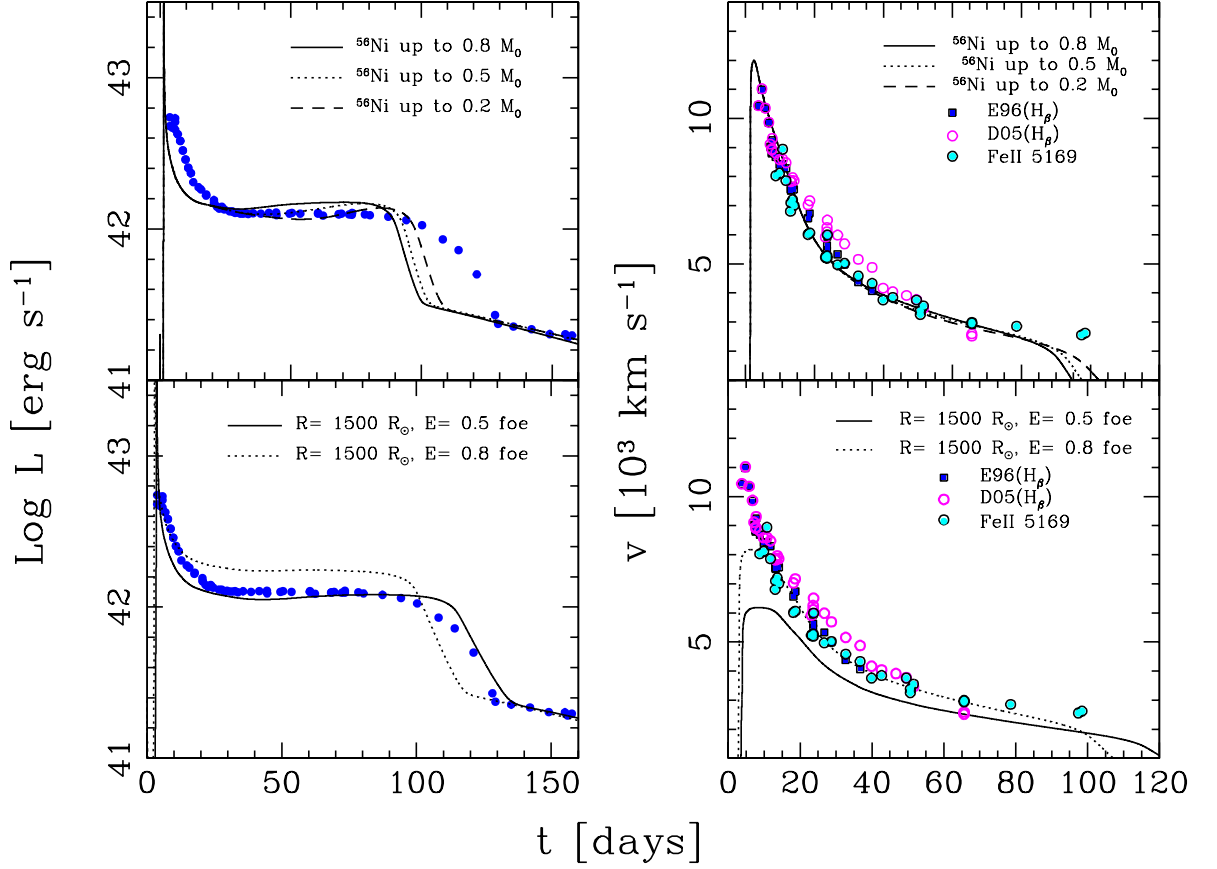


Figure 5.14: Comparison between models and observations of SN 1999em for a low value of the pre-supernovae mass of $M = 12 M_{\odot}$ and the same value of ^{56}Ni mass than for the reference model m19r8e1.25ni56. **(Left panels):** bolometric LCs. **(Right panels):** photospheric velocity evolution. **(Upper panels):** models with different mixing of ^{56}Ni , $E = 1$ foe and $R = 800 R_{\odot}$. Note that the degree of ^{56}Ni is indicated in each figure as a fraction of the initial mass of the model. **(Lower panels):** models with an initial radius of $R = 1500 R_{\odot}$ and two different values for the explosion energy as indicated (corresponding to models m12r15e08ni56 and m12r15e05ni56; see Table 5.3). Model m12r15e05ni56 reproduces very well the bolometric light curve of SN 1999em, while it underestimates the photospheric velocity evolution.

luminosity and length, and the early photospheric velocities, but we will disregard differences in the early LC before the plateau phase where the uncertainties in both models and data are the largest.

Our reference model is shown with a solid line in the upper panels of Figure 5.15 and has the following parameters: $E = 1$ foe, $R = 800 R_{\odot}$, and $0.8 M_0$ of ^{56}Ni mixing. We note that this reference model has the same initial radius and ^{56}Ni mixing as model M19R8E1.25NI56 for $19 M_{\odot}$. The energy has been reduced in order to compensate the effect on the luminosity of using a lower mass. As shown in Figure 5.15 the reference model produces the correct plateau luminosity and photospheric velocities although the plateau duration is too short as compared with the data. With the aim of remedying this situation while keeping the mass fixed we invoked lower energies and larger radii (dashed and dotted lines). While this served to improve the issue of the plateau length, the comparison with photospheric velocities at early times became poorer as expected due to the lower energies. We therefore consider these models to be unlikely. In a further attempt to find a good $14 M_{\odot}$ model, we decided to vary the mixing of ^{56}Ni while keeping the other parameters as in the reference model. The results are shown in the lower panels of Figure 5.15. We now note that while a reduction of the ^{56}Ni mixing serves to increase the length of the plateau, the shape of the LC and the plateau luminosity drift away from the observations. Thus, we can also discard these models.

Based on the above observations we tested other parameter combinations, as shown in Figure 5.16. In the upper panels we show the tests of models with slightly smaller energies and larger radii as compared with the reference model, and two different degrees of ^{56}Ni mixing. While the match of the LC for these models is satisfactory, the problem with the early-time velocities reappears, so we discard these models. In the lower panels of Figure 5.16 we show further combinations of parameters. Here we obtain an improvement in the LC while not compromising the agreement in the velocities. Among these models the one called M14R10E09NI56M provides the best match to the LC and velocity data. We therefore conclude that the $14 M_{\odot}$ scenario for SN 1999em cannot be ruled out, although the comparison with the data is not as good as that of the $19 M_{\odot}$ model (see Figure 5.3 and 5.4).

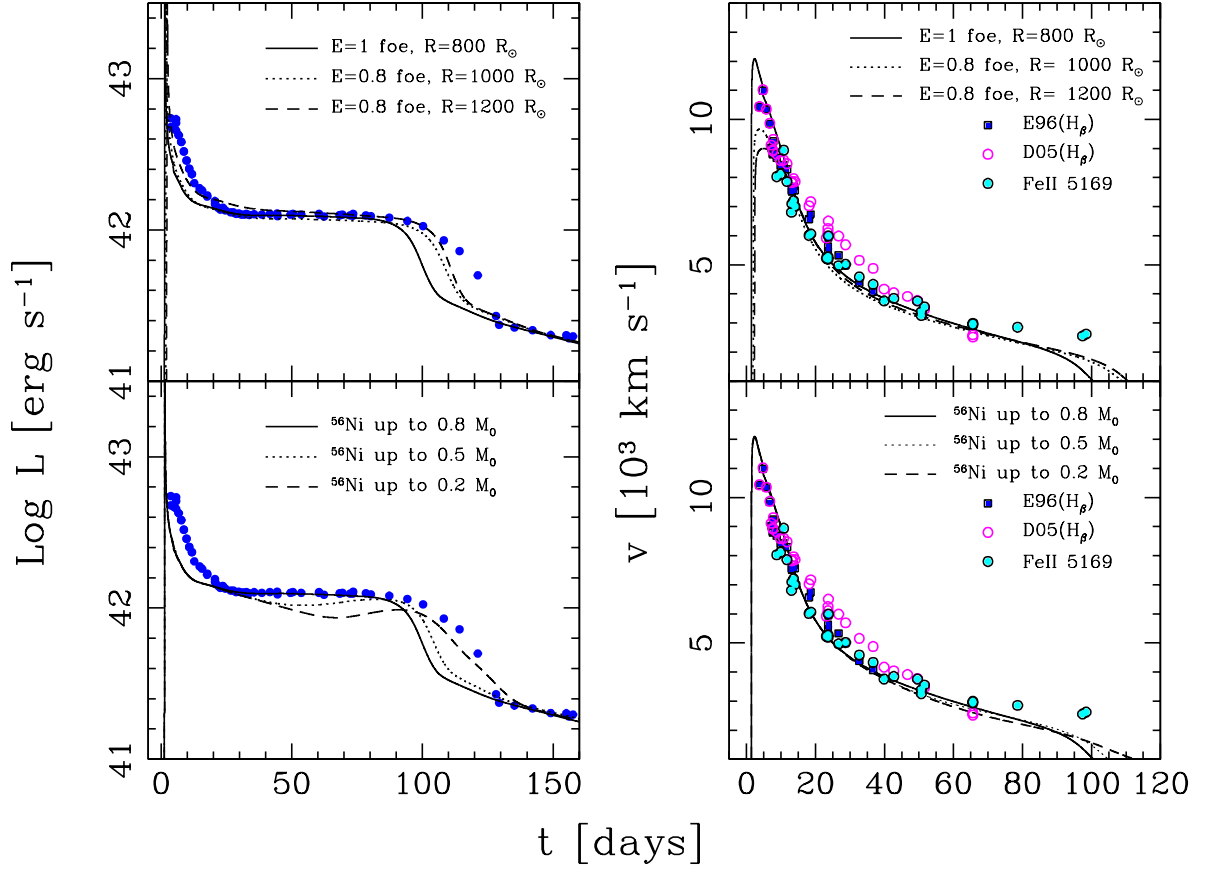


Figure 5.15: Comparison between models (lines) and observations (points) of SN 1999em for a low value of the pre-supernova mass of $M = 14 M_{\odot}$ and the same mass of ^{56}Ni as for the reference model M19R8E1.25NI56. **(Left panels):** bolometric LCs. **(Right panels):** photospheric velocity evolution. **(Upper panels):** models M14R8E1NI56, M14R10E08NI56 and M14R12E08NI56 (see Table 5.3). **(Lower panels):** models with different mixing of ^{56}Ni , $E = 1$ foe and $R = 800 R_{\odot}$. Note that the degree of ^{56}Ni is indicated in each panel as a fraction of the initial mass of the model.

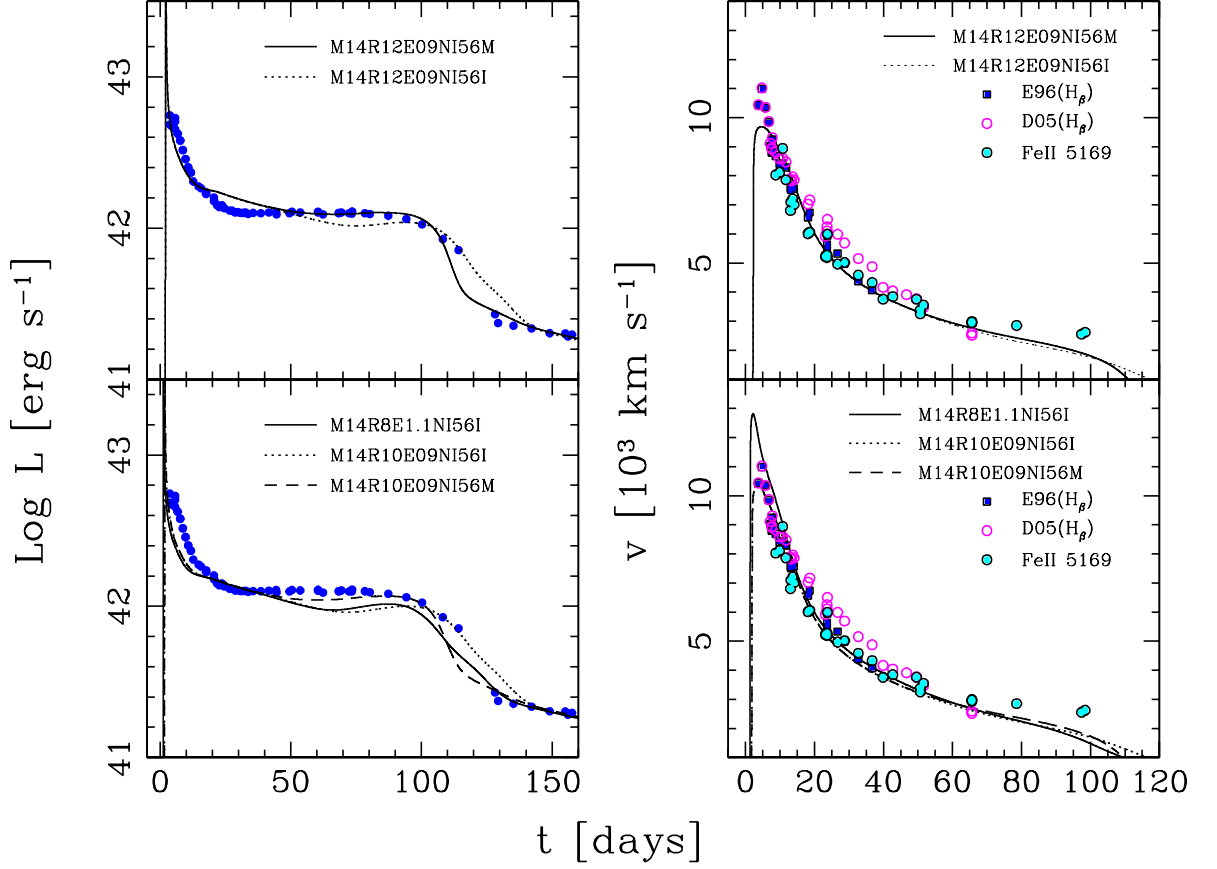


Figure 5.16: Comparison between models (lines) and observations (points) of SN 1999em for a low value of the pre-supernova mass of $M = 14 M_{\odot}$ and the same mass of ^{56}Ni as for the reference model M19R8E1.25NI56. **(Left panels):** bolometric LCs. **(Right panels):** photospheric velocity evolution. **(Upper panels):** models M14R8E1.1NI56I, M14R10E09NI56I and M14R10E09NI56M. **(Lower panels):** models M14R12E09NI56M and M14R12E09NI56I (see Table 5.3).

Table 5.3: Model Parameters

Model	Mass [M_{\odot}]	Radius [R_{\odot}]	Energy [foe]	Ni mixing ^a
M12R8E1Ni56	12	800	1	0.8
M12R8E08Ni56	12	800	0.8	0.8
M12R8E05Ni56	12	800	0.5	0.8
M12R5E1Ni56	12	500	1	0.8
M12R10E1Ni56	12	1000	1	0.8
M12R8E1Ni56M	12	800	1	0.5
M12R8E1Ni56IN	12	800	1	0.2
M12R15E05Ni56	12	1500	0.5	0.8
M12R15E08Ni56	12	1500	0.8	0.8
M14R8E1Ni56	14	800	1	0.8
M14R10E08Ni56	14	1000	0.8	0.8
M14R12E08Ni56	14	1200	0.8	0.8
M14R8E1Ni56M	14	800	1	0.5
M14R8E1Ni56I	14	800	1	0.2
M14R8E1.1Ni56I	14	800	1.1	0.2
M14R10E09Ni56M	14	1000	0.9	0.5
M14R10E09Ni56I	14	1000	0.9	0.2
M14R12E09Ni56M	14	1200	0.9	0.5
M14R12E09Ni56I	14	1200	0.9	0.2

^a The degree of ^{56}Ni mixing is given as a fraction of the initial mass of the model (M_0)

Chapter 6

Observed and Physical Properties

In this chapter I use the database presented in chapter 2 to examine the observed and physical properties of this sample of SNe II-P. I begin by calculating bolometric light curves and effective temperature evolution for the complete sample of SNe II-P in § 6.1. Then, I proceed to derive different parameters that characterize the bolometric LC, and I find that the SN sample shows a range of 1.15 dex in plateau luminosity, and plateau durations between 64 and 103 days. Comparing the shape of the transition between the plateau and the radioactive tail, I find that the size of the drop in luminosity is in the range 0.35 to 1.46 dex. The radioactive nickel masses calculated for all the SNe in our sample **except for SN 1992am** are below $0.1 M_{\odot}$. In section 6.2 I calculate a grid of hydrodynamical models for a range of initial masses, radii, explosion energies, nickel masses, and mixing. From this set of models and the observations I study correlations between different observed and physical parameters in § 6.3.

6.1 Application to SN II-P Data

In this section, we apply the calibrations for bolometric corrections and effective temperatures presented in chapter § 4 to our sample of 37 SNe II-P. Note that in order to calculate bolometric light curves we just need to apply equation (4.4) of § 4.1.2. Thus, we need to have (1) *BVI* photometry, (2) extinction corrections due to our own Galaxy, (3) host-galaxy extinction corrections, and (4) distances. We obtained Galactic extinction values from Schlegel et al. (1998) (see Table 2.1 of chapter 2). Host-galaxy extinctions and distances for most of the present sample were calculated by Olivares et al. (2009) and they are presented in Table 2.3 of § 2.2.

Figures 6.1 – 6.10 present the bolometric light curves and effective temperatures for the 37 SNe II-P in our sample. In order to place all the SNe in the same time scale and facilitate the comparison among them, the origin of time used is the middle point of the transition between the plateau and the radioactive tail (t_{PT} ; see § 2.3 and Table 2.3). A simple inspection of the resulting bolometric light curves reveals a high degree of heterogeneity and a variety of LC morphologies.

There are ~ 16 SNe which were observed previous to the plateau phase, i.e. during the adiabatic cooling phase. Among these, there are three subluminous objects, SN 1999br, SN 2003bl and SN 2005cs which, in comparison with the rest, appear to have a steeper slope during the adiabatic cooling phase and a flatter plateau. Note, however, that in none of the cases we have data covering the maximum produced promptly after shock breakout, as predicted by the models. This lack of observation at maximum light is consistent with the prediction that such peak has a very short duration (a few hours), making it very difficult to observe. Only in recent years it was possible to observe this elusive phase and to detect the shock breakout for two SNe II-P thanks to observations at UV wavelength or to the grater cadence of the the Supernova Legacy Survey (SNLS) (Gezari et al., 2008; Tominaga et al., 2009).

In all cases where we observe a plateau the bolometric luminosity remains nearly constant, slowly decreases, but never increases. Utrobin (2007) has predicted, and we have also tested this with our models, that part of the dense core of the massive star

should be ejected in order to produce a plateau phase as observed. On the contrary, if the whole core remains in the compact remnant and the density profile encountered by the shock wave in the envelope is relatively flat, the resulting luminosity increases with time (see for example Figure 3.6 of § 3.1.4). Our data suggest that all SN II-P ejecta involve part of the dense core of the progenitor star. Also note that our sample of SNe shows different slopes —though never positive— during the “plateau”. Some SNe are more linearly declining instead of showing an obvious plateau in bolometric luminosity. Such is the case of SN 1999ca, SN 2002hx, SN 2002hj, SN 2003cn, SN 2003ci and SN 2003ip. We call these “intermediate-plateau” SNe. If we consider the definition of Type II-L SNe (SNe II-L) as those objects which show a linear, uninterrupted luminosity decline until they reach the radioactive tail phase (Turatto, 2003), then SN 2002hx could perhaps be classified as SN II-L. Interestingly, the existence of this group of intermediate SNe with tilted “plateaus” suggests a possible continuous connection between SNe II-P and SNe II-L, with the differences probably related to the progenitor mass. In this scenario, SNe II-L would have lower envelope masses probably due to mass loss during the progenitor evolution, although there are alternative explanations (see Swartz et al. (1991)). A quantitative classification based on the average decline rate of the first 100 days of the light curve was given by Patat et al. (1994). In the following, we decided to include these intermediate SNe with the aim of showing how their observable properties compare with the genuine SNe II-P and we leave for future research a more precise definition of the limiting value of the “plateau” slope which would serve to divide both subclasses on the basis of their physical properties. It is important to keep in mind, however, that our code may not be suitable to model SNe II-L if such objects experience interaction with the circumstellar medium.

To make a quantitative comparison between different SNe in our sample, we define a series of parameters that can be measured on the bolometric LC: (1) plateau luminosity (L_P), defined as the mean value between days -20 and -80 with respect to t_{PT} ; (2) plateau duration (Δt_P), defined as the interval of time (in the rest frame of the SN) during which the luminosity remains within ± 0.2 dex of the mean value (L_P); (3) post-plateau drop ($\Delta \log L$), defined as the logarithmic difference in luminosity between L_P and the tail luminosity calculated at day 20 with respect to t_{PT} ; and (4) ^{56}Ni mass produced during the explosion (M_{Ni}). As examples we show in Figure 6.11

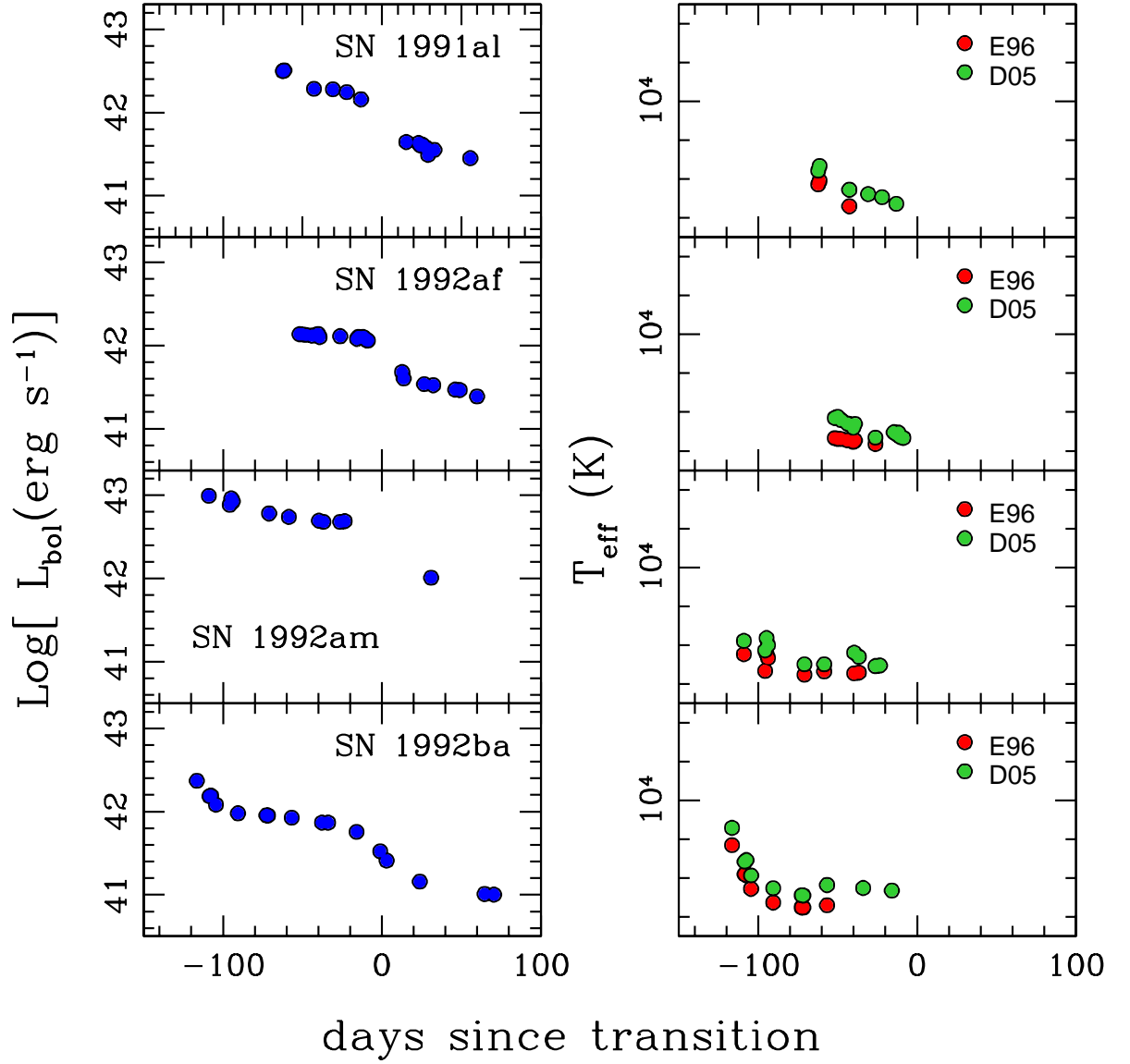


Figure 6.1: Bolometric luminosity (**left**) and effective temperatures (**right**) for SNe II-P as a function of time (part 1). The origin of time is the middle point between the plateau and the linear tail (t_{PT}), as defined by Olivares et al. (2009) (see Table 2.3 of § 2.3).

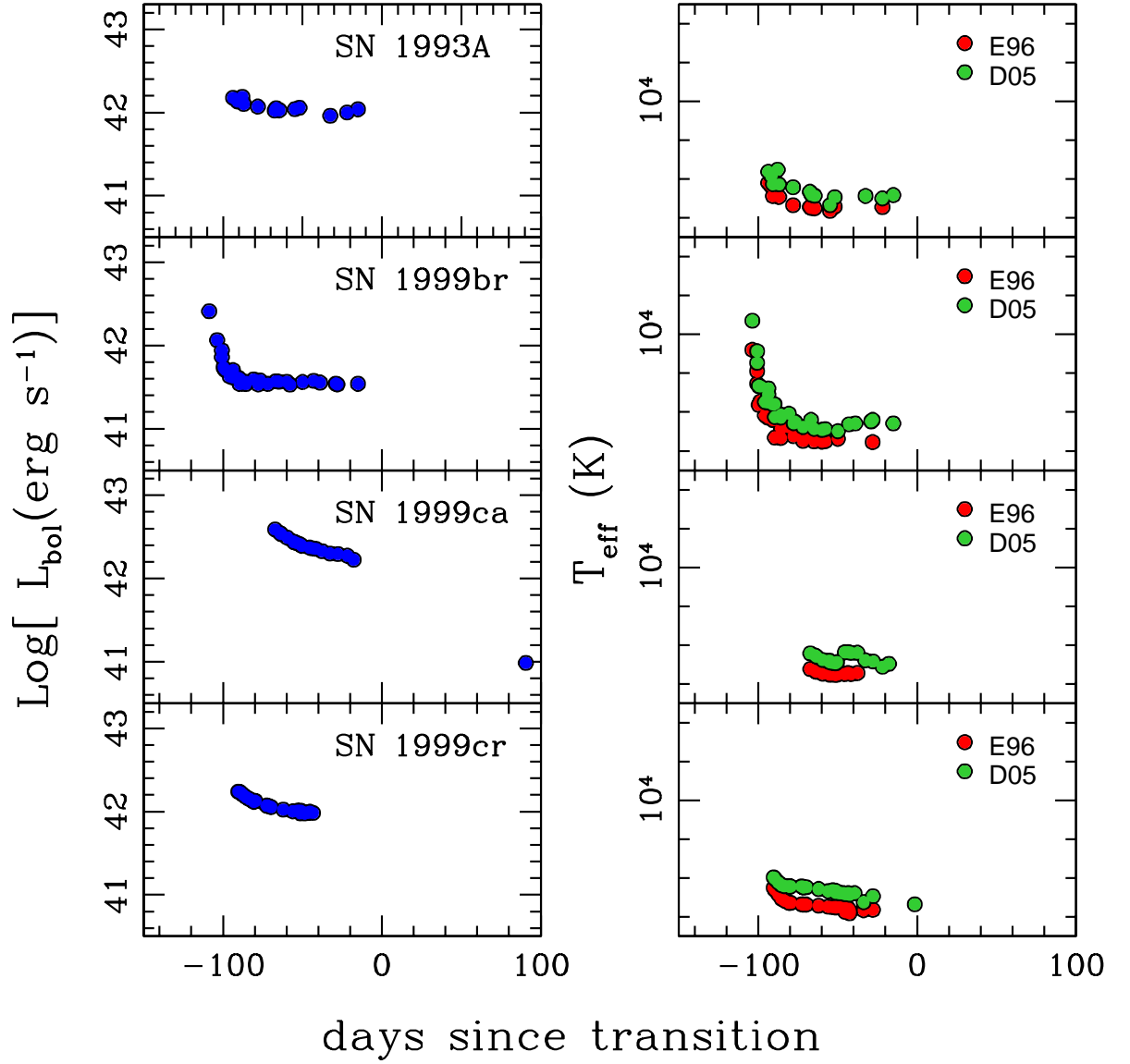


Figure 6.2: Bolometric luminosity (**left**) and effective temperatures (**right**) for SNe II-P as a function of time (part 2). The origin of time is the middle point between the plateau and the linear tail (t_{PT}) as defined by Olivares et al. (2009) (see Table 2.3 of § 2.3).

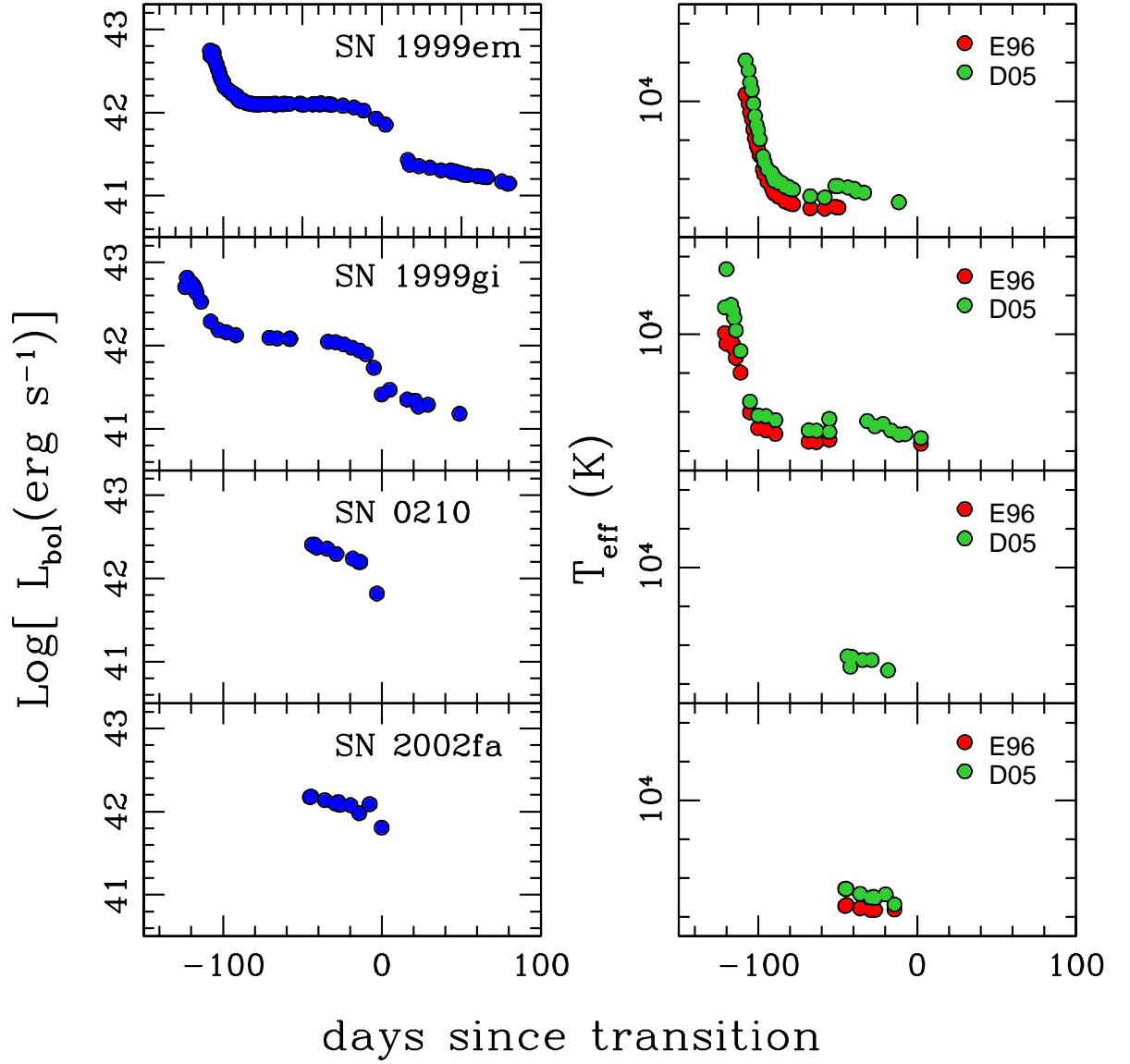


Figure 6.3: Bolometric luminosity (**left**) and effective temperatures (**right**) for SNe II-P as a function of time (part 3). The origin of time is the middle point between the plateau and the linear tail (t_{PT}) as defined by Olivares et al. (2009) (see Table 2.3 of § 2.3).

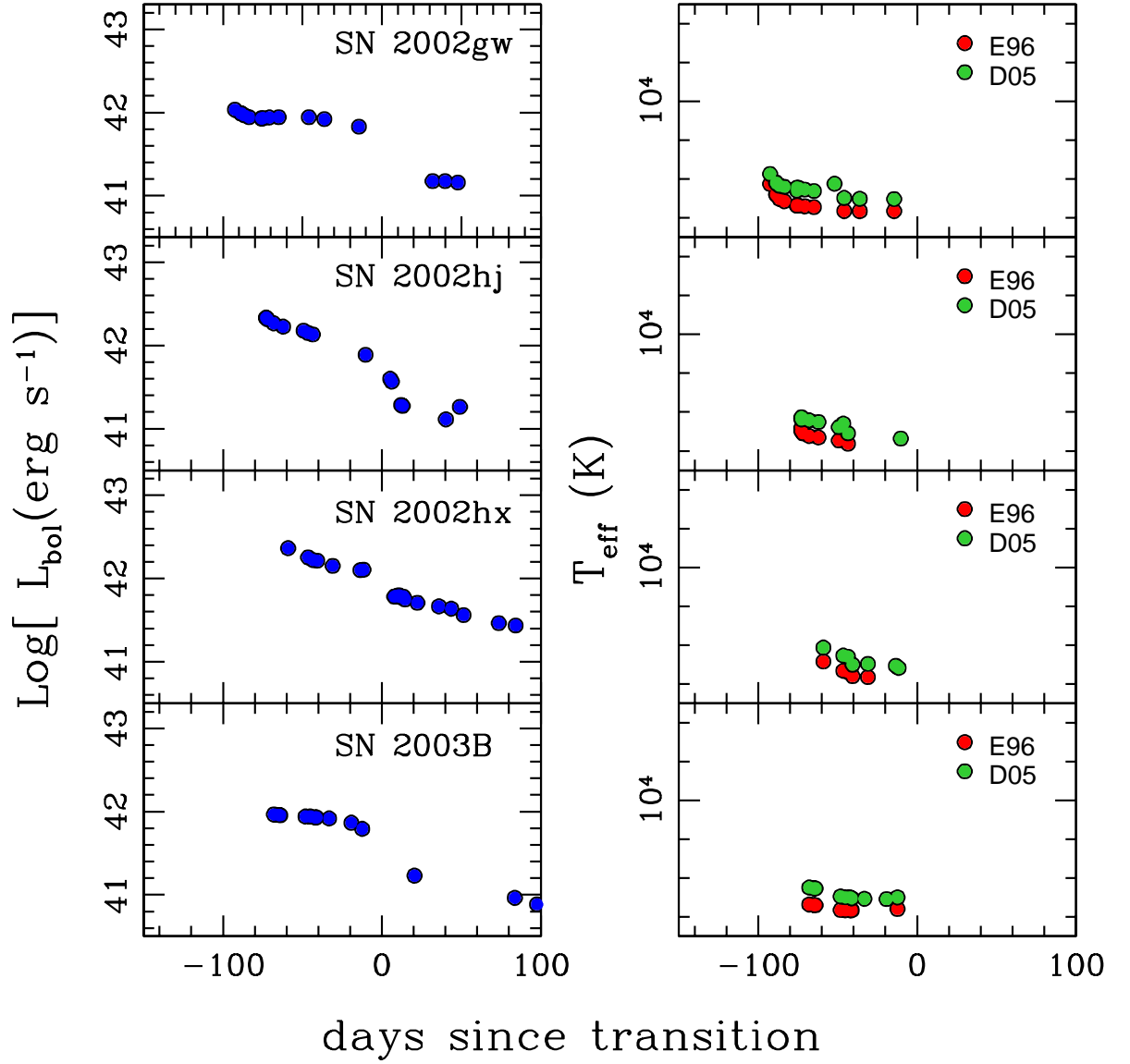


Figure 6.4: Bolometric luminosity (**left**) and effective temperatures (**right**) for SNe II-P as a function of time (part 4). The origin of time is the middle point between the plateau and the linear tail (t_{PT}) as defined by Olivares et al. (2009) (see Table 2.3 of § 2.3).

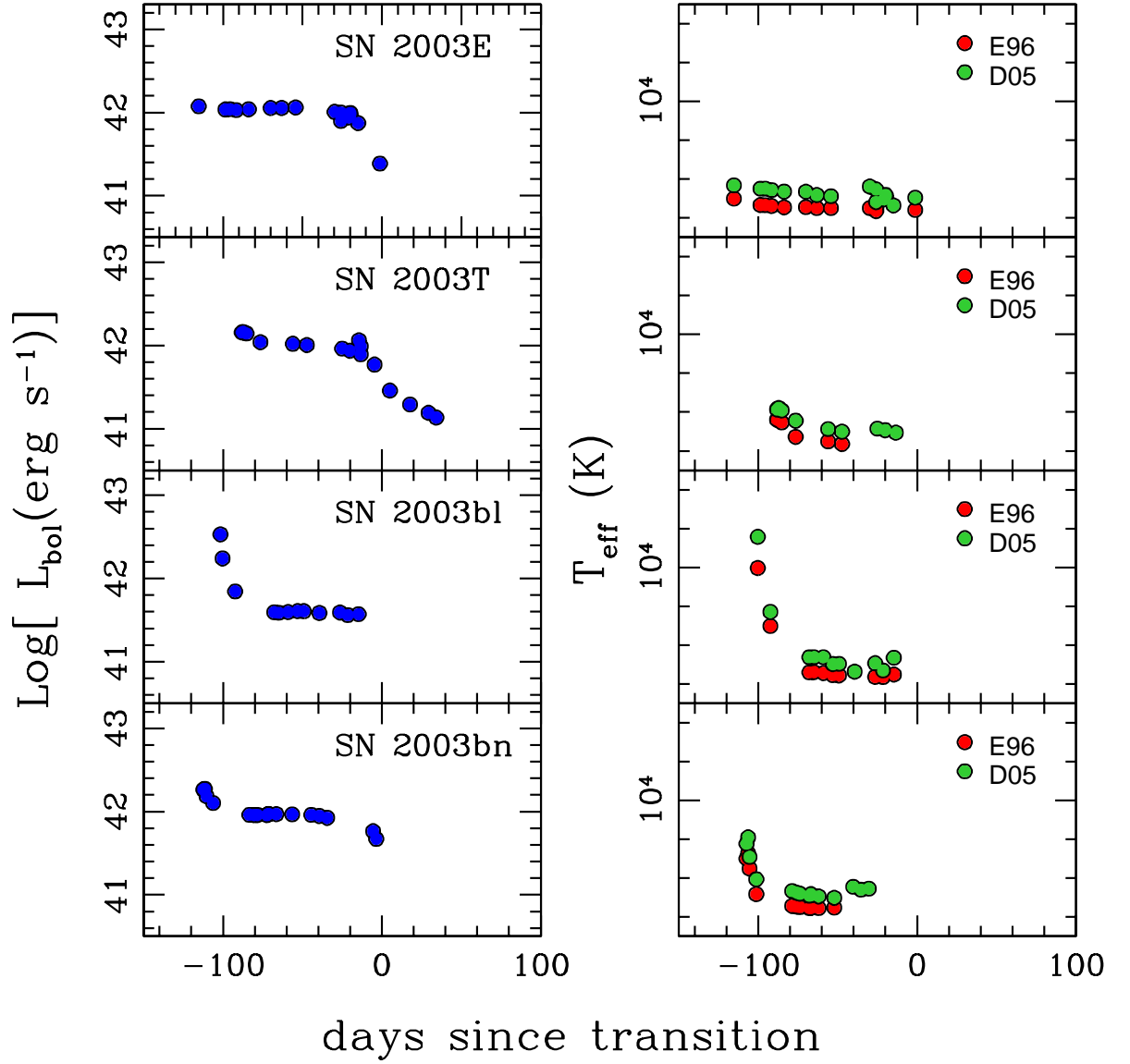


Figure 6.5: Bolometric luminosity (**left**) and effective temperatures (**right**) for SNe II-P as a function of time (part 5). The origin of time is the middle point between the plateau and the linear tail (t_{PT}) as defined by Olivares et al. (2009) (see Table 2.3 of § 2.3).

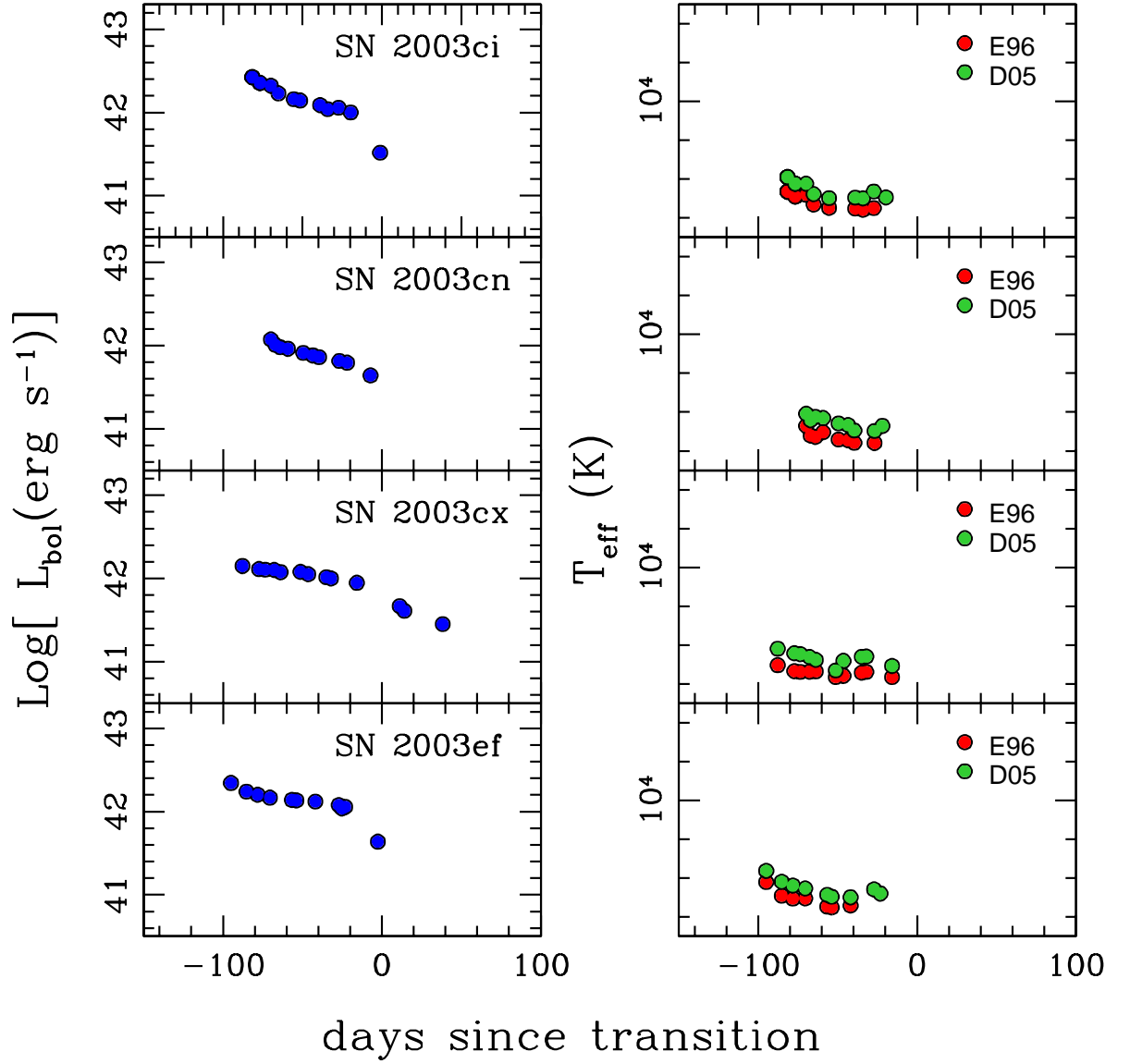


Figure 6.6: Bolometric luminosity (**left**) and effective temperatures (**right**) for SNe II-P as a function of time (part 6). The origin of time is the middle point between the plateau and the linear tail (t_{PT}) as defined by Olivares et al. (2009) (see Table 2.3 of § 2.3).

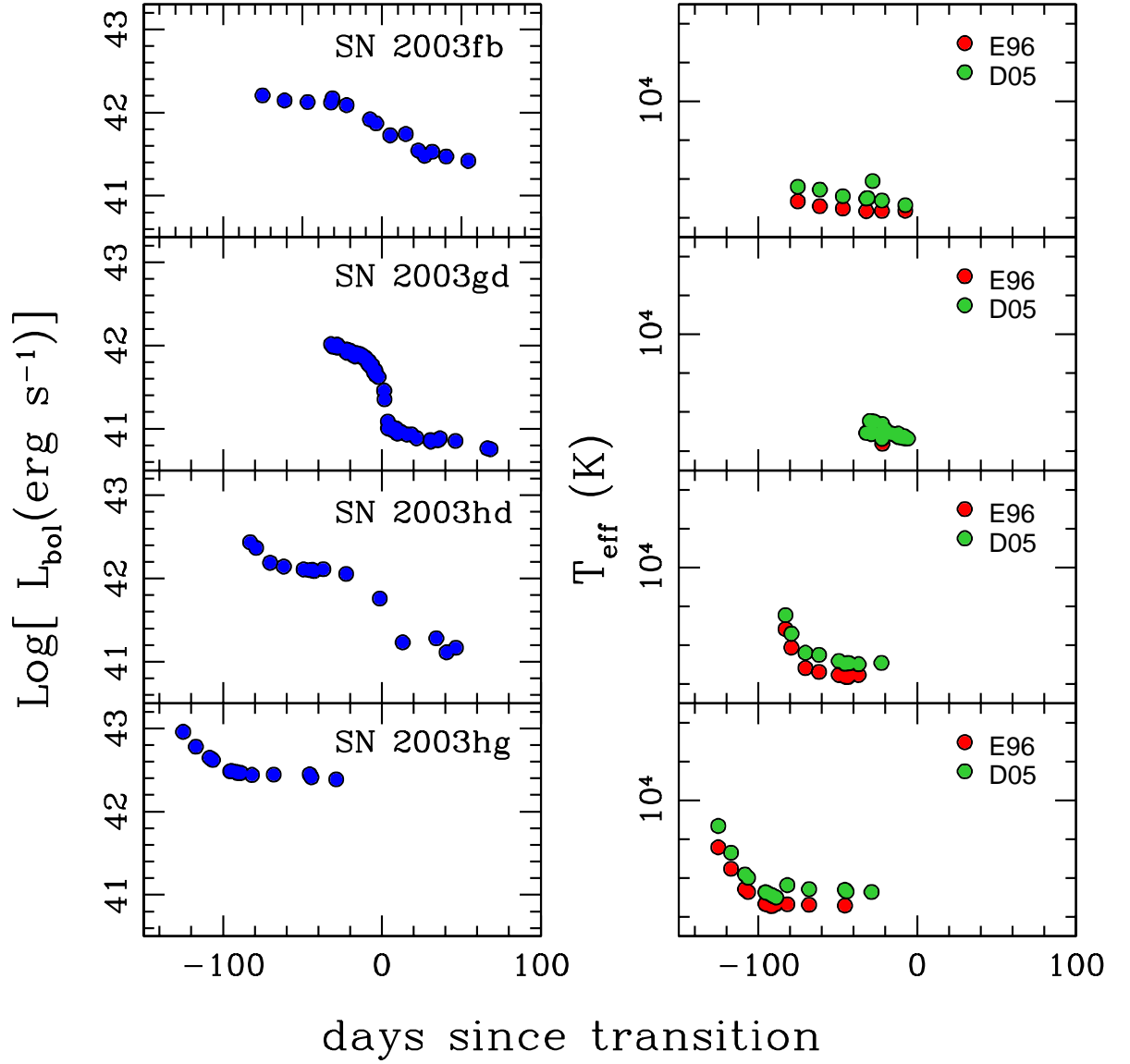


Figure 6.7: Bolometric luminosity (**left**) and effective temperatures (**right**) for SNe II-P as a function of time (part 7). The origin of time is the middle point between the plateau and the linear tail (t_{PT}) as defined by Olivares et al. (2009) (see Table 2.3 of § 2.3).

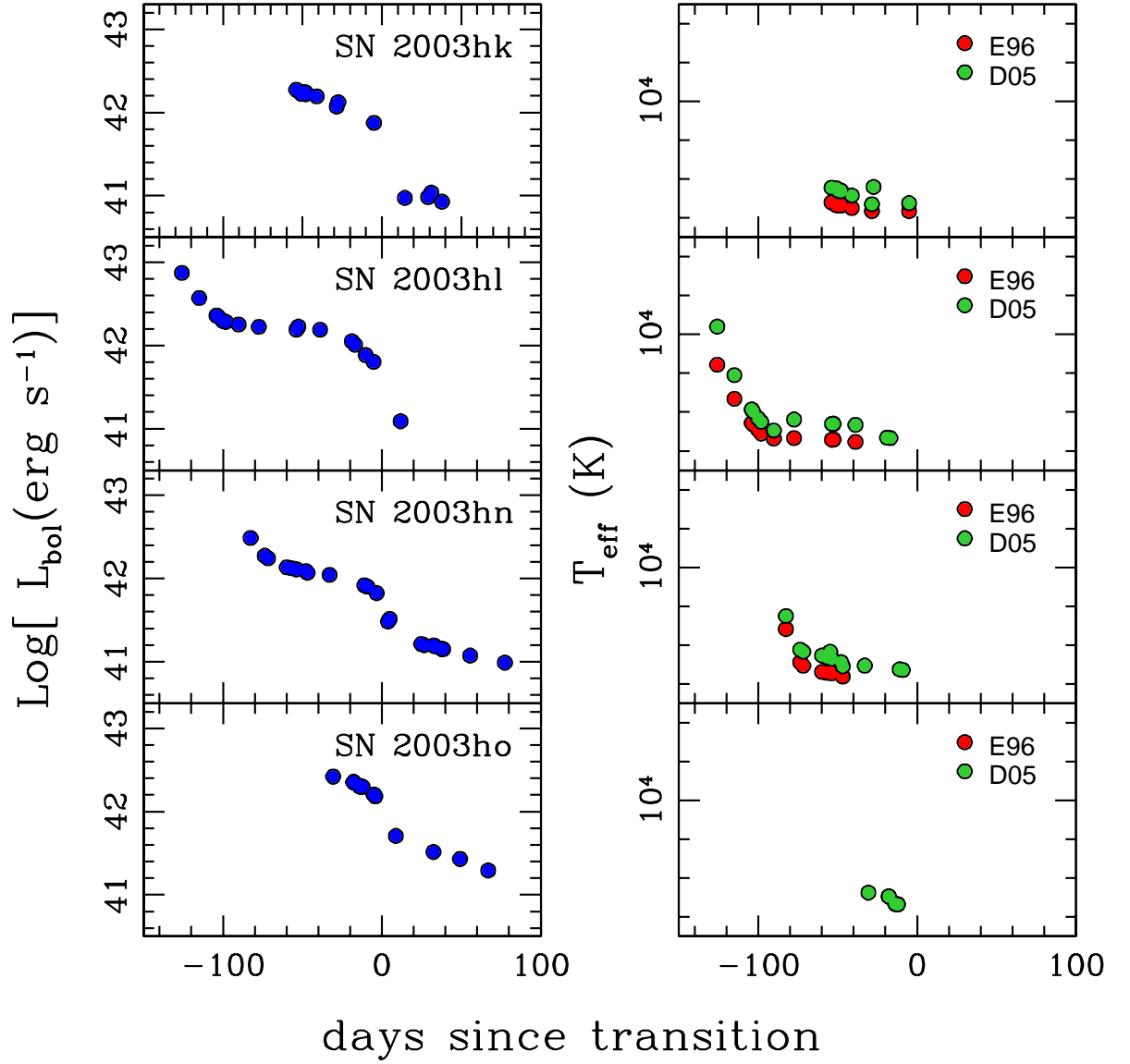


Figure 6.8: Bolometric luminosity (**left**) and effective temperatures (**right**) for SNe II-P as a function of time (part 8). The origin of time is the middle point between the plateau and the linear tail (t_{PT}) as defined by Olivares et al. (2009) (see Table 2.3 of § 2.3).

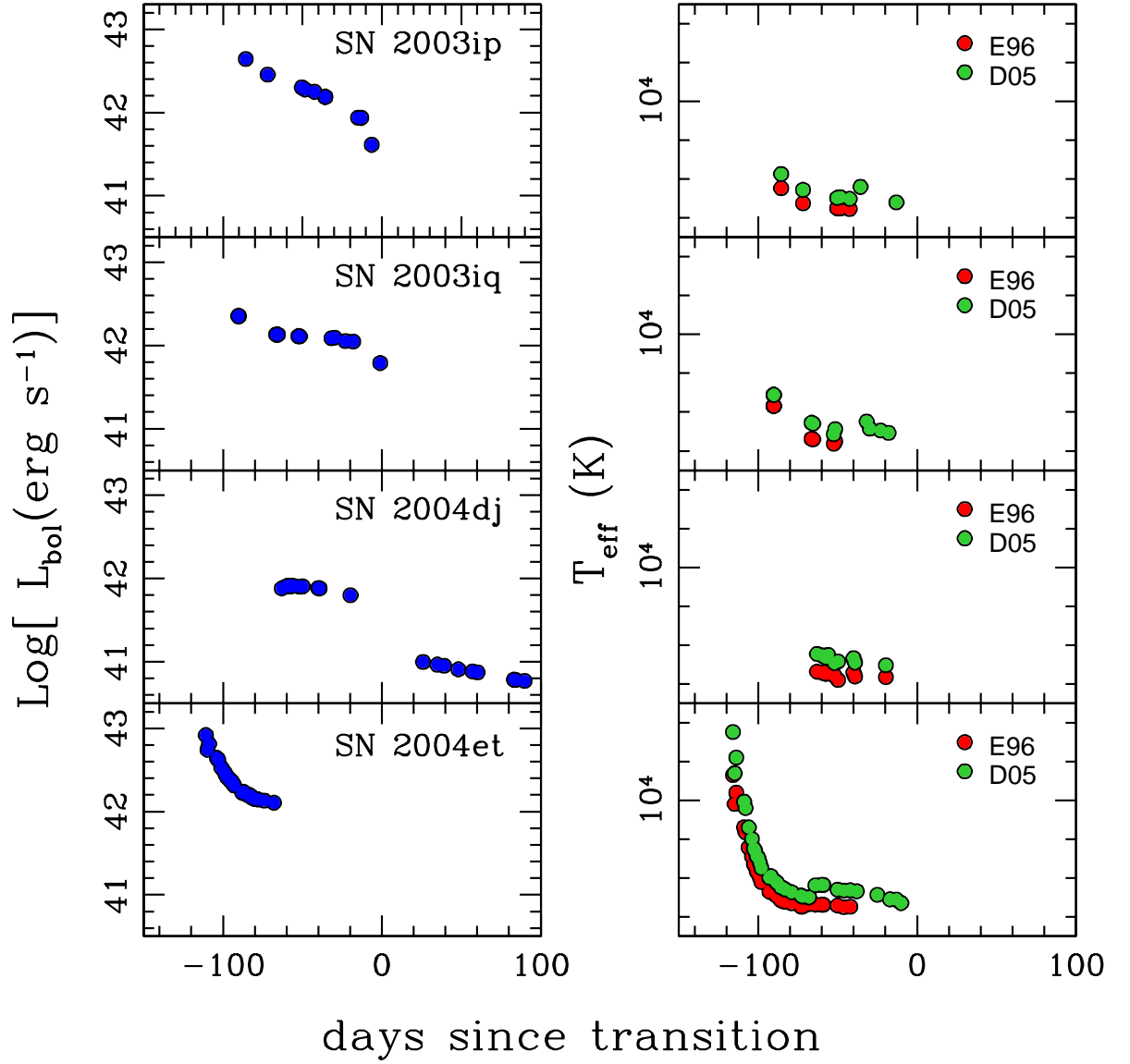


Figure 6.9: Bolometric luminosity (**left**) and effective temperatures (**right**) for SNe II-P as a function of time (part 9). The origin of time is the middle point between the plateau and the linear tail (t_{PT}) as defined by Olivares et al. (2009) (see Table 2.3 of § 2.3).

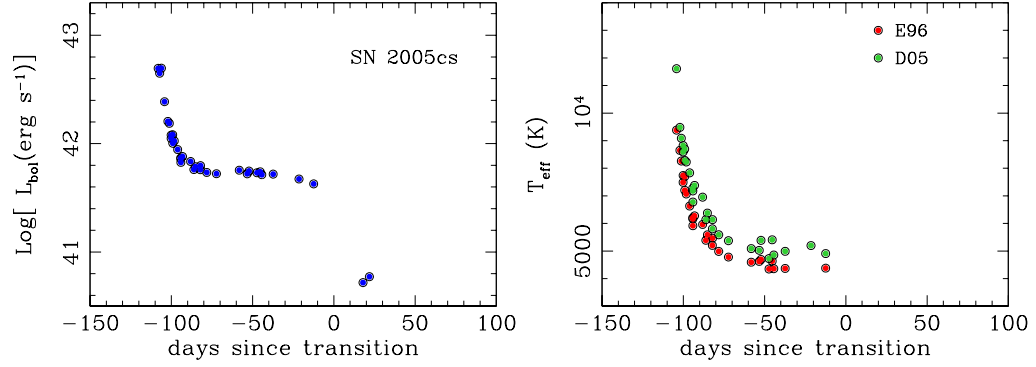


Figure 6.10: Bolometric luminosity (**left**) and effective temperatures (**right**) for SNe II-P as a function of time (part 10). The origin of time is the middle point between the plateau and the linear tail (t_{PT}) as defined by Olivares et al. (2009) (see Table 2.3 of § 2.3).

the bolometric LC for SN 1992ba, SN 1999em, SN 2002gw and SN 2003hl together with their parameters (1)–(4). In Table 6.1 we list the values of the parameters and their uncertainties for all the SNe in our sample. In the following subsection we give a detailed explanation of the calculation of these parameters, and their characteristic values and distributions.

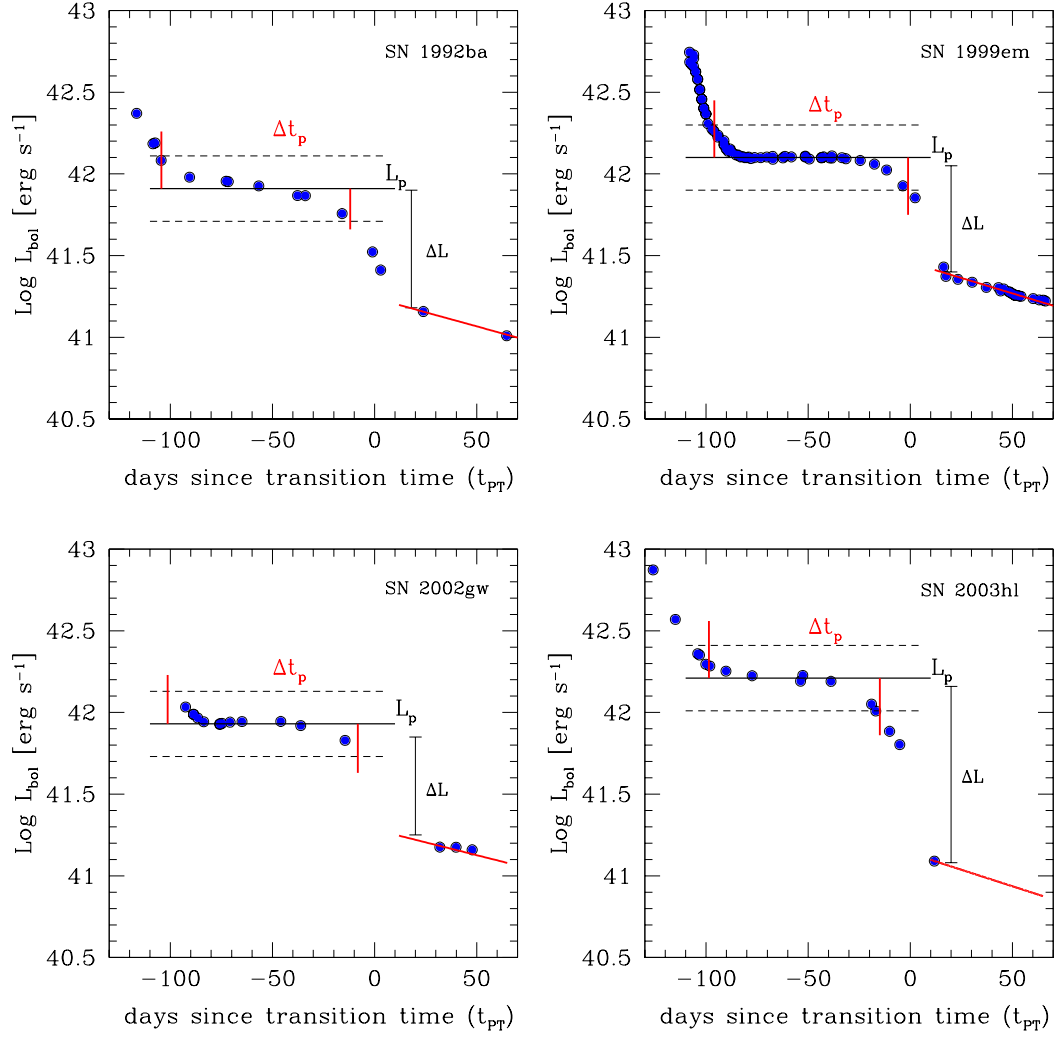


Figure 6.11: Bolometric LC and observed parameters (L_P , Δt_P , ΔL and M_{Ni}) for four SNe in our sample (see Table 6.1).

Table 6.1: Observed Parameters for SNe II-P

SN Name	t_0^a [JD-2448000]	Δt_p [days]	$\text{Log } L_p$ [erg s $^{-1}$]	$\Delta \text{Log } L$ [erg s $^{-1}$]	M_{Ni} M_\odot
1991al	410.00(30)	77.50(30.2)	42.32(0.05)	0.701(0.058)	0.091(0.011)
1992af	736.00(30)	97.65(29.9)	42.12(0.04)	0.526(0.045)	0.093(0.013)
1992am	778.10(11)	82.54(12.6)	42.71(0.04)	0.653(0.057)	0.405(0.099)
1992ba	883.90(3)	92.41(6.4)	41.91(0.05)	0.738(0.051)	0.041(0.006)
1993A	985.50(10)	89.44(31.9)	42.02(0.04)
1999br	3275.6(7.7)	91.26(0.7)	41.56(0.04)	0.763(0.057)	0.013(0.003)
1999ca	280.00(10)	58.36(5.9)	42.38(0.02)	0.929(0.131)	0.027(0.002)
1999cr	221.50(10)	74.80(10.5)	42.00(0.03)
1999em	3476.3(1.1)	94.92(8.3)	42.10(0.02)	0.718(0.024)	0.055(0.003)
1999gi	3517.0(1.2)	97.30(5.1)	42.06(0.04)	0.738(0.047)	0.056(0.006)
0210	...	> 31.40 ^b	42.36(0.06)
2002fa	...	> 41.61 ^b	42.13(0.05)	0.350(0.057)	...
2002gw	4557.9(2.7)	93.14(38.6)	41.93(0.04)	0.713(0.065)	0.040(0.004)
2002hj	...	> 48.56 ^b	42.22(0.04)	0.972(0.065)	0.036(0.009)
2002hx	...	> 59.37 ^b	42.23(0.05)	0.489(0.053)	0.087(0.008)
2003B	...	> 58.58 ^b	41.94(0.04)	0.704(0.043)	...
2003E	...	> 102.70 ^b	41.99(0.04)
2003T	4654.2(2.7)	85.97(56.7)	41.99(0.05)	0.717(0.051)	0.035(0.006)
2003bl	4692.6(2.8)	75.81(9.8)	41.59(0.04)
2003bn	4693.4(2.7)	102.34(4.8)	41.96(0.04)	0.792(0.057)	0.036(0.010)
2003ci	...	56.09(47.9)	42.14(0.05)
2003cn	...	58.34(10.3)	41.90(0.04)	1.457(0.057)	0.005(0.002)
2003cx	...	> 80.25 ^b	42.06(0.04)	0.478(0.045)	...
2003ef	4759.8(4.7)	75.76(37.4)	42.11(0.17)
2003fb	...	> 65.99 ^b	42.14(0.05)	0.521(0.064)	...
2003gd	4716.5(21)	93.76(21.0)	41.97(0.03)	1.032(0.035)	0.020(0.001)
2003hd	...	64.10(7.3)	42.12(0.04)	0.886(0.063)	0.036(0.005)
2003hg	...	98.02(7.8)	42.42(0.06)
2003hk	...	> 45.88 ^b	42.18(0.04)	1.201(0.051)	...
2003hl	4872.3(1.7)	89.75(7.7)	42.21(0.06)	1.150(0.057)	0.032(0.009)
2003hn	4859.5(3.8)	64.72(12.0)	42.12(0.04)	0.882(0.039)	0.036(0.003)
2003ho	...	> 24.36 ^b	42.42(0.11)	0.820(0.116)	...
2003ip	...	47.23(16.8)	42.25(0.05)
2003iq	4909.6(4.3)	75.88(10.7)	42.10(0.04)
2004dj	5167(21)	83.61(21.9)	41.90(0.04)	0.894(0.038)	0.028(0.002)
2004et	5270.5(2)	88.01(7.9)	42.10(0.03)
2005cs	5549.9(1)	86.71(5.8)	41.72(0.05)	0.989(0.065)	0.016(0.003)

^a We generally use $t_0(E96)$ (see Table 2.3 of § 2.3) as the explosion time. In case that this value is not available we use $t_0(D05)$ (see Table 2.3 of § 2.3). If neither value is available we adopt estimations of t_0 found in the literature (see § 2.3). Note that the explosion time is used to calculate M_{Ni} and both $t_0(E96)$ and $t_0(D05)$ provide consistent values for this parameter.

^b Lower bound for Δt_p .

6.1.1 Plateau Luminosity: L_p

In order to estimate the value of this parameter we average the bolometric luminosity between two well-defined epochs. The choice of -20 and -80 days for this was based on the behavior shown by most SNe. Column 4 of Table 6.1 shows the resulting values of this parameter and their uncertainties. The estimation of the uncertainty was done considering the one in the bolometric luminosity whose sources are (1) photometry, (2) extinction (see Table 2.3), (3) distance (see Table 2.3) and (4) calibration of the bolometric correction. For the latter component, a value of 0.11 mag was adopted during the plateau, and of 0.02 mag during the tail (see § 4.1.2). Figure 6.12 shows the distribution of this parameter among our SNe. We see that the intermediate-plateau SNe have plateau luminosities which are consistent with the genuine SNe II-P. The histogram reveals that most of the SNe II-P (22 out of 37) have a characteristic plateau luminosity between $7.9 \times 10^{41} \text{ erg s}^{-1}$ and $1.6 \times 10^{42} \text{ erg s}^{-1}$. There is only one object, namely SN 1992am, with $L_p > 3.16 \times 10^{42} \text{ erg s}^{-1}$ and two SNe (SN 1999br and SN 2003bl) with $L_p < 5 \times 10^{41} \text{ erg s}^{-1}$.

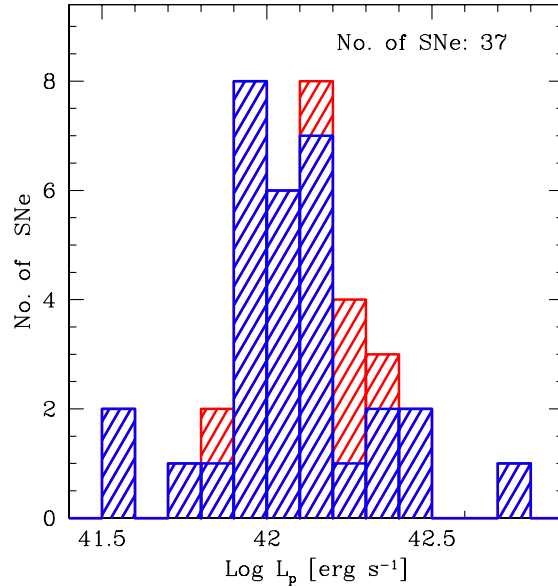


Figure 6.12: The distribution of L_p for SNe II-P. The SNe considered as intermediate between plateau and linear (see § 6.1) are marked in red.

In Figure 6.13 we compare six exemplary SNe to illustrate that SNe II-P display a wide range of plateau luminosities similar to the result reported by (Hamuy, 2001) using V-band light curve. The range of luminosities encompassed by our sample is 1.15 dex, equivalent to more than one order of magnitude of spread in their radiative energy output. The weighted average value of the characteristic plateau luminosity in our sample is $\langle L_P \rangle = 1.26 \pm 0.019 \times 10^{42} \text{ erg s}^{-1}$.

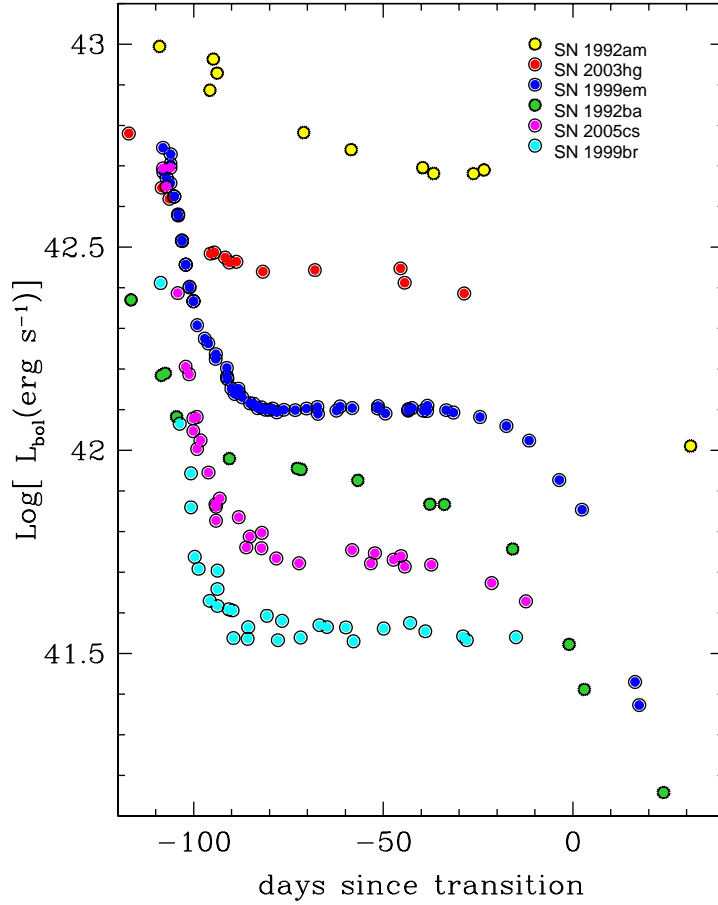


Figure 6.13: Bolometric light curves for five SNe of our sample showing the range of variation of plateau luminosities.

6.1.2 Plateau duration: Δt_p

The estimate of this parameter requires the calculation of two characteristic times: (1) the point where the $L = L_p + \delta L$ (L_+), called t_+ , and (2) the point where the $L = L_p - \delta L$ (L_-), called t_- . Here, δL represents the range of luminosity adopted to define the plateau phase. We chose a value of 0.2 dex which is equivalent to a variation of 1 mag. Note that t_+ always occurs before t_- given the monotonic behavior of the LC. Thus by definition, $\Delta t_P = (t_- - t_+)/(1 + z)$, where z is the redshift of the SN. Although it is straight-forward in theory to define Δt_P , in practice its calculation involves some problems especially for those SNe which do not have good temporal coverage. We found the following cases: (a) SNe with data for $L > L_+$ and $L < L_-$, (b) SNe with data only for $L < L_+$, and (c) SNe with data only for $L > L_-$.

In most of cases (a), we can determine t_+ and t_- and their uncertainties by interpolating between the nearest points on both sides of L_+ and L_- , respectively. When such points are separated by more than 30 days from each other an extrapolation is performed based on the two points right below L_+ for t_+ , or above L_- for t_- . In cases (b) and (c) it was only possible to find t_+ or t_- , respectively, by extrapolation.

In order to compute Δt_P for SNe with poorer coverage, we use data of SNe with the best coverage to derive typical time intervals which in turn allow to obtain t_- or t_+ . For the estimation of t_- , we use the typical interval found between this moment and the transition time, i.e. $\Delta t_- = (t_{PT} - t_-)/(1 + z)$. A weighted average, $\langle \Delta t_- \rangle$, and its uncertainty is computed for the 13 SNe which allow a direct determination of t_- . We find $\langle \Delta t_- \rangle = 8.3 \pm 0.5$ days, i.e, 8.3 days before the middle point of the transition between plateau and tail. This value is then used to obtain t_- for other SNe based on their values of t_{PT} .

A similar procedure can be followed for the estimate of t_+ . In this case its application requires knowledge of the explosion time (t_0). For 13 SNe with both estimates of t_+ and t_0 , we compute the interval between those times, $\Delta t_+ = (t_+ -$

$t_0)/(1+z)$, and its uncertainty. A weighted average of these values is obtained, $\langle \Delta t_+ \rangle = 22.0 \pm 1.5$ days. This means that, on average, SNe II-P enter the plateau phase approximately 22 days after explosion. This result is in very good agreement with predictions from hydrodynamical models. We are thus able to estimate t_+ using the average above only when the explosion time is known. There are ten additional objects for which we can only estimate a lower limit of t_+ and thus of Δt_p . Column 3 of Table 6.1 shows the values of Δt_p and their uncertainties. The values corresponding to lower bounds of Δt_p are preceded by the $>$ symbol.

Figure 6.14 shows the distribution of Δt_p (excluding lower limits). The histogram shows that most SNe (20 out of 27) have Δt_p values between 75 and 105 days and the peak is around 90 days. Although the sample is small, we see hints of a bi-modal distribution with a secondary peak lying at about 60 days. However note that all but two of the SNe that form this secondary peak are intermediate-plateau SNe.

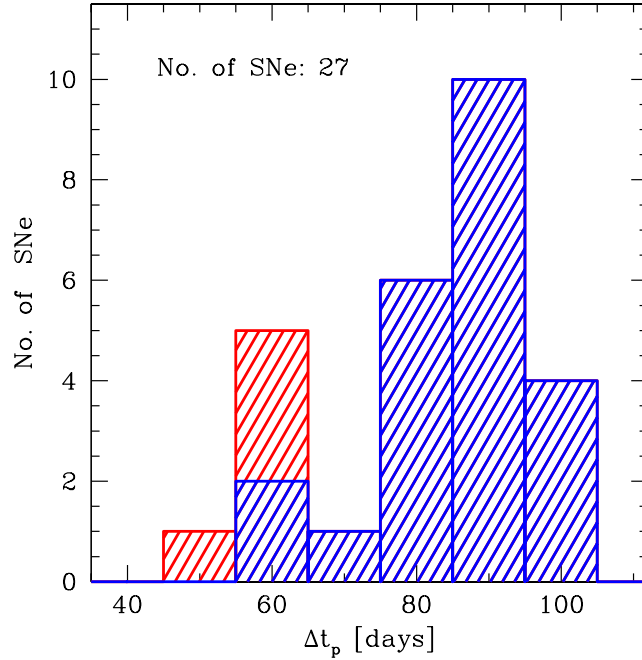


Figure 6.14: Distribution of plateau durations, Δt_p , values for SNe II-P. The SNe considered as intermediate between plateau and linear (see § 6.1) are marked in red.

Figure 6.15 shows a comparison of the light curves of five SNe selected to illustrate the variety of plateau durations. The range of plateau durations is between 47 and 103 days. However, if we restrict the sample to those SNe with bolometric LC showing a genuine plateau, the range is reduced to 64 – 103 days. The weighted average value of the plateau duration in our whole sample is $\langle \Delta t_p \rangle = 90.47 \pm 1.18$ days.

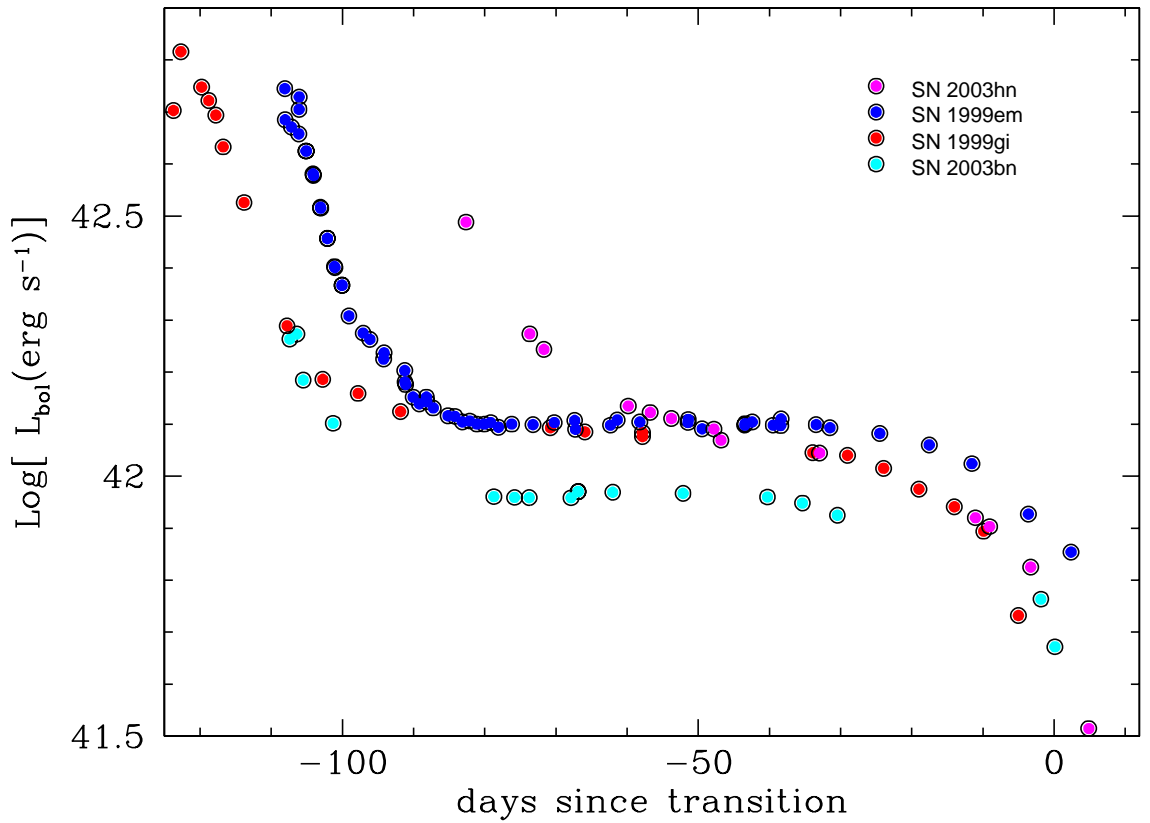


Figure 6.15: Bolometric light curves for four SNe in our sample showing the range of variation of the plateau lengths.

6.1.3 Luminosity drop: $\Delta \log L$

The purpose of this parameter is to quantify the luminosity drop between the plateau and the radioactive phase which is sensitive to the nickel mass and its level of mixing. The calculation of $\Delta \log L$ involves the use of the plateau luminosity L_P (see 6.1.1), and an estimation of the tail luminosity (L_t) at some specific moment during the radioactive tail phase. The luminosity drop is simply $\Delta \log L = \log L_P - \log L_t$.

We choose day 20 with respect to t_{PT} (Olivares et al., 2009) as a convenient moment for the calculation because at that time all SNe have fully in the radioactive tail phase. It is therefore necessary to have at least one data point during the tail phase. In cases where more than two data points are available, a straight-line fit to the data is used to provide the value of L_t and its uncertainty. If only two data points are available, an interpolation is used. We were able to perform such fits and interpolations for 20 SNe, which additionally allowed us to determine a characteristic slope during the tail phase, $\langle \text{slope} \rangle = -0.004 \text{ dex day}^{-1}$ which is in agreement with the slope expected for radioactive decay of ^{56}Co . This slope is used to derive L_t for those SNe which only have one data point during the radioactive tail.

The values and uncertainties of L_t are given in column 5 of Table 6.1. Figure 6.16 shows the distribution of $\Delta \log L$ with a sharp peak at $\Delta \log L = 0.75$ and a concentration of SNe (18 out of 26) in the range between 0.7 and 1. Note that the intermediate-plateau SNe have $\Delta \log L$ values consistent with the genuine SNe II-P, with the exception of SN 2003cn that shows the largest value of $\Delta \log L$ as a consequence of its low estimated ^{56}Ni mass (see next section). Also note that there is only one object, namely SN 2002fa, with $\Delta \log L < 0.4$.

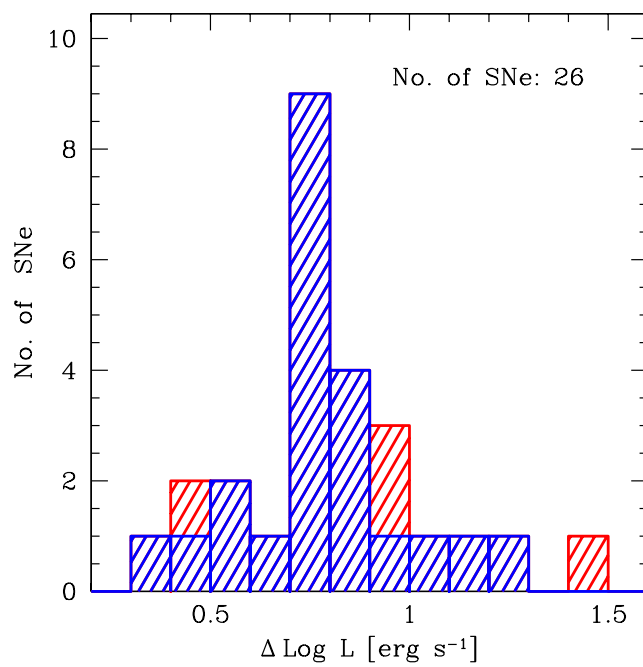


Figure 6.16: Distribution of $\Delta \log L$ for SNe II-P. The SNe considered as intermediate between plateau and linear (see § 6.1) are marked in red.

In Figure 6.17 we compare the shape of the transition between the plateau phase and the radioactive tail for SNe having a well-sampled transition. The behavior of the transition is related to the ^{56}Ni mass synthesized in the explosion and its degree of mixing. More ^{56}Ni mixing produces a more gradual transition between the plateau and the tail (Eastman et al., 1994; Utrobin, 2007). The drop for SN 2003gd appears to be steeper and larger than for the other SNe, which is indicative of less mixing and a smaller ^{56}Ni mass. For the whole sample the luminosity drop is in the range of 0.35–1.46. The weighted average value of the luminosity drop for the current sample is $\langle \Delta \log L \rangle = 0.783 \pm 0.054$.

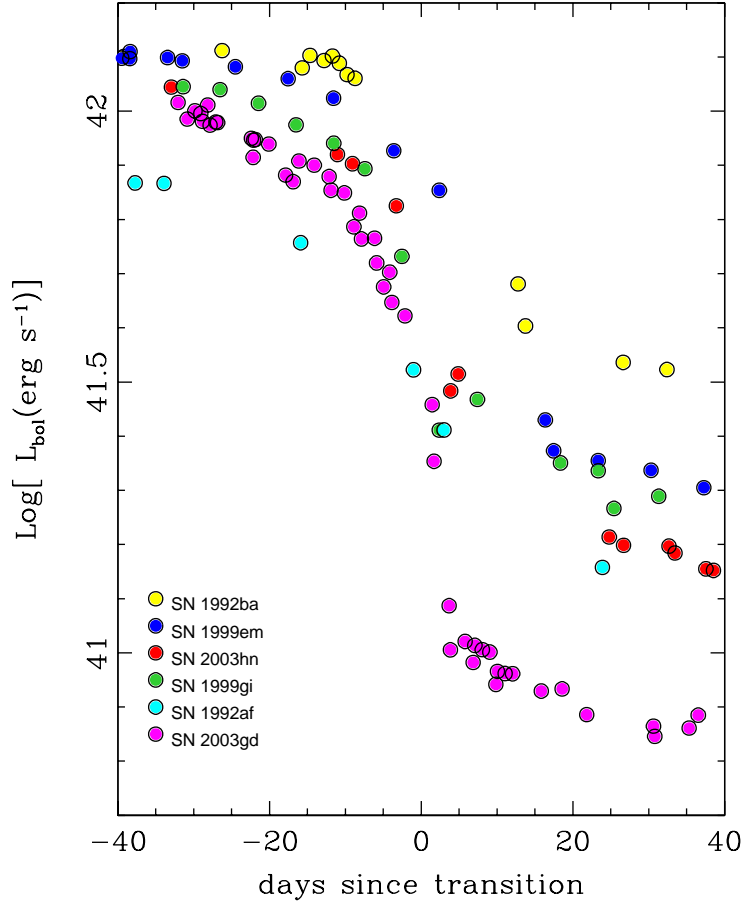


Figure 6.17: Bolometric light curves of six SNe of the sample with different transition properties.

6.1.4 ^{56}Ni mass: M_{Ni}

The bolometric luminosity during the radioactive tail phase is a direct indicator of the mass of ^{56}Ni synthesized during the explosion if we assume that all of the γ -rays resulting from $^{56}\text{Co} \rightarrow ^{56}\text{Fe}$ are fully thermalized¹. This is a reasonable assumption given that most of the SNe II-P have a late-time decline rate consistent with $^{56}\text{Co} \rightarrow ^{56}\text{Fe}$ decays (see § 6.1.3), at least in the initial phase of the nebular era. However, if some γ -rays escape before being thermalized, the estimate of M_{Ni} must be considered as a lower limit. To calculate M_{Ni} , we assume that gamma-ray deposition (see § 3.1.3) is equal to 1 in the whole structure of the object and thus $L_{\text{bol}}(t) = M_{\text{Ni}} \epsilon_{\text{rad}}(t)$ during the tail, with $\epsilon_{\text{rad}}(t)$ given by equation (3.12) of § 3.1.3. Therefore, M_{Ni} in units of M_{\odot} is given by

$$M_{\text{Ni}}[M_{\odot}] = \frac{L_{\text{bol}}(t)}{6.41 \times 10^{43} \exp\left(\frac{-(t-t_0)}{\tau_{\text{Ni}}(1+z)}\right) + 1.33 \times 10^{43} \exp\left(\frac{-(t-t_0)}{\tau_{\text{Co}}(1+z)}\right)}, \quad (6.1)$$

where $\tau_{\text{Ni}} = 8.8$ days, and $\tau_{\text{Co}} = 113.6$ days are the mean lifetimes of the radioactive isotopes. Note that t_0 is the explosion time. Based on equation (6.1) we can calculate M_{Ni} for the SNe with known t_0 and tail luminosity. Specifically, we calculate a value of M_{Ni} and its uncertainty for each data point during the tail. The resulting M_{Ni} is the weighted average of these values. Given that for some SNe we have two estimates of t_0 ($t_0(E96)$ and $t_0(D05)$ see § 2.3), two different values of M_{Ni} can be calculated. However, in column 6 of Table 6.1 we present only one value of M_{Ni} . This is in general the value corresponding to $t_0(E96)$. In cases that this value is not known, we adopted $t_0(D05)$. And if neither value is known we used estimates of t_0 found in the literature (see § 2.3). We remark that the values of M_{Ni} calculated using $t_0(D05)$ are systematically larger but consistent within the uncertainties with those based on $t_0(E96)$. That is why we present only one value of M_{Ni} .

Additionally, we include in our analysis SNe with t_+ (see § 6.1.2) well deter-

¹ ^{56}Co is daughter of ^{56}Ni , which has a half-life of only 6.1 days

mined. Using t_+ and the characteristic $\langle \Delta t_+ \rangle$ (see § 6.1.2) we can estimate the explosion time, t_0 , and therefore calculate M_{Ni} for more SNe in our sample. The uncertainty associated with this calculation is large because M_{Ni} is strongly dependent on the explosion time and the calculation of the bolometric luminosity (see § 6.1.1).

Figure 6.18 shows the distribution of M_{Ni} for all the SNe for which we can estimate this parameter. We do not include in this analysis SN 1992am for which we find a significantly higher value of the ^{56}Ni mass as compared with the rest of the sample ($\sim 0.4M_\odot$ see Table 6.1). Considering that there is a wide range of values for the explosion time of this SN in the literature, we checked if this high value of M_{Ni} could be due to an uncertainty in the value of t_0 assumed. For example, if we use the estimate of t_0 derived from t_+ and $\langle \Delta t_+ \rangle$ we find that the M_{Ni} is reduced to $0.26 \pm 0.07 M_\odot$. Although smaller, this value is still significantly large, which may imply that there are SNe II-P than can produce significant nucleosynthesis of radioactive material. Nevertheless we decided to exclude this SNe in the following analysis and leave it for a closer scrutiny in the future. The histogram shows that the SNe in our sample produce less than $0.1M_\odot$ of ^{56}Ni , with a peak at $0.035M_\odot$. There is a slight tendency to a bi-modal distribution, but this should be confirmed with a larger sample of SNe. With the exception of SN 2003cn that shows the lowest value of M_{Ni} in the whole sample, the intermediate-plateau SNe have values of $M_{\text{Ni}} < 0.1M_\odot$ consistent with the genuine SNe II-P.

In Figure 6.19 we compare the tail luminosity for a subset of five SNe. Note that the amount of ^{56}Ni synthesized by the SN determines the height of the radioactive tail. The weighted average of ^{56}Ni masses obtained in our sample of SNe II-P is $M_{\text{Ni}} = 0.024 \pm 0.004M_\odot$.

Before proceeding to the next section, we note that with the exception of SN 2003cn we did not find any peculiarity in the values of the L_P , $\Delta \log L$ and M_{Ni} for the intermediate-plateau SNe included in the analysis. This consistency strengthens the idea of a connection between linear and plateau subtypes.

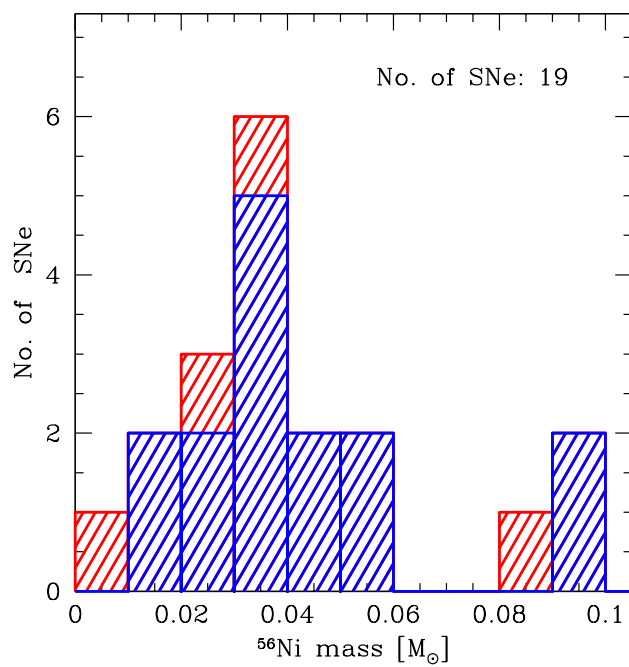


Figure 6.18: Distribution of ^{56}Ni masses for SNe II-P. The SNe considered as intermediate between plateau and linear (see § 6.1) are marked in red.

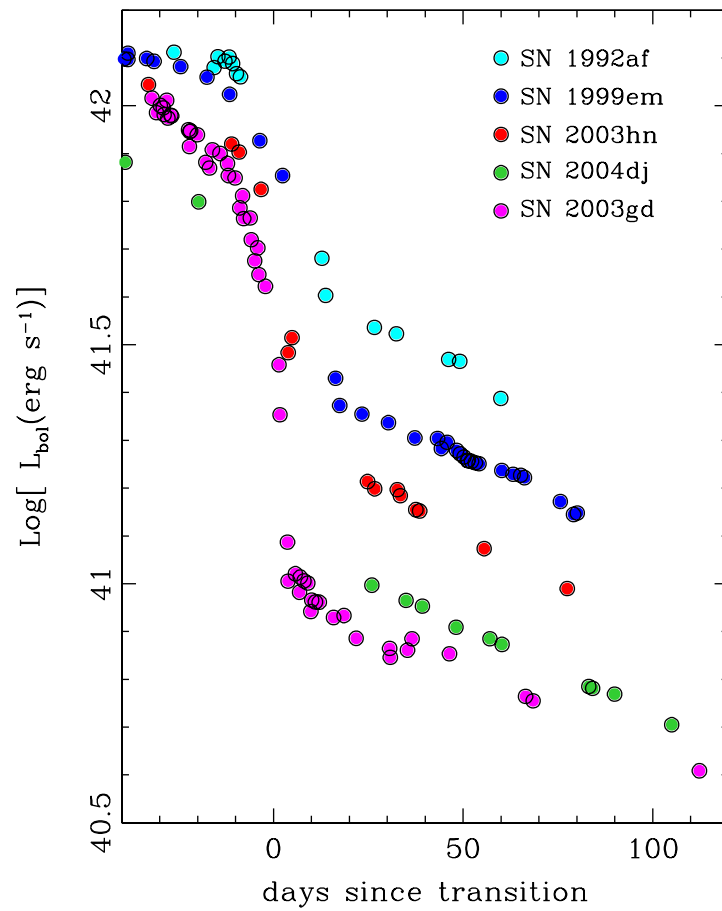


Figure 6.19: Bolometric light curves of five SNe of our sample with different tail luminosities.

6.2 Grid of Hydrodynamical Models

With the aim of comparing parameters between models and observations, and of studying correlations between observables and physical parameters, we calculated a grid of hydrodynamical models for different values of the initial mass (M_0), initial radius (R_0), explosion energy (E), ^{56}Ni mass (M_{Ni}) and mixing of nickel. Other parameters like chemical composition and density profile shape were kept fixed. The ranges of physical parameters used were: $M_0 = 10, 15, 20$ and $25 M_\odot$, $E = 0.5, 1, 2$ and 3 foe, $R_0 = 500, 1000$, and $1500 R_\odot$, $M_{\text{Ni}} = 0.02, 0.04$ and $0.07 M_\odot$, and mixing of nickel out to fraction of M_0 of $0.23, 0.5$ and 0.8 .

For each model we calculated L_P , Δt_P , and $\Delta \log L$ using the same definitions as in the previous section to perform a consistent comparison between model and observation. Additionally, we calculated the photospheric velocity at -30 days (v_{-30}) with respect to t_{PT} . In Table 6.2 we present our results for a total of 46 hydrodynamical models. Although the table includes all the models, some sets of physical parameters seem unlikely to happen in nature. For example, models with initial masses of $15, 20$ and $25 M_\odot$ and explosion energy of 0.5 foe, independently of the values of R_0 , M_{Ni} and nickel mixing, yield values of $\Delta t_P > 110$ days, which is outside the observed range for our sample of SNe. Thus, we can rule out models and refine the set of physical parameters that could produce SNe II-P.

In Figure 6.20 we show the sensitivity of our model light curves to the variation of physical parameters for some selected models of Table 6.2. A glance at this figure indicates that (a) increasing the injected energy results in higher luminosities and shorter plateau durations, (b) more massive progenitors produce longer plateaus and lower plateau luminosities, (c) more extended progenitors produce higher plateau luminosities and longer plateaus, and (d) a greater amount of ^{56}Ni produces a longer plateau and a higher tail luminosity. The behavior of our bolometric LC on variation of physical parameters is consistent with those shown in previous works (Litvinova & Nadezhin, 1983, 1985; Popov, 1993, among others). Based on the results of our models we study in greater detail the dependence of observable parameters on physical quantities (E , R_0 , M_0 and M_{Ni}). Figures 6.21, 6.22, 6.23

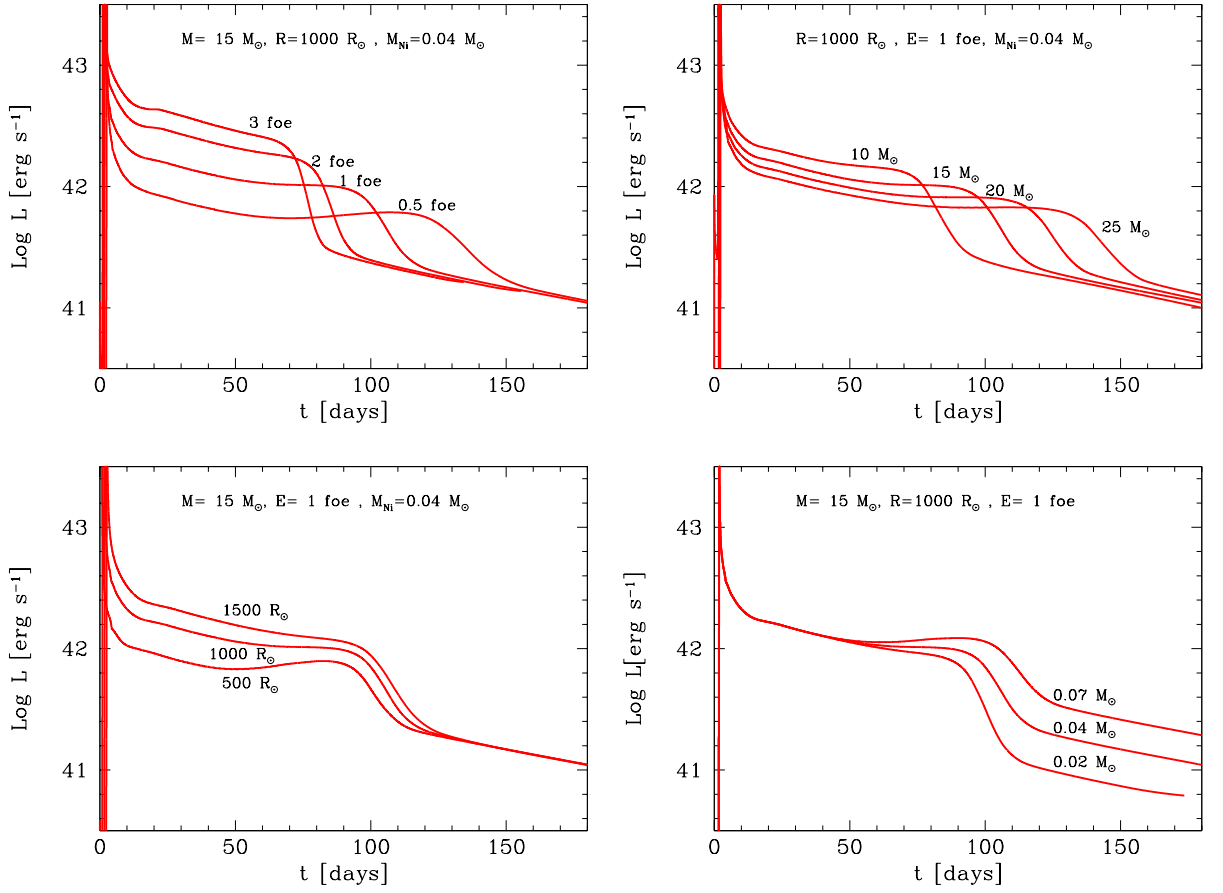


Figure 6.20: Bolometric LC for different (**upper left**) injected energies (E), (**lower left**) initial radius (R_0), (**upper right**) initial mass (M_0), and (**lower right**) ^{56}Ni mass (M_{Ni}). The shape of the LC, being sensitive to the hydrodynamics, is a useful tool to infer physical parameter of the SN progenitor.

and 6.24 show L_P , Δt_P , $\Delta \log L$ and $v(-30)$, respectively, versus explosion energy. In these figures, the size of the symbols is proportional to the progenitor mass and the shape is related to the initial radius (square symbols for $R_0 = 500R_\odot$, circles for $R_0 = 1000R_\odot$ and triangles for $R_0 = 1500R_\odot$). The colors indicate different values of ^{56}Ni mass (red color for $M_{\text{Ni}} = 0.02M_\odot$, blue for $M_{\text{Ni}} = 0.04M_\odot$ and cyan for $M_{\text{Ni}} = 0.07M_\odot$). In all these figures we only show models with a mixing of ^{56}Ni of $0.5M_0$.

From Figure 6.21 it is clear that there is a strong correlation between plateau luminosity and explosion energy. Larger explosion energies produce higher plateau

Table 6.2: Model Parameters

Model	Energy [foe]	Mass [M_{\odot}]	Radius [R_{\odot}]	M_{Ni} [M_{\odot}]	mixing ^a	$\text{Log } L_p$ [erg s ⁻¹]	Δt_p [days]	$\Delta \text{Log } L$ [erg s ⁻¹]	v^b [km s ⁻¹]
1	0.50	15	1000	0.04	0.23	41.70	119.91	0.519	1213
2	1.00	15	1000	0.04	0.23	42.02	86.16	0.711	2093
3	2.00	15	1000	0.04	0.23	42.39	62.48	0.992	3531
4	3.00	15	1000	0.04	0.23	42.61	45.71	1.167	4809
5	0.50	15	1000	0.02	0.5	41.72	97.79	0.773	1534
6	1.00	15	1000	0.02	0.5	42.07	78.80	1.016	2479
7	2.00	15	1000	0.02	0.5	42.44	53.02	1.310	4023
8	3.00	15	1000	0.02	0.5	42.63	45.07	1.466	5226
9	0.50	15	1000	0.04	0.5	41.76	116.43	0.536	1471
10	1.00	15	1000	0.04	0.5	42.07	87.83	0.717	2369
11	2.00	15	1000	0.04	0.5	42.43	64.13	0.995	3815
12	3.00	15	1000	0.04	0.5	42.63	48.07	1.155	5080
13	0.50	15	1000	0.07	0.5	41.86	135.94	0.426	1413
14	1.00	15	1000	0.07	0.5	42.08	98.59	0.507	2276
15	2.00	15	1000	0.07	0.5	42.41	74.19	0.739	3628
16	3.00	15	1000	0.07	0.5	42.62	59.03	0.912	4943
17	0.50	15	1000	0.04	0.8	41.82	112.78	0.560	1565
18	1.00	15	1000	0.04	0.8	42.11	84.85	0.738	2543
19	2.00	15	1000	0.04	0.8	42.46	60.91	1.013	4026
20	3.00	15	1000	0.04	0.8	42.64	49.89	1.168	5384
21	0.50	20	1000	0.04	0.5	41.73	151.32	0.594	1244
22	0.50	25	1000	0.04	0.5	41.70	177.66	0.693	1093
23	1.00	10	1000	0.04	0.5	42.23	43.13	0.747	3170
24	1.00	20	1000	0.04	0.5	41.98	116.04	0.703	1930
25	1.00	25	1000	0.04	0.5	41.94	138.93	0.768	1660
26	2.00	20	1000	0.04	0.5	42.29	92.64	0.922	2985
27	2.00	25	1000	0.04	0.5	42.22	110.99	0.950	2519
28	3.00	20	1000	0.04	0.5	42.47	82.43	1.084	3860
29	3.00	25	1000	0.02	0.5	42.39	99.09	1.124	3260
30	1.00	10	1000	0.02	0.5	42.24	37.21	1.100	3519
31	1.00	20	1000	0.02	0.5	41.96	108.36	0.982	1923
32	1.00	25	1000	0.02	0.5	41.90	131.66	1.143	1655
33	1.00	10	1000	0.07	0.5	42.22	65.77	0.546	2889
34	1.00	20	1000	0.07	0.5	42.03	125.44	0.526	1887
35	1.00	25	1000	0.07	0.5	41.10	147.83	0.585	1668
36	0.50	15	500	0.04	0.5	41.64	126.58	0.402	1373
37	1.00	15	500	0.04	0.5	41.87	92.70	0.498	2280
38	1.00	15	1500	0.04	0.5	42.18	83.05	0.855	2404
39	2.00	15	500	0.04	0.5	42.23	70.20	0.770	3656
40	2.00	15	1500	0.04	0.5	42.54	57.53	1.130	3877
41	3.00	15	500	0.04	0.5	42.41	59.36	0.933	4997
42	3.00	15	1500	0.04	0.5	42.73	47.90	1.279	5180
43	1.00	15	500	0.02	0.5	41.86	82.41	0.766	2381
44	1.00	15	1500	0.02	0.5	42.19	73.60	1.163	2516
45	1.00	15	500	0.07	0.5	41.92	106.16	0.338	2124
46	1.00	15	1500	0.07	0.5	42.18	93.49	0.623	2309

^a The degree of ⁵⁶Ni mixing is given as a fraction of the initial mass of the model (M_0)^b v is the photospheric velocity at -30 days with respect to the transition between the plateau and radioactive tail phases.

luminosities (see also upper-right panel of Figure 6.20). However, there is significant dispersion in this relation (~ 0.4 dex). Note that for a fixed value of explosion energy, more massive progenitors produce lower plateau luminosities and smaller initial radius also produce lower values of L_p . There is an additional contribution to the dispersion due to the ^{56}Ni mass, although it is lower than for the other parameters.

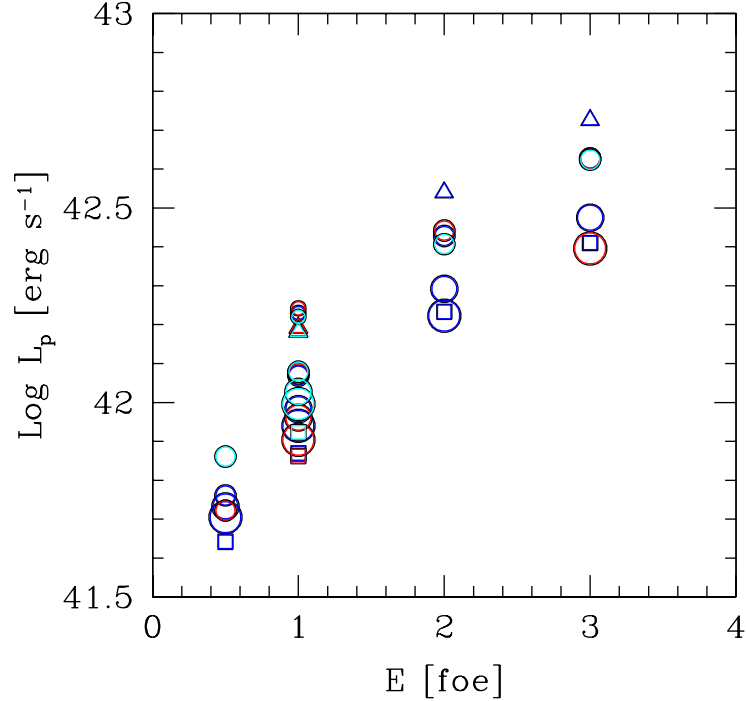


Figure 6.21: The characteristic plateau luminosity (L_p) for all of the models presented in Table 6.2 (with ^{56}Ni mixing of $0.5 M_\odot$) as a function of explosion energy. The size of the symbols is proportional to the initial mass. The shape is related to the initial radius (square symbols for $R_0 = 500R_\odot$, circles for $R_0 = 1000R_\odot$, and triangles for $R_0 = 1500R_\odot$). The colors indicate different values of ^{56}Ni mass (red color for $M_{\text{Ni}} = 0.02M_\odot$, blue for $M_{\text{Ni}} = 0.04M_\odot$, and cyan for $M_{\text{Ni}} = 0.07M_\odot$).

The plateau duration also correlates with explosion energy (see Figure 6.22) but in this case the dependence is weaker than in the case of the plateau luminosity. The progenitor mass appears to be the most important factor affecting Δt_p . Note, for example, that almost the full range of variation of Δt_p is covered for fixed $E = 1$ foe, only by changing the initial mass between $10\text{--}25 M_\odot$. Nevertheless the effect of

^{56}Ni mass is not negligible. Increasing the ^{56}Ni mass the plateau duration becomes noticeably larger. The effect of ^{56}Ni mass seems to depend on energy, being greater for smaller values of explosion energy. The initial radius produces only a minor effect on Δt_P . Another point is that we found several models with $\Delta t_P < 75$ days, interestingly these models tend to show a linear behavior consistently with the observations.

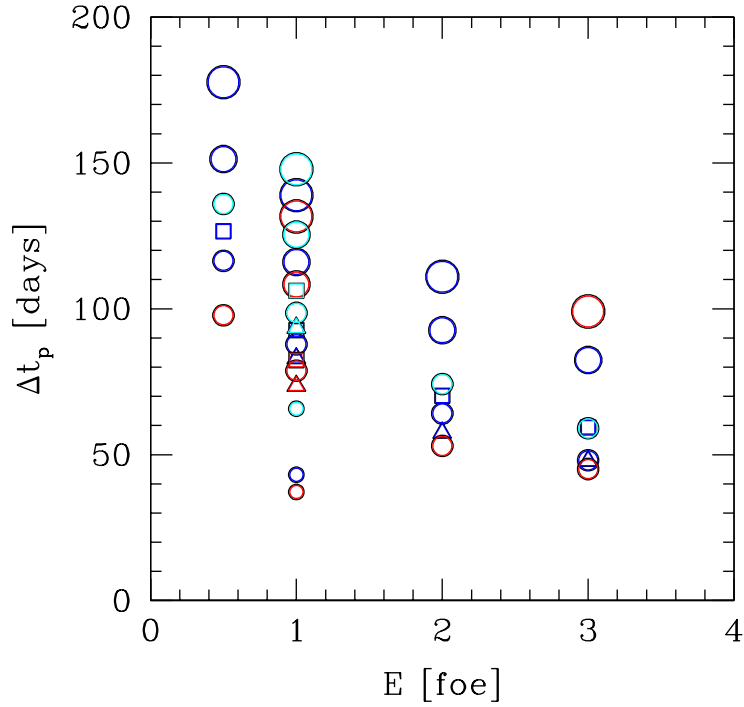


Figure 6.22: The plateau duration (Δt_P) for all of the models presented in Table 6.2 (with ^{56}Ni mixing of $0.5 M_0$) as a function of explosion energy. The size of the symbols is proportional to the initial mass. The shape is related to the initial radius (square symbols for $R_0 = 500 R_\odot$, circles for $R_0 = 1000 R_\odot$, and triangles for $R_0 = 1500 R_\odot$). The colors indicate different values of ^{56}Ni mass (red color for $M_{\text{Ni}} = 0.02 M_\odot$, blue for $M_{\text{Ni}} = 0.04 M_\odot$, and cyan for $M_{\text{Ni}} = 0.07 M_\odot$).

From Figure 6.23 we see that the post-plateau drop ΔL is slightly dependent on E . The ^{56}Ni mass appears as the main factor in the determination of this parameter, as expected from the large effect of M_{Ni} on the tail luminosity. Lower values of M_{Ni} lead to reduced brightness in the tail and therefore to higher values of ΔL , and vice

versa. Also note that ΔL is not very sensitive to the initial mass but there is some dependence on the initial radius.

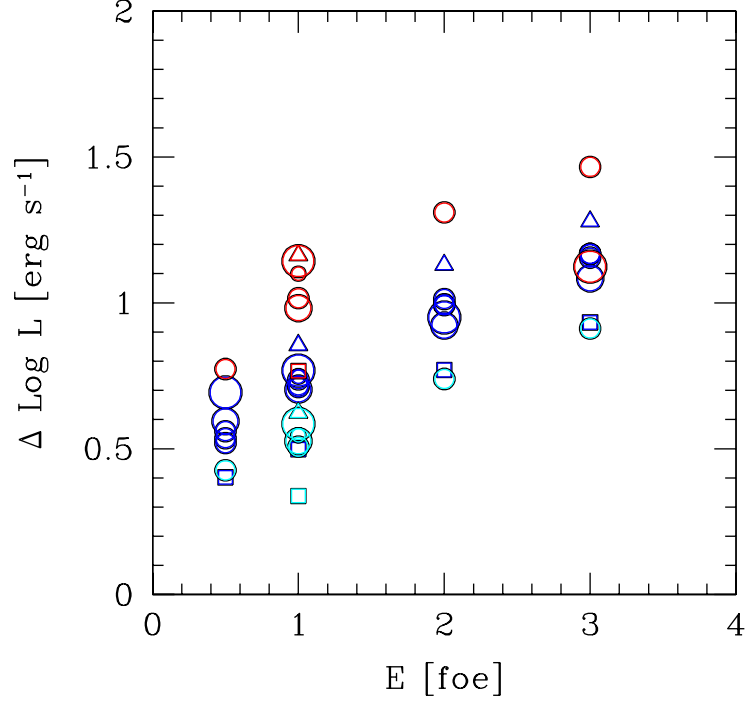


Figure 6.23: The drop in luminosity (ΔL) for all of the models presented in Table 6.2 (with ^{56}Ni mixing of $0.5 M_0$) as a function of explosion energy. The size of the symbols is proportional to the initial mass. The shape is related to the initial radius (square symbols for $R_0 = 500R_\odot$, circles for $R_0 = 1000R_\odot$, and triangles for $R_0 = 1500R_\odot$). The colors indicate different values of ^{56}Ni mass (red color for $M_{\text{Ni}} = 0.02M_\odot$, blue for $M_{\text{Ni}} = 0.04M_\odot$, and cyan for $M_{\text{Ni}} = 0.07M_\odot$).

In Figure 6.24 we plot the photospheric velocity at -30 days with respect to t_{PT} versus explosion energy. The selection of this particular epoch to evaluate the photospheric velocity was based on the work of Olivares et al. (2009) which calibrate the standard-candle method for estimating distances using expansion velocities at this epoch. We found a strong dependence of v_{-30} on the explosion energy, as expected from the fact that the explosion energy is almost completely converted into kinetic energy a few days after the explosion (see § 5.1.1). Also note that the value of v_{-30} depends on the progenitor mass in the sense that more massive progenitors

produce lower velocities for a fixed energy. There is also some dependence on ^{56}Ni at least for lower values of the progenitor mass but we do not find a dependence on initial radius.

The analysis presented above is a qualitative demonstration of the correlations among observable and physical parameters based on a limited amount of models. Further work is planned to enlarge the set of models in order to provide quantitative relations.

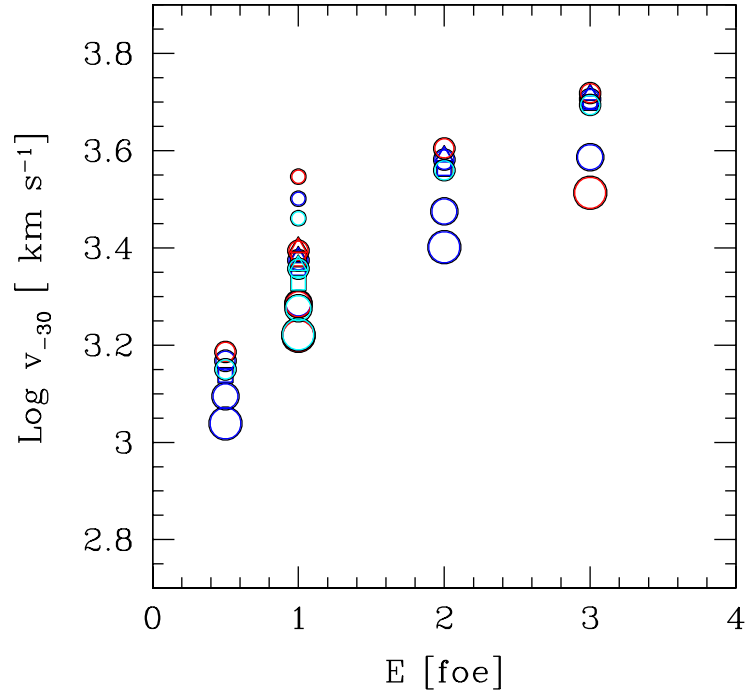


Figure 6.24: The photospheric velocity at -30 days with respect to t_{PT} ($v(-30)$) for all of the models presented in Table 6.2 (with mixing ^{56}Ni of $0.5 M_{\odot}$) as a function of the explosion energy. The size of the symbols is proportional to the initial mass. The shape is related to the initial radius (square symbols for $R_0 = 500 R_{\odot}$, circles for $R_0 = 1000 R_{\odot}$, and triangles for $R_0 = 1500 R_{\odot}$). The colors indicate different values of ^{56}Ni mass (red color for $M_{\text{Ni}} = 0.02 M_{\odot}$, blue for $M_{\text{Ni}} = 0.04 M_{\odot}$, and cyan for $M_{\text{Ni}} = 0.07 M_{\odot}$).

6.3 Observed and Modeled Correlations

In this section, we use the parameters L_P , Δt_P , $\Delta \text{Log } L$, and M_{Ni} , calculated both from the observations of our SN II-P sample (see Table 6.1) and from our grid of hydrodynamical models (see Table 6.2) to analyze correlations among them. We also include in this analysis the expansion velocity measured from the Fe II $\lambda 5169$ line at -30 days with respect to t_{PT} as calculated by Olivares et al. (2009) (see Table 4.1 of that work).

We begin by analyzing how M_{Ni} is related to other observable parameters. Figures 6.25, 6.26, 6.27 and 6.28 show L_P , Δt_P , $\Delta \text{Log } L$ and v_{-30} , respectively, as a function of the ^{56}Ni mass. In these figures, filled symbols represent the models and open symbols show the observations. Different colors are used for identifying models with different explosion energies (magenta color for $E = 0.5$ foe, blue for $E = 1$ foe, green for $E = 2$ foe, and cyan for $E = 3$ foe), and the size of the model symbols is proportional to the progenitor mass. We use \cdot . The intermediate-plateau SNe are shown with a different symbol (triangles) than genuine plateau SNe (squares).

Hamuy (2003) found a correlation between plateau luminosity and ^{56}Ni mass in the sense that more luminous supernovae produce more ^{56}Ni . The observational data in Figure 6.25 shows a slight trend in agreement with such correlation, although less pronounced than the one found by Hamuy (2003). The models show a range of plateau luminosities for any specific value of ^{56}Ni mass which is mainly caused by the explosion energy. It is important to note that the ^{56}Ni mass is introduced as a free parameter in our model while it is actually determined by the nucleosynthesis produced during the explosion and by how much ^{56}Ni falls back on the compact remnant. In any case, we see that the observations are consistent with models of explosion energy ~ 1 foe and different progenitors properties (mass and radius).

As shown in Figure 6.26, the data show no correlation between Δt_P and ^{56}Ni mass. This is consistent with the models which show only a mild dependence of the plateau duration with ^{56}Ni mass.

Figure 6.27 shows that there is a strong correlation between $\Delta \text{Log } L$ and ^{56}Ni mass, both in the models and observations. The lower the ^{56}Ni mass the greater the luminosity drop.

Finally, Figure 6.28 compares ^{56}Ni mass with v_{-30} . The observations suggest a trend where faster SNe produce larger amounts of ^{56}Ni , as was previously pointed out by Hamuy (2003). Since v_{-30} is closely related with the kinetic energy which is a considerable percentage of the explosion energy, this correlation suggests that SNe with higher explosion energy produce more nuclear burning or suffer less fall-back of the reprocessed material. From the comparison between observations and models, we see that explosion energies around 0.5 foe occur, but are not realized very often in Nature.

Given that the luminosity is an important parameter in the determination of distances, we examine the dependence of this parameter on other observables. In Figure 6.29, 6.30, and 6.31 we show its dependence on v_{-30} , Δt_P , and $\Delta \text{Log } L$, respectively. The symbol shapes and colors have the same meaning as in the previous figures.

It is known that there is a strong correlation between luminosity and the expansion velocity during the plateau phase (Hamuy & Pinto, 2002). For our sample of SNe this correlation was studied in detail by Olivares et al. (2009) using -30 days with respect to t_{PT} as the epoch where the correlation was calibrated. Figure 6.29 shows this correlation for our models and the observational data. From the figure we see that the models reproduce very well the trend of the correlation, and we can identify the explosion energy as the main driving parameter. In addition, the models show that the dispersion is related to the progenitor properties. For example, more massive progenitors produce lower expansion velocities for approximately the same luminosity. Although the trend of the correlation is well reproduced by the models we can see that there is a shift in the relationship between the models and the observations. One reason for the shift could be related to luminosity calibration used by Olivares et al. (2009) to estimate distances for the SNe in our sample. The zero point is based on two objects, SN 1999em and SN 2004dj, with known Cepheids distance. These two SNe show a difference of ~ 0.9 mag in their SCM-calibrated

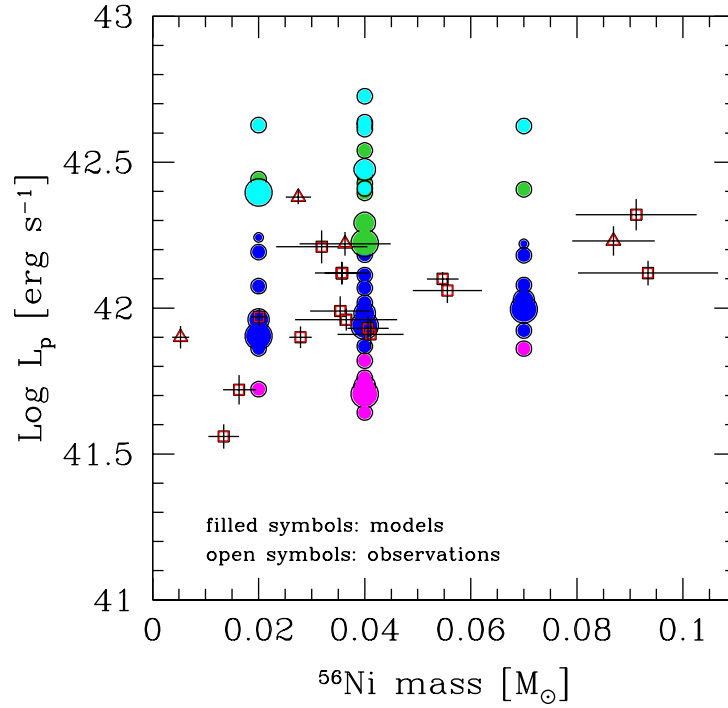


Figure 6.25: The characteristic plateau luminosity as a function of ^{56}Ni mass for models (filled symbols) and observations (open symbols). The size of the symbols is proportional to the initial mass. Colors indicate the explosion energy: magenta for $E = 0.5$ foe, blue for $E = 1$ foe, green for $E = 2$ foe and cyan for $E = 3$ foe. The intermediate-plateau SNe are shown with triangles while squares are used for genuine plateau SNe.

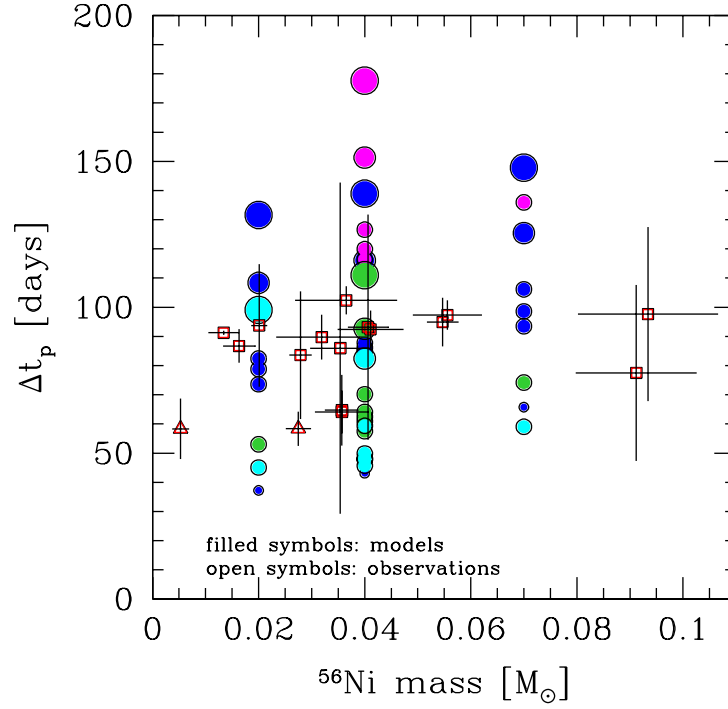


Figure 6.26: The plateau duration as a function of ^{56}Ni mass for models (filled symbols) and observations (open symbols). The size of the symbols is proportional to the initial mass. Colors indicate the explosion energy: magenta for $E = 0.5$ foe, blue for $E = 1$ foe, green for $E = 2$ foe and cyan for $E = 3$ foe. The intermediate-plateau SNe are shown with triangles while squares are used for genuine plateau SNe.

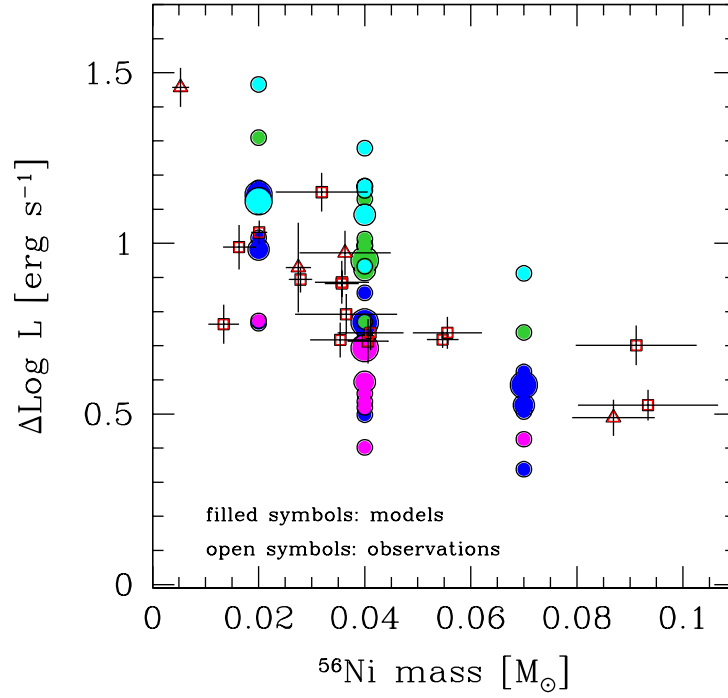


Figure 6.27: The drop in luminosity as a function of ^{56}Ni mass for models (filled symbols) and observations (open symbols). The size of the symbols is proportional to the initial mass. Colors indicate the explosion energy: magenta for $E = 0.5$ foe, blue for $E = 1$ foe, green for $E = 2$ foe and cyan for $E = 3$ foe. The intermediate-plateau SNe are shown with triangles while squares are used for genuine plateau SNe.

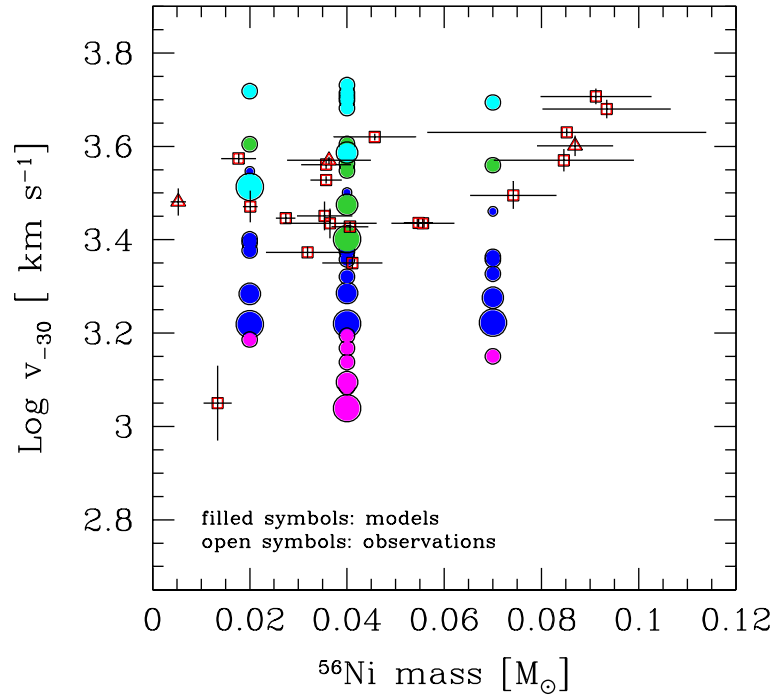


Figure 6.28: The photospheric velocity at -30 days with respect to t_{PT} as a function of ^{56}Ni mass for models (filled symbols) and observations (open symbols). The size of the symbols is proportional to the initial mass. Colors indicate the explosion energy: magenta for $E = 0.5$ foe, blue for $E = 1$ foe, green for $E = 2$ foe and cyan for $E = 3$ foe. The intermediate-plateau SNe are shown with triangles while squares are used for genuine plateau SNe.

absolute magnitude, which could lead to a shift of ~ 0.2 dex in luminosity. Other reason for the discrepancy may be that we are using photospheric velocities from the models and line velocities of Fe II $\lambda 5169$ (v_{FeII}) from the observations. The right way to do the comparison would be to convert v_{FeII} into a photospheric velocity using the calibration based on atmospheric models given by Jones et al. (2009). The problem is that this calibration is only valid for $v \gtrsim 5000 \text{ km s}^{-1}$ (see § 4.2) and therefore is out of range for most of our data. Another possibility is that our set of models does not cover the appropriate range of physical parameters. In this sense, we note that models with lower values of the initial mass are more consistent with the observations. We will explore these issues in greater detail in a future research.

From the models shown in Figure 6.30 we see that there is a relation between plateau duration and plateau luminosity. This relation is essentially a consequence of the explosion energy but we see an important dispersion associated with the progenitor properties, especially the progenitor mass. The relationship is not present in the observational data although the uncertainties in the estimation of plateau durations are large and the statistics are small. We also see that models with the lowest values of explosion energy and high masses are not consistent with the observations.

Figure 6.31 shows that the values of L_P and ΔL from models and observations are in very good agreement, especially for models with $E = 1$ and 2 foe. We also see, for the models, a dependence between these two parameters which is not observed in the data.

Finally, we compare the behavior of v_{-30} with respect to the plateau duration in Figure 6.32. We see that models predict a strong correlation between plateau durations and expansion velocities. This correlation can be understood based on the dependence of the expansion velocity on explosion energy. It is a well known fact that more energetic explosions produce shorter plateaus and vice versa. The observational data appear to follow this relation but the dispersion and the errors are large, making it difficult to draw a definitive conclusion. We note, however, that the observations rule out the lowest energy values.

Based on the comparison of different observables between models and observa-

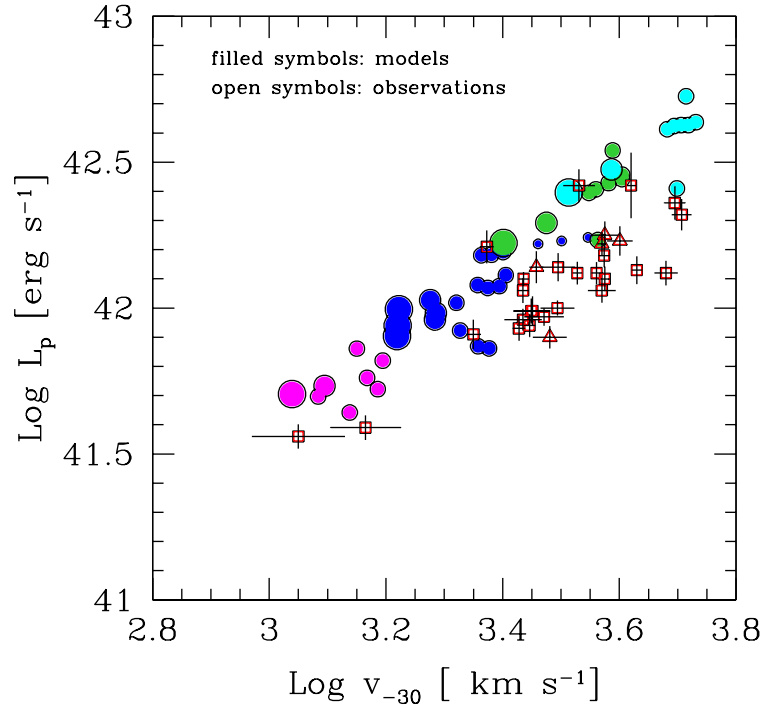


Figure 6.29: The characteristic plateau luminosity as a function of v_{-30} for models (filled symbols) and observations (open symbols). The size of the symbols is proportional to the initial mass. Colors indicate the explosion energy: magenta for $E = 0.5$ foe, blue for $E = 1$ foe, green for $E = 2$ foe and cyan for $E = 3$ foe. The intermediate-plateau SNe are shown with triangles while squares are used for genuine plateau SNe.

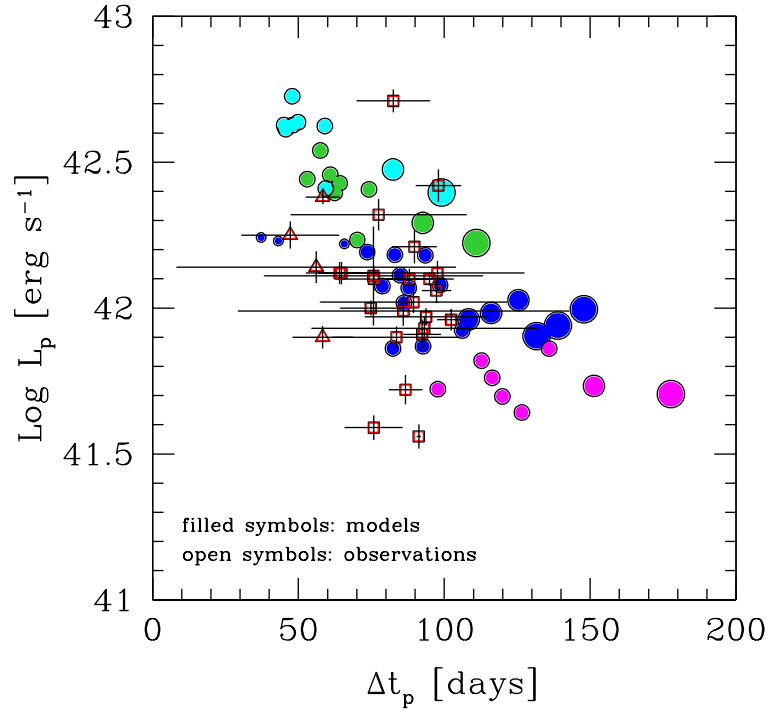


Figure 6.30: The characteristic plateau luminosity as a function of plateau duration for models (filled symbols) and observations (open symbols). The size of the symbols is proportional to the initial mass. Colors indicate the explosion energy: magenta for $E = 0.5$ foe, blue for $E = 1$ foe, green for $E = 2$ foe and cyan for $E = 3$ foe. The intermediate-plateau SNe are shown with triangles while squares are used for genuine plateau SNe.

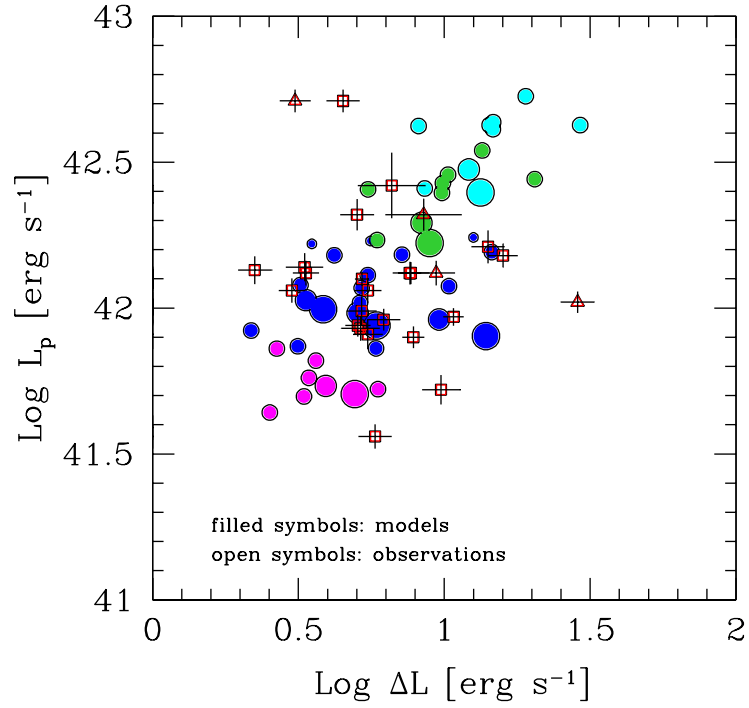


Figure 6.31: The characteristic plateau luminosity as a function of the drop in luminosity for models (filled symbols) and observations (open symbols). The size of the symbols is proportional to the initial mass. Colors indicate the explosion energy: magenta for $E = 0.5$ foe, blue for $E = 1$ foe, green for $E = 2$ foe and cyan for $E = 3$ foe. The intermediate-plateau SNe are shown with triangles while squares are used for genuine plateau SNe.

tions we conclude in general models that with $E = 0.5$ foe do not occur very often discarded. Also models with $E = 3$ foe and $M < 25M_{\odot}$ or $E = 1$ foe and $M \geq 20M_{\odot}$ are unlikely to explain the observations of our sample of SNe II-P.

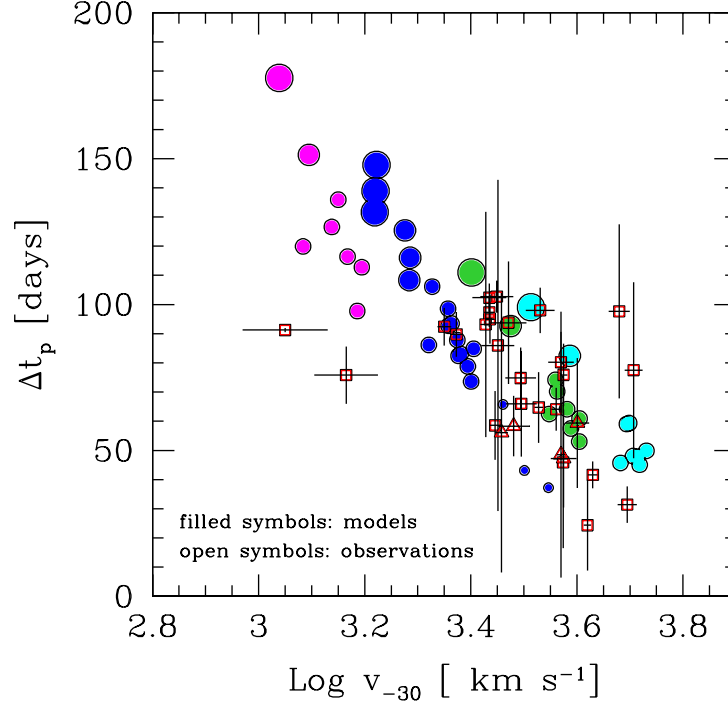


Figure 6.32: The plateau duration as a function of v_{-30} for models (filled symbols) and observations (open symbols). The size of the symbols is proportional to the initial mass. Colors indicate the explosion energy: magenta for $E = 0.5$ foe, blue for $E = 1$ foe, green for $E = 2$ foe and cyan for $E = 3$ foe. The intermediate-plateau SNe are shown with triangles while squares are used for genuine plateau SNe.

Chapter 7

Summary

The main propouse of this thesis is the development of a one-dimensional, Lagrangian hydrodynamic code to model bolometric light curves of SNe II-P with the ultimate goal of analyzing the physical properties of an available large sample of SNe with highly-precise, well-sampled observations. In the first part of the thesis I focused on the development of the hydrodynamic code, the incorporation of the required micro-physics and the construction of the progenitors models.

Since our code produces bolometric light curves and effective temperatures, it was also necessary to calculate such quantities from the observed photometry before performing a comparison between models and observations. Hence, the second (Chapter 4) of the thesis was devoted to deriving reliable calibrations for bolometric corrections (BC) and effective temperatures based on *BVI* photometry and applicable to SNe II-P. In this analysis I used data of three well-observed SNe 1987A, 1999em, and 2003hn; and two series of atmosphere models by Eastman et al. (1996) and Dessart & Hillier (2005b). I found a tight correlation betewen BC and photometric colors which allows one to estimate bolometric luminosity with an uncertainty of 0.05 dex during the plateau phase. On the radioactive tail I found that the BC was independent of color with a value of -0.70 mag and a scatter of 0.02 mag based only on the behavior of SN 1987A. I noticed the importance of including *L*- and

M -band photometry in order to derive an accurate BC during this phase.

Then, I studied in detail the performance of the code via its application to one of the best observed SNe II-P, namely SN 1999em, obtaining a very good agreement with the observations using the following physical parameters $E = 1.25$ foe, $M = 19 M_{\odot}$, $R = 800 R_{\odot}$, and $M_{\text{Ni}} = 0.056 M_{\odot}$. In this analysis, I found that an extended mixing of ^{56}Ni is needed in order to reproduce a plateau as flat as that shown by the observations of SN 1999em. I note that the plateau phase, at least in the case of this SN, is powered by the energy deposited by the shock wave and released by the recombination process, plus some extra energy deposited by the radioactive material. I compared our results with two previous hydrodynamical studies of SN 1999em given by Baklanov et al. (2005) and Utrobin (2007). Even if these studies are based on a more sophisticated prescription of the radiative transfer, there is a very good agreement among the results obtained by the three works. In particular, the physical parameters obtained in our calculations are intermediate between those estimated by Baklanov et al. (2005) and Utrobin (2007).

The remarkably good agreement of our model with the observations of SN 1999em, and the consistency found with previous hydrodynamical studies of this SN using more sophisticated code give us confidence in our attempt to model SNe II-P at least during the plateau phase and early evolution of the radioactive tail phase, in spite of the simplifications assumed in our calculation.

The last part of this thesis was focused on the study of the intrinsic properties of our sample of SNe. First, I used the calibrations of BC and effective temperature to derive bolometric luminosities and effective temperatures for our complete sample of SNe II-P. In order to make a quantitative comparison among the objects, I calculated a set of parameters that characterize the bolometric LC: (1) plateau luminosity (L_P), (2) plateau duration (Δt_P), (3) the drop in luminosity between plateau and radioactive tail ($\Delta \log L$) and (4) the nickel mass (M_{Ni}).

I found that the SN sample shows a range of 1.15 dex in plateau luminosity with a weighted average value of $\langle L_P \rangle = 1.26 \pm 0.019 \times 10^{42} \text{ erg s}^{-1}$, and plateau durations between 64 and 103 days with a weighted average value of $\langle \Delta t_p \rangle =$

90.47 ± 1.18 days. Comparing the shape of the transition between the plateau and the radioactive tail, I found that the size of the drop in luminosity to be in the range of 0.35 to 1.46 dex with a weighted average of $\langle \Delta \log L \rangle = 0.783 \pm 0.054$ dex. The radioactive nickel masses calculated for all of the SNe in our sample are below $0.1 M_{\odot}$ with a weighted average of $0.024 \pm 0.004 M_{\odot}$. However, it is important to note that I have excluded the extreme case of SN 1992am from the analysis. For this SN I found $M_{\text{Ni}} > 0.26 \pm 0.07 M_{\odot}$ implying that there are SNe II-P which produce significant nucleosynthesis during the explosion. We leave a detailed analysis of this SN for a future work. SNe with a more linearly declining behavior during the “plateau” phase show consistent values of L_P , $\Delta \log L$, and M_{Ni} , which strengthens the idea of a connection between linear and plateau SNe II. In addition, our models show a strong dependence of the Δt_P on the progenitor mass in the sense that progenitors with lower masses produce shorter Δt_P . This could mean that linear SNe in general have less massive progenitors, as has been previously proposed (see Turatto (2003)).

Then I proceeded to calculate a grid of 46 hydrodynamical models for a range of initial masses (M_0), radii (R_0), explosion energies (E), nickel masses (M_{Ni}), and nickel mixing. For each model I calculated L_P , Δt_P , $\Delta \log L$ and the photospheric velocity (v_{ph}), and I studied the dependence of these observable parameters on physical quantities (E , R_0 , M_0 and M_{Ni}).

From this analysis I found that the explosion energy is the main factor in the determination of L_P and v_{ph} , with a smaller dependence on M_0 , and on R_0 for the case of L_P . I found that M_{Ni} has no noticeable effect on the those parameters. In the case of Δt_P , I identify the progenitor mass as the most important parameter but E and M_{Ni} also produce an important effect. Finally, I found that $\Delta \log L$ largely depends on M_{Ni} , with some dependence on E and R_0 but not on M_0 .

I studied correlations among the observable parameters, L_P , Δt_P , $\Delta \log L$, M_{Ni} , and v_{ph} calculated both from the observations and hydrodynamical models. The most important results of this analysis are: (1) our models reproduce the strong correlations shown by the observations between luminosity and expansion velocity during the plateau. The slope of the relation is consistent with the observations, but there is a general shift between observational and model data. The shift is

possibly related with the zero point of the distance calibration used to calculate distances for the SNe in our sample (see Olivares et al., 2009), which could lead to a shift of ~ 0.2 dex in luminosity. I identified the explosion energy as the main driving parameter of this correlation. (2) I did not find a clear correlation between M_{Ni} and other observables with the exception of $\Delta \log L$ where I found that lower values of M_{Ni} correspond to higher $\Delta \log L$ and vice versa. (3) Our models show a certain relationship between L_P and Δt_P in the sense that more luminous SNe have shorter Δt_P , but this is not seen in the observations. It is interesting to note that this correlation was also found in a recent work by Kasen & Woosley (2009) using their hydrodynamical code and initial models from stellar-evolution calculations. (4) The models show a relationship between Δt_P and the expansion velocity with smaller values of Δt_P associated to SNe with greater expansion velocities. The observations show a similar trend but the scatter is large and the statistics is too poor to provide a definitive conclusion.

Finally, based on the comparison of different observables between models and observational data we conclude in general models with (a) $E = 0.5$ foe and $M \geq 10M_{\odot}$, (b) $E = 3$ foe and $M < 25M_{\odot}$, and (c) $E = 1$ foe and $M \geq 20M_{\odot}$ do not occur very often.

Appendix A

Finite Difference Approximations

A.1 Computational grid

A finite difference representation of a system of time dependent equations, such as the one presented in § 3.1.1 (equations 3.1–3.5), consists of defining a space-time grid upon which finite difference approximations are performed to evaluate the functions and their derivatives which constitute the partial differential equations under study. As an example, Figure A.1 shows a schematic space-time grid which consists of a set of fixed coordinate positions x_k defined at discrete times t^n . Throughout this discussion, the subscript k represents the spatial index and n , the temporal index. The temporal variable changes in a discrete fashion such that $t^{n+1} = t^n + \Delta t^{n+1/2}$, where $\Delta t^{n+1/2}$ is the time step between t^{n+1} and t^n . If the spatial coordinates are fixed, as is the case of Lagrangian coordinates, they do not carry a temporal index. The interval between two spatial coordinates, x_{k+1} and x_k , is denoted by $\Delta x_{k+1/2}$ and it is commonly referred to as grid cell or zone. Note that $\Delta x_{k+1/2}$ and $\Delta t^{n+1/2}$ need not be constant throughout the grid.

Dependent variables are defined on this space-time grid and the evolution equations take them from one spatial level to the next. However, there are different ways

to represent a dependent variable on the grid. For example, given the function $u(x, t)$ this can be defined at cell corners denoted by $u_k^n = u(x_k, t^n)$, at cell edges denoted by $u_{k-1}^{n+1/2} = u(x_{k-1/2}, t^{n+1/2})$ with $t^{n+1/2} = t^n + 0.5 \Delta t^{n+1/2}$, or at cell centers denoted by $u_{k+1/2}^{n+1/2} = u(x_{k+1/2}, t^{n+1/2})$ with $x_{k+1/2} = x_k + 0.5 \Delta x_{k+1/2}$ (see Figure A.1). The choice of the representation is based on the physical meaning of each variable.

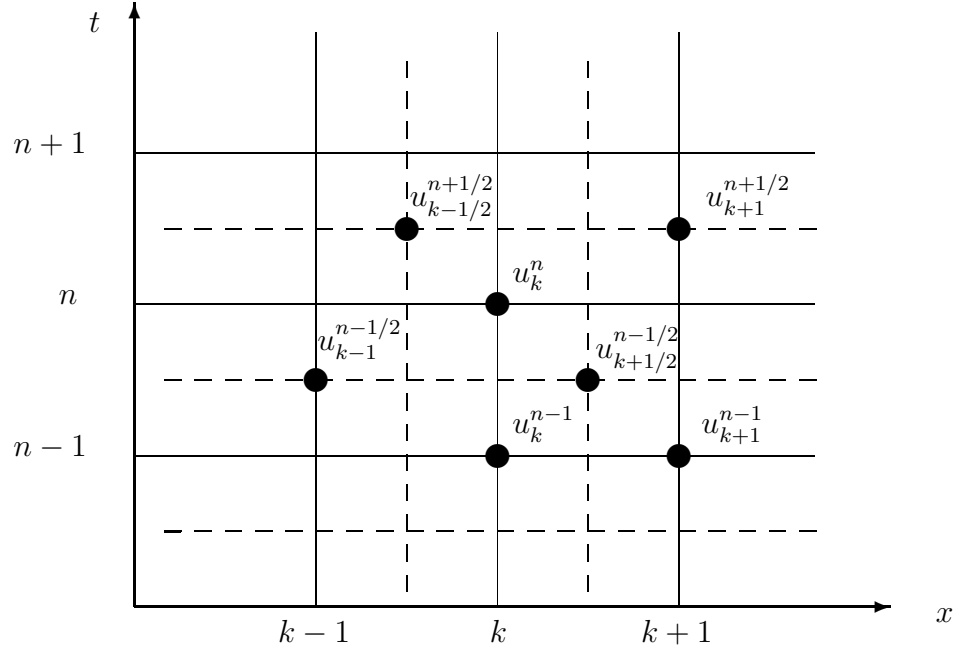


Figure A.1: Space-time grid. The values of the discretized function $u(x, t)$ can be defined either at cell corners (e.g., u_k^n), cell edges (e.g., $u_{k-1}^{n+1/2}$) or cell centers (e.g., $u_{k+1/2}^{n-1/2}$).

A.2 The Difference Equations

In the Lagrangian prescription of the hydrodynamic equations in spherical symmetric approximation (equations 3.1–3.3 of Section 3.1), the object is represented by concentric spherical shells (zones) of mass $\Delta m_{k+1/2}$ which represent the spatial coordinates of the system (analogous to $\Delta x_{k+1/2}$ in the previous discussion). The

radii r_k^n are defined at cell corners, the velocities $v_k^{n+1/2}$ are defined at the centers of vertical cell edges and the intensive quantities (ρ , P and E) are defined at the centers of the horizontal cell edges; for example the pressure is represented as $P_{k+1/2}^n$. Two time steps are also required: one to advance the velocity Δt^n defined by $\Delta t^n = 0.5(\Delta t^{n-1/2} + \Delta t^{n+1/2})$, and another to advance the material state variables, $\Delta t^{n+1/2} = t^{n+1} - t^n$.

The calculation procedure is to take known radii and velocities at t^n and determine the new values $v_k^{n+1/2}$, r_k^{n+1} and $V_{k+1/2}^{n+1}$ for all values k using the following explicit difference representation of the hydrodynamics equations

$$v_k^{n+1/2} = v_k^{n-1/2} - 4\pi(r_k^n)^2[P_{k+1/2}^n + Q_{k+1/2}^n - (P_{k-1/2}^n + Q_{k-1/2}^n)] \frac{\Delta t^n}{\Delta m_k} - \frac{Gm_k}{(r_k^n)^2} \Delta t^n \quad (\text{A.1})$$

$$r_k^{n+1} = r_k^n + v_k^{n+1/2} \Delta t^{n+1/2} \quad (\text{A.2})$$

$$V_{k+1/2}^{n+1} \equiv (\rho_{k+1/2}^{n+1})^{-1} = \frac{4\pi [(r_{k+1}^{n+1})^3 - (r_k^{n+1})^3]}{3 \Delta m_{k+1/2}} \quad (\text{A.3})$$

where Q is the *artificial viscosity* term included in the equation to take into account numerical discontinuities which are produced by the shock wave. For this term I have adopted the following expression given by Von Neumann & Richtmyer (1950)

$$Q_{k+1/2}^{n+1/2} = \begin{cases} C_q (v_{k+1/2}^{n+1/2} - v_k^{n+1/2})^2 \rho_{k+1/2}^{n+1/2} & \text{if } v_{k+1}^{n+1/2} < v_k^{n+1/2} \\ 0 & \text{otherwise} \end{cases}$$

where C_q is a constant set to a value of 2 in our calculations. The time step $\Delta t^{n+1/2}$ is chosen subject to assure stability and accuracy. The stability of the explicit numerical scheme is obtained if the time step is constrained to the Courant condition, i.e.,

$$\Delta t^{n+3/2} = \min\{\Delta m_{k+1/2}^{n+1}/v_{s,k+1/2}^{n+1}\}, \quad (\text{A.4})$$

where $v_{s,k+1/2}^{n+1}$ is the sound speed which varies from zone to zone. The time step is taken as a fraction of the Courant condition for all zones. Additional conditions on the time step are imposed to assure the accuracy of the results: it is required that changes in temperature, density and flux over one time step be less than 5%. This constraint added to that on the time step is a consequence of the iterative procedure used to solve the radiative transfer (see following discussion). Note that the iterations usually do not converge if Δt is too large. Even if we do not need to iterate, the size of Δt in the implicit scheme is limited by the error growth rate. To keep the error low, changes in the physical quantities over one time step must be less than, for example, 5%. So, the time step is limited, by reason of accuracy, to the physical time scale on which quantities change. However, in general, the physical time scale is much longer than the Courant time.

The energy and radiation transfer equations (equation 3.4 and 3.5 of Section 3.1) are solved using an iterative procedure. The discretization of the energy equation in the diffusion limit for a semi-implicit scheme is written as

$$\begin{aligned} E_{k+1/2}^{n+1} - E_{k+1/2}^n + \frac{1}{2}(P_{k+1/2}^{n+1} + P_{k+1/2}^n + Q_{k+1/2}^{n+1} + Q_{k+1/2}^n) \Delta V_{k+1/2} \\ = -[\theta(L_{k+1}^{n+1} - L_k^{n+1}) + (1 - \theta)(L_{k+1}^n - L_k^n)] \frac{\Delta t^{n+1/2}}{\Delta m_{k+1/2}} \end{aligned} \quad (\text{A.5})$$

where $\Delta V_{k+1/2} = V_{k+1/2}^{n+1} - V_{k+1/2}^n$ is written by numerical convenience as

$$\Delta V_{k+1/2} = \frac{4\pi}{3} \frac{(\Delta r_{k+1}^3 - \Delta r_k^3)}{\Delta m_{k+1/2}} \quad \text{with} \quad \Delta r_k^3 = \Delta r_k (3r_k^n r_k^{n+1} + \Delta r_k^{n+1}).$$

Here θ is a parameter with reflects the time-centering: $\theta = 1$ fully implicit scheme, and $\theta = 0.5$ for time-centering. This latter value for θ is the one I usually adopted in the calculations. The luminosity is written as

$$L_k^n = -[4\pi(r_k^n)^2]^2 \frac{ac\lambda_k^n}{3\bar{\kappa}} \frac{(T_{k+1/2}^n)^4 - (T_{k-1/2}^n)^4}{\Delta m_k}, \quad (\text{A.6})$$

where $\lambda_k^n = \frac{6+3R_k^n}{6+3R_k^n+(R_k^n)^2}$ is the “flux-limiter”, and R_k^n is written as

$$R_k^n = \frac{4\pi(r_k^n)^2}{0.5[(T_{k+1/2}^n)^4 + (T_{k-1/2}^n)^4]} \frac{|(T_{k+1/2}^n)^4 - (T_{k-1/2}^n)^4|}{\bar{\kappa} \Delta m_k}.$$

Here, $\bar{\kappa}$, which also appears in equation A.6, is the Rosseland mean opacity evaluated at m_k and t^n , i.e., $= \kappa_k^n = \kappa(T_k^n, \rho_k^n)$. Note, however, that the intensive quantities are known at the middle points of the grid. Therefore, it is needed to average the value of κ between the points $m_{k-1/2}$ and $m_{k+1/2}$. Special care must be taken to do this average in order to prevent numerical noise which appears when the radiation flow is propagated through a steep front (such as a shock-wave front) where T and P change abruptly. Following Christy (1967), instead of $\bar{\kappa}$, I have used an effective opacity defined by

$$\left(\frac{1}{\kappa}\right)_{eff} = \frac{T_{k+1/2}^4/\kappa_{k+1/2} + T_{k-1/2}^4/\kappa_{k-1/2}}{T_{k+1/2}^4 + T_{k-1/2}^4}. \quad (\text{A.7})$$

Note that knowing the values of the temperature $T_{k-1/2}^{n+1}$, $T_{k+1/2}^{n+1}$ and $T_{k+3/2}^{n+1}$ for all values k , the transport problem is solved. However, equation (A.5) is nonlinear with respect to the new temperatures at $n+1$, according to the dependence of E^{n+1} , P^{n+1} and L^{n+1} on these new values. Defining an extrapolated temperature as $T_{k+1/2}^{n+1} = T_{k+1/2}^n + \delta T_{k+1/2}$, one can linearize the energy equation in corrections $\delta T_{k+1/2}$, which leads to a system of N (equal to the number of points grid) coupled linear equations. Each equation takes the form

$$A_{k+1/2} \delta T_{k+3/2} + B_{k+1/2} \delta T_{k+1/2} + C_{k+1/2} \delta T_{k-1/2} = D_{k+1/2}, \quad (\text{A.8})$$

where $D_{k+1/2} = G(T_{k+1/2}, T_{k+1/2}, T_{k+1/2})|_{t=t^n}$, is a function of the temperature evaluated at only three spatial points and at the previous time step t^n . The other constants in equation A.8 are derivatives of this function “ G ” with respect to δT at the three different spatial points evaluated at t^n , i.e.,

$$A_{k+1/2} = \left. \frac{\partial G}{\partial(\delta T_{k+3/2})} \right|_{t=t^n}, \quad B_{k+1/2} = \left. \frac{\partial G}{\partial(\delta T_{k+1/2})} \right|_{t=t^n} \quad \text{and} \quad C_{k+1/2} = \left. \frac{\partial G}{\partial(\delta T_{k-1/2})} \right|_{t=t^n}.$$

Because each equation of the system depends on the temperature at only three adjacent mass points (see equation A.8), the system of algebraic equations takes the form of a tridiagonal matrix. This tridiagonal system is solved for all the correction temperatures δT (inverting the tridiagonal matrix). The zone temperatures are corrected and the process is repeated until the corrections are reduced to a sufficiently small amount. The condition that is usually adopted in the code for the convergence of the iterative process is that $\max(\frac{\delta T}{T}) < 10^{-5}$, where $\max(\frac{\delta T}{T})$ is the maximum value of the $\frac{\delta T}{T}$ in all the grid points.

Appendix B

Solution of Gamma-ray transfer

In this appendix I describe the solution of the γ -ray transfer in gray approximation assuming that the γ -ray opacity is purely absorptive and independent of the energy, and allowing a spherically symmetric distribution for the sources of the γ photons — i.e., the radioactive material. From this solution, the energy deposited by γ -rays can be calculated because, by definition (see Clayton, 1983), the total energy absorbed by matter per unit of time and mass is

$$\frac{dE}{dm} = \kappa_\gamma \int I d\Omega,$$

where the integral is done in all solid angles, I is the specific intensity and κ_γ is the opacity of the γ -rays for which we adopted the value $\kappa_\gamma = 0.06 y_e \text{ cm}^2 \text{ g}^{-1}$ (Sutherland & Wheeler, 1984) and y_e is the number of electrons per baryon. Although our code solves the equations in spherical symmetry, in order to correctly take into account the energy deposited in a specific point, it is necessary to consider rays which come from different directions. Nevertheless, the axial symmetry is preserved. Therefore, the previous integral in spherical coordinates and assuming axial symmetry can be written as

$$\frac{dE}{dm} = 2\pi\kappa_\gamma \int_{\theta_{min}}^{\theta_{max}} I(r, \theta) \sin\theta \, d\theta. \quad (\text{B.1})$$

As can be seen in the above expression, to calculate the energy deposited by γ -rays one should find the specific intensity in each point of the object by solving the transport of γ -rays. The radiative transfer equation in gray approximation is

$$\frac{dI}{d\tau} = -I + S, \quad (\text{B.2})$$

where I and S are the specific intensity and the source function integrated in frequency, and $d\tau = \kappa_\gamma \rho \, ds$ is the differential optical depth of γ -rays along the direction of the beam, \hat{s} . The formal solution of this equation is

$$I(\tau) = I_0 e^{-\tau} + \int_0^\tau S(\tau') e^{-(\tau-\tau')} d\tau'. \quad (\text{B.3})$$

The source function, S , is a known function in our problem and it depends on the distribution of the radioactive material. Specifically, it can be written as

$$S = \epsilon_{rad}(t) \xi(r) / \kappa_\gamma, \quad (\text{B.4})$$

where $\epsilon_{rad}(t)$ denotes the time-dependent rate of energy released per gram by Ni-Co-Fe decay,

$$\epsilon_{rad} = 3.9 \times 10^{10} \exp(-t/\tau_{\text{Ni}}) + 6.78 \times 10^9 [\exp(-t/\tau_{\text{Co}}) - \exp(-t/\tau_{\text{Ni}})] \text{ erg g}^{-1} \text{ s}^{-1},$$

and $\xi(r)$ of equation B.4 is the initial distribution of ^{56}Ni ¹. Note that this function

¹Since ^{56}Co is a decay product of ^{56}Ni , its spatial distribution is described by the same function $\xi(r)$.

Bibliography

Alexander, D. R., & Ferguson, J. W. 1994, ApJ, 437, 879

Arnett, W. D. 1980, ApJ, 237, 541

Arnett, W. D. 1988, ApJ, 331, 377

Arnett, D. 1996, *Supernovae and Nucleosynthesis: An Investigation of the History of Matter, from the Big Bang to the Present*, by D. Arnett. Princeton: Princeton University Press, 1996.

Baklanov, P. V., Blinnikov, S. I., & Pavlyuk, N. N. 2005, *Astronomy Letters*, 31, 429

Barbon, R., Ciatti, F., & Rosino, L. 1979, A&A, 72, 287

Baron, E., Hauschildt, P. H., Nugent, P., & Branch, D. 1996, MNRAS, 283, 297

Baron, E., Nugent, P. E., Branch, D., & Hauschildt, P. H. 2004, ApJL, 616, L91

Bersten, M. C., & Hamuy, M. 2009, ApJ, 701, 200

Bersten, M. C., Benvenuto, O. & Hamuy, M., 2009, submitted to ApJ

Blinnikov, S. I., & Bartunov, O. S. 1993, A&A, 273, 106

Blinnikov, S. I., Eastman, R., Bartunov, O. S., Popolitov, V. A., & Woosley, S. E. 1998, ApJ, 496, 454

Blinnikov, S., Lundqvist, P., Bartunov, O., Nomoto, K., & Iwamoto, K. 2000, ApJ, 532, 1132

- Bowers, R. L., & Wilson, J. R. 1991, Boston : Jones and Bartlett, c1991.,
- Bouchet, P., Slezak, E., Le Bertre, T., Moneti, A., & Manfroid, J. 1989, A&AS, 80, 379
- Burrows, A. 1991, Supernovae, 393
- Burrows, A., Livne, E., Dessart, L., Ott, C. D., & Murphy, J. 2006, New Astronomy Review, 50, 487
- Cardelli, J. A., Clayton, G. C., & Mathis, J. S. 1989, ApJ, 345, 245
- Chevalier, R. A. 1976, ApJ, 207, 872
- Chieffi, A., Domínguez, I., Höflich, P., Limongi, M., & Straniero, O. 2003, MNRAS, 345, 111
- Christy, R. F. 1967, Methods in computational physics, vol. 7, astrophysics, 191, 218
- Clayton, D. D. 1983, Chicago: University of Chicago Press, 1983,
- Cousins, A. W. J. 1971, Royal Observatory Annals, 7, C
- Dessart, L., & Hillier, D. J. 2005, A&A, 437, 667
- Dessart, L., & Hillier, D. J. 2005, A&A, 439, 671
- Dessart, L., & Hillier, D. J. 2008, MNRAS, 383, 57
- Dessart, L. 2008 private communication
- Eastman, R. G., Woosley, S. E., Weaver, T. A., & Pinto, P. A. 1994, ApJ, 430, 300
- Eastman, R. G., Schmidt, B. P., & Kirshner, R. 1996, ApJ, 466, 911
- Elmhamdi, A., Chugai, N. N., & Danziger, I. J. 2003, A&A, 404, 1077
- Ensmann, L., & Burrows, A. 1992, ApJ, 393, 742
- Falk, S. W., & Arnett, W. D. 1977, ApJS, 33, 515
- Filippenko, A. V. 1997, ARA&A, 35, 309

- Freedman, W. L., et al. 2001, *ApJ*, 553, 47
- Gezari, S., et al. 2008, *ApJL*, 683, L131
- Grassberg, E. K., Imshennik, V. S., & Nadyozhin, D. K. 1971, *Ap&SS*, 10, 28
- Hamuy, M., & Suntzeff, N. B. 1990, *AJ*, 99, 1146
- Hamuy, M., Phillips, M. M., Suntzeff, N. B., Schommer, R. A., Maza, J., & Aviles, R. 1996, *AJ*, 112, 2398
- Hamuy, M. 2001, Ph.D. thesis, Univ. Arizona
- Hamuy, M., & Pinto, P. A. 2002, *ApJL*, 566, L63
- Hamuy, M. 2003, *ApJ*, 582, 905
- Hamuy, M., et al. 2010, in preparation
- Heger, A., Fryer, C. L., Woosley, S. E., Langer, N., & Hartmann, D. H. 2003, *ApJ*, 591, 288
- Hendry, M. A., et al. 2005, *MNRAS*, 359, 906
- Herzig, K., El Eid, M. F., Fricke, K. J., & Langer, N. 1990, *A&A*, 233, 462
- Hillebrandt, W. 1990. Models of type II Supernovae: An Introduction. *Supernovae: Les Houches, session LIV*, 1990
- Hoflich, P. 1991, *Supernovae*, 415
- Iglesias, C. A., & Rogers, F. J. 1996, *ApJ*, 464, 943
- Imshenik, V. S., & Nadezhin, D. K. 1965, *Soviet Astronomy*, 8, 664
- Janka, H.-T., Langanke, K., Marek, A., Martínez-Pinedo, G., Muuumlmler, B. 2007, *Phys. Rep.*, 442, 38
- Johnson, H. L., Iriarte, B., Mitchell, R. I., & Wisniewskj, W. Z. 1966, *Communications of the Lunar and Planetary Laboratory*, 4, 99
- Jones, M. I., et al. 2009, *ApJ*, 696, 1176

- Kane, J., Arnett, D., Remington, B. A., Glendinning, S. G., Bazán, G., Müller, E., Fryxell, B. A., & Teyssier, R. 2000, *ApJ*, 528, 989
- Karp, A. H., Lasher, G., Chan, K. L., & Salpeter, E. E. 1977, *ApJ*, 214, 161
- Kasen, D., & Woosley, S. E. 2009, *ApJ*, 703, 2205
- Kippenhahn, R., Weigert, A., & Hofmeister, E., *Methods in computational physics*, vol. 7, astrophysics
- Krisciunas, K., et al. 2009, *AJ*, 137, 34
- Leonard, D. C., et al. 2002, *AJ*, 124, 2490
- Leonard, D. C., Kanbur, S. M., Ngeow, C. C., & Tanvir, N. R. 2003, *ApJ*, 594, 247
- Leonard, D. C., & Filippenko, A. V. 2005, 1604-2004: Supernovae as Cosmological Lighthouses, 342, 330
- Levermore, C. D., & Pomraning, G. C. 1981, *ApJ*, 248, 321
- Li, W. D. 1999, *IAU Circ.*, 7294, 1
- Limongi, M., Straniero, O., & Chieffi, A. 2000, *ApJS*, 129, 625
- Litvinova, I. I., & Nadezhin, D. K. 1983, *Ap&SS*, 89, 89
- Litvinova, I. Y., & Nadezhin, D. K. 1985, *Soviet Astronomy Letters*, 11, 145
- Matz, S. M., Share, G. H., Leising, M. D., Chupp, E. L., & Vestrand, W. T. 1988, *Nature*, 331, 416
- Mitchell, R. C., Baron, E., Branch, D., Hauschildt, P. H., Nugent, P. E., Lundqvist, P., Blinnikov, S., & Pun, C. S. J. 2002, *ApJ*, 574, 293
- Montes, M. J., & Wagoner, R. V. 1995, *ApJ*, 445, 828
- Mueller, E., Fryxell, B., & Arnett, D. 1991, *A&A*, 251, 505
- Nadyozhin, D. K. 2003, *MNRAS*, 346, 97
- Olivares, F. et al., 2009, submitted to *ApJ*

- Pastorello, A., et al. 2006, MNRAS, 370, 1752
- Patat, F., Barbon, R., Cappellaro, E., & Turatto, M. 1994, A&A, 282, 731
- Perlmutter, S., et al. 1999, ApJ, 517, 565
- Phillips, M. M. 1993, ApJL, 413, L105
- Popov, D. V. 1993, ApJ, 414, 712
- Riess, A. G., et al. 1998, AJ, 116, 1009
- Rogers, F. J., Swenson, F. J., & Iglesias, C. A. 1996, ApJ, 456, 902
- Sahu, D. K., Anupama, G. C., Srividya, S., & Muneer, S. 2006, MNRAS, 372, 1315
- Schlegel, D. J., Finkbeiner, D. P., & Davis, M. 1998, ApJ, 500, 525
- Shigeyama, T., Nomoto, K., Hashimoto, M., & Sugimoto, D. 1987, Nature, 328, 320
- Shigeyama, T., Nomoto, K., & Hashimoto, M. 1988, A&A, 196, 141
- Shigeyama, T., & Nomoto, K. 1990, ApJ, 360, 242
- Sobolev, V. V. 1980, Astrofizika, 16, 695
- Smartt, S. J., Maund, J. R., Hendry, M. A., Tout, C. A., Gilmore, G. F., Mattila, S., & Benn, C. R. 2004, Science, 303, 499
- Smartt, S. J., Eldridge, J. J., Crockett, R. M., & Maund, J. R. 2009, MNRAS, 395, 1409
- Smartt, S. J. 2009, arXiv:0908.0700
- Sorokina, E. I., & Blinnikov, S. I. 2002, Nuclear Astrophysics, 57
- Suntzeff, N. B., & Bouchet, P. 1990, AJ, 99, 650
- Sutherland, P. G., & Wheeler, J. C. 1984, ApJ, 280, 282
- Swartz, D. A., Wheeler, J. C., & Harkness, R. P. 1991, ApJ, 374, 266
- Swartz, D. A., Sutherland, P. G., & Harkness, R. P. 1995, ApJ, 446, 766

- Tominaga, N., Blinnikov, S., Baklanov, P., Morokuma, T., Nomoto, K., & Suzuki, T. 2009, *ApJL*, 705, L10
- Tsvetkov, D. Y., Volnova, A. A., Shulga, A. P., Korotkiy, S. A., Elmhamdi, A., Danziger, I. J., & Ereshko, M. V. 2006, *A&A*, 460, 769
- Turatto, M. 2003, *Supernovae and Gamma-Ray Bursters*, 598, 21
- Umeda, H., & Nomoto, K. 2005, *ApJ*, 619, 427
- Utrobin, V. 1993, *A&A*, 270, 249
- Utrobin, V. P. 2004, *Astronomy Letters*, 30, 293
- Utrobin, V. P. 2007, *A&A*, 461, 233
- Utrobin, V. P., & Chugai, N. N. 2008, *A&A*, 491, 507
- Utrobin, V. P., & Chugai, N. N. 2009, *A&A*, 506, 829
- Van Dyk, S. D., Li, W., & Filippenko, A. V. 2003, *PASP*, 115, 1289
- Vinkó, J., et al. 2006, *MNRAS*, 369, 1780
- Von Neumann, J., & Richtmyer, R. D. 1950, *Appl.Phys*, 21:232
- Woosley, S. E., Pinto, P. A., & Ensman, L. 1988, *ApJ*, 324, 466
- Woosley, S. E. 1988, *ApJ*, 330, 218
- Woosley, S. E., Hartmann, D., & Pinto, P. A. 1989, *ApJ*, 346, 395
- Woosley, S. E. & Weaver, T. A. . *Massive stars, supernovae, and nucleosynthesis. Supernovae: Les Houches, session LIV*, 1990
- Woosley, S. E., & Bloom, J. S. 2006, *ARA&A*, 44, 507
- Young, T. R., & Branch, D. 1989, *ApJL*, 342, L79
- Young, T. R. 2004, *ApJ*, 617, 1233